2016

Effect of Dopants at the Grain Boundary on Thermal Transport in β-SiC at High Temperatures

Nipun Goel
Lehigh University

Effect of Dopants at the Grain Boundary on Thermal Transport in β-SiC at High Temperatures

by

Nipun Goel

Presented to the Graduate and Research Committee
of Lehigh University
in Candidacy for the Degree of
Doctor of Philosophy
in
Mechanical Engineering

Lehigh University

May 2016

Approved and recommended for acceptance as a dissertation in partial fulfillment of the requirements for the degree of Doctor of Philosophy.

_____
Date

_____
Dissertation Director

_____
Accepted Date

Committee Members:

_____
Dr. Alparslan Oztekin, Co-Advisor

_____
Dr. Edmund B. Webb III, Co-Advisor

_____
Dr. Sudhakar Neti

_____
Dr. Jeffrey M. Rickman

_____
Dr. Dileep Singh

Acknowledgements

Graduate school was a long journey and there are lot of people that I need to acknowledge for being the source of unending encouragement and support. First and foremost, I would like to express my gratitude to my advisors, Dr. Alparslan Oztekin and Dr. Edmund B Webb III for their guidance over the last 4 years. I would also like to thank the members of my dissertation committee: Dr. Sudhakar Neti, Dr. Jeffrey M Rickman and Dr. Dileep Singh. I feel blessed that I had a committee so involved in my work and were willing to meet regularly to discuss the results and check on progress. I believe their drive played a vital role in pushing me beyond my abilities and shaping the researcher in me.

Next, I would like to thank the Industrial assessment center at Lehigh University for financially supporting my work. I would also like to thanks my colleagues Laura Solomon, Murat El and Baiou Shi for intriguing discussion about my work. I would also like to thank Kathleen Hutnik and Amy McCrae at the Graduate Life Office for helping me while I tried to manage between research and senate responsibilities. They both were key to nurturing personal and professional skills in me. Also, special thanks to JoAnn Casciano, Barbara McGuire and Jennifer Smith in the Mechanical Engineering department for all the reason that I can write another PhD dissertation on.

Finally and most importantly, I would like to thank my family back home in India. There were times when they pushed me harder than my committee. They always gave me a feeling of security and inculcated the resolution to never give up in times of hardship. Having said that, I think they are more excited to know that I'm finally done rather than the fact that I officially have a PhD.

Table of Contents

Acknowledgements iv
Table of Contents v
List of Tables viii
List of Figures ix
Abstract 1
1. Introduction 3
1.1. Motivation 3
1.2. Problem Description 4
1.3. Literature Review 6
1.4. Objectives and Thesis Structure 9
2. Molecular Dynamics Simulations 12
2.1. Introduction 12
2.2. The MD Algorithm & Newton's Equations of Motion 14
2.3. NPT, NVT, and NVE Ensembles 18
2.4. Interatomic Potentials 18
2.4.1. Tersoff's Potential 19
2.4.2. Lennard Jones 6/12 Potential 21
2.4.3. Accuracy of Interatomic Potentials 22
2.5. Equilibrium and Non-Equilibrium Methods 23
3. Grain Boundary: Structure and Dynamics 25
3.1. Introduction 25
3.2. Grain Boundary Structure 25
3.3. Grain Boundary Construction 28
3.3.1. Rotation Matrix and Crystal Orientation 29
3.3.2. Olmsted's Method and Microscopic Degrees of Freedom 32
3.3.3. Dopants at Grain Boundary 37
4. Calculating Kapitza Resistance using NEMD 40
4.1. Introduction 40
4.2. Procedure 41
4.3. Sources of Error 47

4.3.1. Periodic Boundary Conditions 47
4.3.2. Simulation Cell Finite Size Effect 49
4.3.3. Size of Heat Reservoir and Rate of Heat Addition 50
4.3.4. Non-Linearities 51
4.3.5. Temperature Transients and Time Evolution of System Temperature 53
4.3.6. Statistics and Error Bars 55
5. Thermal Conductivity of β-SiC 57
5.1. Introduction 57
5.2. Simulation Cell Size Effects and Matthiessen's Rule 58
5.3. Interatomic Potential Validation 59
5.4. Quantum Effects and Temperature Correction 64
5.5. Summary 65
6. Effect of Grain Boundary Segregation 66
6.1. Introduction 66
6.2. Kapitza Resistance for Undoped Grain Boundary 67
6.3. Effect of Dopants on Kapitza Resistance. 68
6.4. Structure Factor and Atomic Number Density 76
6.5. Summary 80
7. Effect of Temperature and Dopant Description 82
7.1. Introduction 82
7.2. Influence of Temperature 83
7.3. Influence of Dopant Mass 85
7.4. Influence of Dopant/Matrix Interaction Strength 88
7.5. Vibrational Density of States 90
7.6. Summary 99
8. Effect of Grain Boundary Orientation & Energy 101
8.1. Introduction 101
8.2. Grain Boundary Misorientation Angle 103
8.3. Effect of Misorientation Angle on Dopant Contributions 107
8.4. Influence of Grain Boundary Energy 110
8.5. Summary 115
9. Conclusions and Future Work 117
9.1. Conclusions 117

9.2. Suggestions for Future Work. 118
9.2.1. Selective Matrix Element/Dopant Affinity 119
9.2.2. Phonon Dispersion Curves Analysis 119
9.2.3. Multiple Dopant Layers 120
9.2.4. Real Dopants 120
Appendix A 122
Appendix B 130
References 137
Vita 149

List of Tables

Table 1: Parameters for the Tersoff potential, for atoms of carbon and silicon. 21

Table 2: List of dopant concentrations studied. 1 ML = 432 LJ dopant atoms 39

Table 3: Dependence of κ on system size using NEMD method 61

Table 4: Geometrical rules for Structure factor 77

Table 5: System dimensions and X and Y rotation vectors for different symmetric tilt angle GBs. Z Vector along [1 1 1]..... 104

Table 6: Radial Distribution function and coordination number for β-SiC at 500 K 123

Table 7: Hessian Matrix for 3D N atom system. The subscript for τ shows the direction for the perturbation and the force vector (X, Y or Z) on atom (1, 2, 3, …N) 132

List of Figures

Figure 1: Schematic representation of the energy usage in a typical, modern automotive system [1] (Reproduced with permission) 4

Figure 2: Schematic Representation of three-dimensional periodic simulation cell for calculation of Kapitza resistance 17

Figure 3: Example of a) tilt, b) twist and c) general grain boundary [82] Copyright © 2001 by John Wiley & Sons limited. (Reproduced with Permission) 27

Figure 4: Schematic showing atomic arrangement is [1 1 1] plane for 3C-SiC. 30

Figure 5: XY plane view of the symmetric 7.5891° tilt system (i.e., along [111]). With periodic boundary conditions at the ends, there are two GBs: one in the middle and one split at either ends. 31

Figure 6: GB energy for 7.5891° symmetric tilt system, at 500 K, with different overlapping atom deletion criteria and zero lateral scroll. 34

Figure 7: Schematic for obtaining low energy GB system by iterating over the microscopic DoF 35

Figure 8: GB energy vs. GB configuration iteration (sorted by increasing GB energy) for atomic deletion criteria of 30%, 35%, and 40% of the equilibrium bond length in 7.5891° symmetric tilt GB. 36

Figure 9: Schematic representation of three-dimensional periodic simulation cell for calculation of Kapitza resistance. 42

Figure 10: Plots for a) temperature, b) pressure, c) PE/atom and d) KE/atom in 7.5891° tilt GB system after NVT and NVE equilibration at 1000 K. Plotted on the same plot, first 20 ps show the evolution over NVT and the following 20 seconds show evolution over NVE. 43

Figure 11: Time- and space-averaged temperature distribution in the undoped 7.5891° GB system at 1000 K generated from a total of 100,000 samples taken every 100 time steps. 46

Figure 12: The temperature distribution obtained by averaging the data used in Figure 11 about the flux planes with the first GB located at X=0 Å..... 46

Figure 13: Schematic representation of Non-periodic simulation cell. 48

Figure 14: Non-linear and linear temperature regions of temperature distribution in 7.5891° symmetric tilt GB system at 500 K. Only one monocrystal has been shown in the figure here..... 52

Figure 15: Evolution of temperature in simulation system in heat source (blue) and heat sink (cyan) regions as well as planes of width 8 Å in the middle of the GB and heat reservoirs on the hot (green) and the cold (red) side. 54

Figure 16: Schematic representation of three-dimensional periodic simulation cell for calculation of Thermal Conductivity. 62

Figure 17: System size dependence of $1/\kappa$ on $1/L_x$ for β-SiC at T=500K using modified Tersoff's potential. Some error bars are of the size of the symbol and are therefore not visible..... 63

Figure 18: (a and c) Atomic arrangement at GB (at X = 0) and (b and d) density profiles across the GB. Data are shown for the weak (a and b) and strong dopant/matrix interaction limit (c and d). Data shown are for dopant concentrations 0.048, 0.167, 0.33, 0.567, and 1.007 ML (1-5). Large dark spheres are dopant atoms; Si and C atoms \whereas bright red atoms are dopants..... 71

Figure 19: Kapitza resistance versus dopant concentration for the clustered (circles), the layered (squares) limits and the undoped system (triangle); a fit to the clustered data is also shown 73

Figure 20: Temperature contours in different planes perpendicular to the direction of heat flux for a) clustered limit and b) layered limit for the contour planes (CPs) 1 through 5,

from left to right. CP1 and CP5 are half way between the GB and the flux in and out planes, respectively, while CP2 and CP4 are adjacent to the GB and CP3 is on the GB. 75

Figure 21: Bragg peak α = 1 (solid line) and α = 2 (dashed line) for the clustered (squares) and the layered (circles) limit 78

Figure 22: Normalized density in a 6Å thick layer at the GB for the clustered (squares) and the layered (circles) limit. 79

Figure 23: Effect of dopant concentration on temperature on σ_k for 7.59° symmetric tilt GB system in the cluster limit (ε_{dm} = 0.03) 85

Figure 24: Influence of mass of dopant atoms on Kapitza resistance for in the layered (red squares) and clustered (blue circles) limit and dopant concentration of 1.007ML. Error bars are the size of the symbols for the data presented in this plot. 87

Figure 25: Bragg peak α=1 (solid line) and α=2 (dashed line) for the clustered (squares) and the layered (circles) limit 88

Figure 26: Kapitza resistance for different dopant/matrix interaction strengths and a dopant concentration of 1.007ML at 1000 K. The insets show the corresponding segregation profiles for the two limiting cases with Si atoms (blue), carbon atoms (black) and dopant atoms (red). Error bars were determined by averaging over well separated 50 data points. 89

Figure 27: a) Sketch showing the location of 5 different planes for which vibrational density of states is calculated perpendicular to the direction of heat flux for b) undoped system, c) clustered limit, and d) layered limit. 93

Figure 28: Individual contribution of the constituent species Si (blue), C (red) to vibrational density of states in a) as well as the total vibrational density of states (black) for a monocrystal at equilibrium. and b) at the GB in an undoped system at steady state..... 94

Figure 29: Individual contribution of the constituent species Si (blue), C (red) and dopant (green) to vibrational density of states in as well as the total vibrational density of states (black) for a) clustered limit (ε_{dm} = 0.03) and b) layered limit (ε_{dm} = 0.3) for the dopant concentrations (left to right) 0.048 ML, 0.567 ML and 1.007 ML. 95

Figure 30: Projected vibrational density of states for an ideal crystal at 1000 K averaged over wave vectors $\vec{q}$ = [1 1 0], [1 0 1] and [0 1 1], and polarization vectors $\vec{p}$ = [1 0 0] (red), [1 1 0] (blue) and [1 1 1] (green)..... 97

Figure 31: Atomic vibrations for Silicon (red) and Carbon (blue) from eigenmode analysis at $\omega = 204$ THz..... 99

Figure 32: Free surface plots (left) and density distribution along the length (right) for 3.9632° (top), 7.5891° (middle), and 16.1021° (bottom) tilt angle about (1 1 1) plane in β-SiC mono crystal. Blue spheres are Silicon atoms and red spheres are Carbon atoms. . 103

Figure 33: Influence of temperature on Kapitza resistance at different symmetric tilt GBs 105

Figure 34: Vibrational Density of States at the GB for 3.9632° (green), 7.5891° (blue), and 16.1021° (red) symmetric tilt GB systems..... 107

Figure 35: Influence of dopant concentration on Kapitza resistance at different symmetric tilt GBs..... 108

Figure 36: Vibrational density of states at the GB in a) clustered limit and b) layered limit for 3.9632° (green), 7.5891° (blue), and 16.1021° (red) symmetric tilt GB systems at highest dopant concentration 110

Figure 37: GB energy vs. GB configuration iteration (sorted by increasing GB energy) for atomic deletion criteria of 25%, 30%, and 35% of the equilibrium bond length in 3.9632° symmetric tilt GB..... 111

Figure 38: Kapitza resistance versus dopant concentration for high energy (squares) and low energy (circles) configurations; and the clustered (solid lines), the layered (dashed lines) limits and the undoped systems (triangle)..... 112

Figure 39: GB disorder at GB1 (columns a & c) and GB2 (columns b & d) as indicated in Figure 20 a) for undoped and doped systems in the clustered limit. The first two columns are for the LE systems and the last two columns are for HE systems. 114

Figure 40: GB disorder at GB1 (columns a & c) and GB2 (columns b & d) as indicated in Figure 20 a) for doped systems in the layered limit. The first two columns are for the LE systems and the last two columns are for HE systems..... 115

Figure 41: Space discretization for the evaluation of the radial distribution function.... 122

Figure 42: Vibrational density of states for β-SiC using LD calculations. 133

Figure 43: Atomic vibrations in acoustic mode for silicon (red) and carbon (blue) from an eigenmode analysis at $\omega = 55.2$ THz. The vibrations in Silicon atoms are higher than those in their pairing carbon atoms 134

Figure 44: Atomic vibrations for acoustic mode silicon (red) and carbon (blue) from an eigenmode analysis at $\omega = 61.8$ THz. The higher vector magnitude for silicon indicates greater contribution to vibrational density of states..... 134

Figure 45: Atomic vibrations for silicon (red) and carbon (blue) from an eigenmode analysis at $\omega = 92.5$ THz. The entirely different direction of vibration for silicon and Carbon indicate an overlap in $\vec{q}$ 135

Figure 46: Atomic vibrations for optical mode for silicon (red) and carbon (blue) from an eigenmode analysis at $\omega = 188.7$ THz. The contribution from Carbon atoms to vibrational density of states is higher than that from Silicon..... 135

Figure 47: Atomic vibrations for optical mode for silicon (red) and carbon (blue) from an eigenmode analysis at $\omega = 191.6$ THz 136

Abstract

Advanced semiconductor materials for thermoelectric applications often comprise of nanostructured grains in order to take advantage of phonon scattering phenomenon at the grain boundaries and thus increase the thermoelectric figure of merit for the material. Opportunities for further improvements in the figure of merit are available via usage of appropriate dopants. In this report, thermal transport across low-angle, symmetric tilt grain boundaries in β-SiC is studied and the influence of dopants, introduced at these grain boundaries, on the phononic transmission across the grain boundary is investigated.

Non-equilibrium molecular dynamics (NEMD) simulation are used to gain insights into the impact of grain-boundary segregation on Kapitza resistance of doped β-SiC at high-temperature. In particular, the role of dopant concentration and dopant/matrix interaction strength in determining the resistance is assessed. Dopants that adhere to the matrix material with the same strength as they adhere to other dopant atoms are determined to spread out across the grain boundary cross-section forming a layered structure and resulted in a concomitant gradual increase in resistance with increase in dopant concentration. Whereas, for relatively weak dopant/matrix interaction strengths, dopant clustering predominates, and the Kapitza resistance increases significantly for small changes in dopant concentration. The different interaction strength regimes are investigated by mapping the spatial distribution of temperature at the grain boundary cross-section and calculating the degree of structural disorder. It was found that the dopant clusters lead to a heat flux parallel to the grain boundary plane and a significant increase in boundary disorder, partly explaining the observed increase in Kapitza resistance at the boundary.

A comparison of the local vibrational density of states for the weak and strong dopant/matrix interaction strength cases is performed and a subset of modes that are significant for thermal transport in this system are identified. It is determined that for the nano-structures studied, the loss of optical phonon modes that have typically been ignored for thermal transport analyses, resulted in a more significant increase in Kapitza resistance at the grain boundary. This analysis is complemented by calculations of the projected density of states and a corresponding eigenmode analysis of the dynamical matrix that highlight important phonon polarizations and propagation directions. We also examine the dependence of the Kapitza resistance on temperature, dopant mass and dopant/matrix interaction strength, the latter parameter affecting grain-boundary structure and, hence, phonon scattering.

The study concludes with an investigation into the effects of grain boundary orientation and the local grain boundary energy on phonon scattering at the boundaries. More specifically, the impact of dopants on the interface resistance is examined for these boundaries. It is observed that for the methodology used to create the grain boundary systems, the interface resistance was independent of the grain boundary orientation irrespective of the dopant concentration. However, grain boundary energy had distinct effects on the interface resistance. Layering dopant caused an increase in disorder at the grain boundaries in higher energy system resulting in an increase in phonon scattering and therefore higher interface resistance.

Chapter 1

1. Introduction

1.1. Motivation

The most germane aspect of many technologies used in our day to day activities is the management of heat in a system. While some technologies require efficient removal of heat in order to obtain best performance, others aim at retaining as much heat as possible. As the demand for oil continues to soar for a myriad of applications and the focus has been shifting to alternative sources of energy, there is an increasing interest in waste heat management and recovery. For example, a typical engine is able to convert only 25% of fuel energy to useful energy to move the vehicle and power the accessories. Furthermore, about 40% of the energy generated from the combustion of fuel is directly expelled with exhaust gases[1]. A similar observation can be made for technologies like solar towers[2], thermal power plants, industrial furnaces [3, 4], and even microchips and data centers[5-7], where heat generation is an inherent part of the process. The use of thermoelectric generators (TEGs) to recover some of the waste heat in the processes mentioned above can potentially enable the automobile industry to improve engine fuel economy by as much as 5% [8].

Historically, TEGs were primarily used in military and space applications since the late 1950s, primarily due to the ease of scalability and simplicity to use [9]. TEGs have been researched for several decades now to harvest waste heat from environments like automotive exhaust into electricity available to the automobile [10], owing in part to the

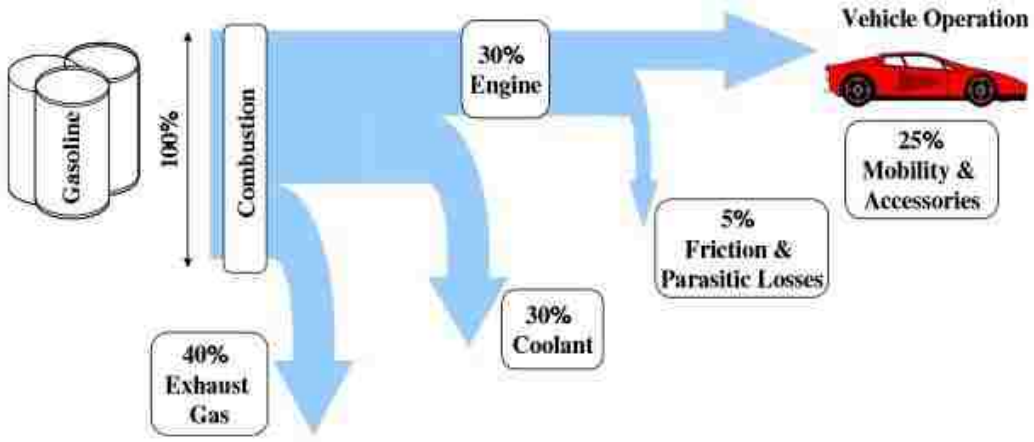

Figure 1: Schematic representation of the energy usage in a typical, modern automotive system [1] (Reproduced with permission)

absence of moving parts, importing high reliability and simplicity. The first prototype geared toward such an application dates back to the 1960s and has been pursued by automobile manufacturers like BMW, GM and Nissan. These companies have been experimenting with PbSeTe/PbTe, Bi_2Te_3/Sb_2Te_3 based alloys among several others for use as thermoelectric material in TEGs [11-13]. However, most materials available so far that offer sufficiently high thermoelectric performance can only be used in relatively low temperature scenarios; although candidate materials have been explored for high temperature thermal management applications, most contain either toxic elements like lead (Pb) or other elements that make them less attractive from a mass manufacturing perspective (i.e. because of cost/availability, toxicity, or environmental impact). Thus, great motivation exists to advance thermoelectric materials usable at high temperature and familiar to existing manufacturing practices.

1.2. Problem Description

Thermoelectric materials are characterized by a figure of merit $ZT=S^2T\sigma_e/\kappa$, which essentially quantifies the efficiency with which a material converts heat to electricity. Here

S is the Seebeck coefficient for the material, *T* is the absolute temperature, σ_e and κ are the electrical and thermal conductivity, respectively [14-16]. It is customary to include absolute temperature *T* on both sides of the figure of merit expression. *S* measures how well electronic and phononic degrees of freedom couple in a material; it can be crudely interpreted to characterize how well electrons carry heat. The sign of *S* is determined by the sign of the predominant charge carrier and the magnitude of *S* is related to the entropy per charge carrier. High *S* and σ_e mean electronic transport is both facile and associated with coupled thermal transport. Because, the most efficient thermoelectric materials will also maintain a temperature gradient across the material, lower κ is desirable. *S*, σ_e and κ are all sensitive to materials chemistry and a primary path to optimizing thermoelectric materials is through tailored chemistry, including controlled doping. However, increases in σ_e are typically accompanied by increases in κ, giving potentially minimal effect on *ZT* [17, 18]. Although thermal transport through the bulk of the material is governed by Fourier's law, on the atomistic level, it is the phononic movement through the system that is responsible for heat conduction and Fourier's law gives a more simplistic result from the overall phononic movement. A path that has therefore been proposed for reducing κ while leaving σ relatively unchanged is to increase phonon scattering at microstructure defect features, like grain boundaries (GBs), by reducing the grain size in the microstructure [19, 20]. For example, in bulk Si at 300K, 50% or more heat is carried by phonons of mean free path about 600 nm whereas only 10% heat is carried by phonons of mean free path less than about 90 nm. With the grain size reduced, it is evident that the overall thermal conductivity of the material is extensively reduced [21]. This may be an effective path for optimizing *ZT* because the mean free path for phonons is significantly larger than that for

electrons. This is particularly true for semiconducting materials, whose thermal transport is dominated by phononic modes rather than electronic. Since such materials are candidates for emerging thermoelectric applications, great potential exists to tune ZT through controlled processing of nanometer scale grain structure materials. By processing grain sizes down into the nanometer regime, potentially significant reductions in κ may be achieved without affecting σ_e or S. Further influence can be had by preferential inclusion of dopant atoms at GBs, though much remains unknown about the coupled role of scattering due to microstructure defects (GBs) and due to dopant species, both in the material matrix as well as near GBs.

1.3. Literature Review

Thermal boundary resistance, also called Kapitza resistance (R_k), is the resistance to heat flow across interfaces like those between two nano grains, and was first pointed out by P.L. Kapitza while investigating super-fluidity of Helium [22]. In other words, R_k is the measure of drop in temperature at the interface as heat current passes from one grain to another. This reflects as a reduction in the overall thermal conductivity of the system (discussed in more details in Chapter 4). R_k has since been investigated both experimentally and numerically for a wide variety of materials. R_k, has been determined to hold the key to taking advantage of nano-structuring the material for different applications. For this reason, thermoreflectance techniques have been developed which measure the change in surface reflectivity with time at the temperature of interest using high-resolution thermal microscopy to calculate R_k [23-25]. This non-destructive, non-contact method has been used extensively to examine the interfacial phonon scattering and subsequently thermal

conductivity of engineered materials. In experiments conducted by Koh and Cahill, it was demonstrated that for semiconductor alloys of InGaP, InGaAs and SiGe, the thermal conductivity of samples decreased with the decrease in the thickness of the layers as phonons with wavelength greater than the sample thickness were scattered at the interface [26]. The sample sizes that have been developed and tested range from a several hundred nm to few μm. With the reduction in size, Fourier's law ceases to apply as the thermal contribution of phonons with mean free path longer than the grain size are scattered resulting in a deviation from the bulk thermal conductivity. Thermal conductivity accumulation functions have been developed to calculate the thermal conductivity by integrating over the density of state of phonons with mean free path within the grain size limits in good agreement with the experimental observations [27-29]. In a different work, Cheaito *et al*. advanced a thermal boundary conductance accumulation function to study the phononic transmission across dissimilar material interfaces [30].

Experimental work performed thus far has been admirable in both the advancement of techniques and the usage of those techniques to probe thermal transport effects of microstructure scale defects like GBs. Experimental efforts to elucidate thermal boundary resistance and theoretical developments in this realm have benefitted greatly from companion work using atomic scale simulations. A significant body of research has been advanced to understand phonon scattering by GBs in semi-conductor materials via models with atomic scale resolution. Much of this work was based on non-equilibrium molecular dynamics simulations where either a highly characterized phonon wave packet or a heat flux is made to impinge on a boundary. In the former case, the spectral dependence of phonon transmission and reflection can be computed; in the latter case, R_k can be computed

via the discontinuous temperature drop that occurs at GBs subject to a heat flux. Topics explored in this realm include effects of mass mismatch at the GB [31-33], grain orientation [34-36], grain size [32, 37, 38], vacancy defects [39, 40], and dislocations [41-43]. Duda *et al*. observed that the cut-off radius and the strength of interaction between the atoms about a mass mismatched GB on R_k, for example, reduces with an increase in temperature [44]. High strains in materials resulting from dislocations have been identified to cause significant increase in R_k with larger Berger vector dislocations scattering more phonons [41]. The effects due to dopants at GBs have also been looked at but most of the prior work focused on low (up to 400 K) or moderate temperature (500 K – 800 K) regimes. Volz *et al*. used Non-equilibrium Green's function to demonstrate that the transmission through the interface can be controlled by introducing impurity atoms and by controlling the strength of bonds between the materials comprising the interface. They noted that the transmission is maximum when the mass of the impurity atom is the arithmetic mean of the masses on either side of the interface or when the strength of the bonds across the interface is harmonic mean of the bond strength on either sides of the interface [41]. Variation in mass, concentration, and the strength of bonds between impurity atoms have also been identified to have substantial impact on R_k [45], however, Duda *et al*. also noted that contrary to their earlier work involving chemical etching of substrate [46], R_k increased with increase in impurity concentration. In many cases where materials are either intentionally or unintentionally doped with chemical species different from the matrix elements, dopant atoms will preferentially segregate to GBs in the material. For example, dopant atoms of significantly greater size than matrix atoms have a driving force to be near GBs where crystallographic mismatch results in additional free volume. Lower stress level

due to the dopant inclusion reduces system energy [47-50]. Given this behavior in some systems, it is of interest to understand how dopants at GBs influence thermal transport across interfaces and if they can be used to maneuver thermal conductivity of the material.

1.4. Objectives and Thesis Structure

The objective of this thesis is to develop an understanding of thermal transport at nano-scale, particularly the impact of dopants on thermal conductivity across grain boundaries. The focus is primarily on β–SiC due to its high endurance and strength at high temperatures. We note that for β–SiC, the ZT is of the order of $\sim 10^{-3}$ at 500 K, and has therefore not been identified as a promising material for thermoelectric applications. We wish to determine whether its thermal properties may be substantially altered by the presence of segregating dopants. Thus, we perform large-scale molecular dynamics (MD) simulations of β–SiC bicrystals in which dopants segregate to the grain boundary to calculate thermal interface resistance using the massively parallel LAMMPS code [51]. The outline of the remainder of the thesis is as follows:

In Chapter 2, a brief history and details pertaining to the MD simulations method are discussed. Subsequently, the interatomic potential functions used to model the interactions between the constituent atoms of the matrix material as well as those with the dopant atoms are described. Finally, the equilibrium Green Kubo method and non-equilibrium direct method for predicting thermal conductivity and interfacial thermal resistance using MD simulation are introduced.

In Chapter 3, a brief introduction to grain boundaries is given. Particular emphasis is given on description of a grain boundary and the fine differences between different

possible boundaries. In this chapter, the procedure of boundary creation for our simulation cells is explained in detail. The chapter concludes with the details pertinent to introducing dopants at the grain boundary.

Chapter 4 commences with breaking down thermal conductivity in a material between contributions coming from electrons and phonons. Subsequently, the underlying physics behind thermal transport in material is used to calculate the thermal interface resistance. A detailed procedure is provided to ensure that results obtained are statistically accurate. The chapter concludes with various sources of errors in the calculations along with the appropriate measures taken to account for them.

In Chapter 5, the MD simulations procedure is validated by calculating thermal conductivity of β–SiC. The results obtained are compared to previously published work as well as experimentally obtained data. It is noted that the MD simulations performed under predict the thermal conductivity for the system and that corrections need to be performed to account for the quantum effects.

In Chapter 6, the effect of dopant segregation at the grain boundary on Kapitza resistance is explored [52]. Comparison is drawn with respect to Kapitza resistance at undoped grain boundaries as well as in systems where dopant segregation is not observed. Structure factor calculations are performed to explain the dependence of Kapitza resistance on the structural changes introduced by the dopants at the grain boundary. The chapter concludes with development of a parametric expression that accounts for the effects of different concentrations of dopants, nano-structuring, and the grain boundary disorder on Kapitza resistance.

Chapter 7 delves deeper into dopant/matrix interaction strength and discusses several cases to draw on its effect on Kapitza resistance. Phonon density of state analyses are performed to determine the key phonon modes responsible for thermal transport and the contributions from optical and acoustic phonon modes are compared. This chapter is particularly intriguing as contrary to general belief, it is found that optical modes had a much more significant contribution to thermal transport than acoustic modes. The other aspects evaluated in the chapter include effect of temperature dopant mass on Kapitza resistance.

Chapter 8 discusses the effect of grain boundary orientation on Kapitza resistance. The only grain boundary studied in chapters VI and VII is 7.5891° symmetric tilt boundary. In this chapter, four more symmetric tilt grain boundary systems are evaluated at three different temperatures. With focus maintained on the effect of dopants, three of the five symmetric tilt systems are evaluated with different dopant concentrations. Although, the undoped systems appear to be independent of grain boundary orientation, the effect of dopants becomes discretely evident at high concentrations. Phonon density of state calculations are used to explain the observations in greater detail.

In Chapter 9, the major contributions of the work presented in this thesis and suggestions for future study are discussed.

Chapter 2

2. Molecular Dynamics Simulations

2.1. Introduction

Computer simulation techniques have seen a significant advancement given that the application of computers for numerical solution is only a few decades old, with the earliest atomistic simulation performed by Metropolis *et al.* at Los Alamos National Lab using the then most powerful computer MANIAC in 1953 [53]. Computer simulations are currently used to study a wide array of phenomenon and properties like thermal and mass transport in condensed matter, fracture progression, protein folding and phase transitions. Computer simulations can be divided in to two different types: Monte Carlo (MC) simulations and molecular dynamics (MD) simulations. The idea behind MC simulations is to determine the probability of a specific outcome over several random trials. A simple example pertaining to an atomic arrangement in a system would be the potential energy of the system. MC simulations use a random number generator to randomly move atoms in the system. For each new position, the changes in potential energy of the system can be probed. Subsequently, the new atomic position is accepted if the potential energy of the system decreased. If the potential energy of the system increased, an additional probe can be done by generating a new random number between 0 and 1 and comparing it with the Boltzman factor of the energy difference between the old system state and the new system state. More details about the method can be found in Ref [53]. Although MC simulations

traditionally do not include model dynamics, newer methods that combine MC with other simulation techniques like quantum calculations are continuously being developed.

MD simulations on the other hand need a model describing atomic interactions in the material. Two of the most commonly used methods to do this are: a) ab-initio (first principle) methods and b) using classical interatomic potentials. Ab-initio method is based on quantum mechanical treatment of electrons and is therefore very advantageous in studying chemical effects. Although ab-initio methods are backed by strong physical underpinnings, they are computationally expensive and the N^3 scaling limits the system size to few hundreds of atoms. On the other hand, classical interatomic potentials not only permit access to significantly larger systems with millions of atoms, but are also much faster. Classical MD simulations also enable studying processes like melting, deformation and diffusion, which are presently inaccessible by ab-initio methods.

The properties measured in continuum scale simulation as well as from experiments are typically "averaged" properties or bulk properties that are averaged over a large number of particles and also averaged over duration of measurement. MD simulations allow us to measure the instantaneous parameters like position and velocity of atoms, which when averaged over appropriate statistics can provide the equilibrium and transport properties of a classical many-body system as measured from experiments. This scale of resolution has given the researchers the opportunity to not only verify the theory and the underlying physics, but has also enabled them to explore new ideas that can't be tested experimentally due to either technological limitations or logistics.

MD simulations are similar to a real experiment in many respects. In MD simulation, a representative model is created for the sample based on the arrangement of

particles specific to that sample, and the system is evolved using Newton's equation of motion, as discussed in Section 2.2, until the properties of the system do not change with time [54]. The only other required input is the specification of interatomic interactions. These interactions are typically obtained either through ab-initio calculation or empirical relations and are element specific. The interatomic interaction potential functions used in this work are described in Section 2.4. The first successful MD simulation was performed by Alder and Wainwright, where they solved the classical equations of motion for a system composed of hard spheres [54]. They have since come a long way.

However, MD simulations still suffer from two distinct limitations. As mentioned above, MD simulations are strictly classical. That is, for the analyses where the temperatures are below the Debye temperature for the material, quantum effects should ideally be accounted for in order to get the correct results. Several models have been proposed to account for the quantum effects [55, 56]. However, these corrections have not been made in this study. Secondly, MD simulations does not take into account the electronic effects. This means that the contribution of electrons in thermal transport is neglected. This limitation is of little impact on this study as the focus is on semiconductor materials where the thermal transport is dominated by phonons [21, 57].

2.2. The MD Algorithm & Newton's Equations of Motion

The core idea behind MD simulations is that any two particles placed in proximity of each other exert certain force on each other, the strength of which depends on the separation distance between them. Furthermore, if the separation distance between the particles increases beyond certain cutoff radius, the forces experienced by each of the

particles due to the other, becomes negligible. As such, given the masses of constituent particles, interatomic potentials that closely capture the strength of interatomic forces with the separation distance, can be used to calculate the positions and velocities of the particles at a future time $t + \delta t$ by numerically integrating the Newton's second law of motion. Several integration methods are available to numerically integrate Newton's equations in MD simulations: velocity Verlet algorithm, leap frog algorithm, reversible reference system propagator algorithms (RESPA) etc. [53, 54]. The choice of the algorithm is critical to accurately predict the trajectory of all particles as well as conserve the energy for both the short and the total duration of the simulation to prevent any energy drift. Here, velocity Verlet algorithm is used for its superior energy conservation compared to the other mentioned algorithms as well as the ability to work with large time steps, resulting in a comparatively lower number of force evaluations per unit of simulation time.

For MD simulations, a system of N particles can be identified by the positions ($r_1 \ldots r_N$) and momentum ($p_1 \ldots p_N$) and a classical description for the total energy of the system can be formed by the Hamiltonian, $\mathscr{H}$. This total energy is a sum of the kinetic energy, $K(p)$, and potential energy, $\Phi(r)$. From the velocity Verlet algorithm, positions and momentum at time $t + \delta t$ are obtained from their value at time t in the following steps [53, 54]:

$$p_i(t + \delta t/2) = p_i(t) + (\frac{1}{2})F_i(t)\delta t \quad (1)$$

$$r_i(t + \delta t) = r_i(t) + p_i(t + \frac{1}{2}\delta t)\delta t / m_i \quad (2)$$

$$p_i(t + \delta t) = p_i(t + \frac{1}{2}\delta t) + (\frac{1}{2})F_i(t + \delta t)\delta t \quad (3)$$

where m_i is the mass of the atoms i, F_i is the force experienced by the atom and is obtained from the interatomic potential as described in Section 2.4. The force evaluation is carried out after calculating the new positions at $t + \delta t$, to calculate $F_i(t+\delta t)$, to be used in equation (3).

The time taken to evaluate the forces or potential energy is proportional to N^2 due to the double loop used in the evaluation. Therefore, for a bulk material that is composed of Avogadro's number of atoms per mole, the current state of the art computational resources would be inadequate not only due the storage requirements to handle such a huge system, but also due to the computation time. A solution to this limitation is to employ periodic boundary conditions which approximate the large system by using a small simulation space. The use of periodic boundary conditions also solves the potential issue of edge and surface effects which arise from abrupt termination of the system boundaries. A 2D representation of periodic boundary condition is shown in Figure 2. These nine sections in the figure are identical as they have the same number of atoms and the same relative position of atoms within each simulation space. If an atom moves in the central section, its periodic image in all other sections also move in the same way. If an atom leaves the periodic bound of the section, its images from all other sections also move across their corresponding boundaries as shown in the figure where the dashed atom shows the new position of atom coming in from the opposite boundary. As a result, the number density in the central section is conserved.

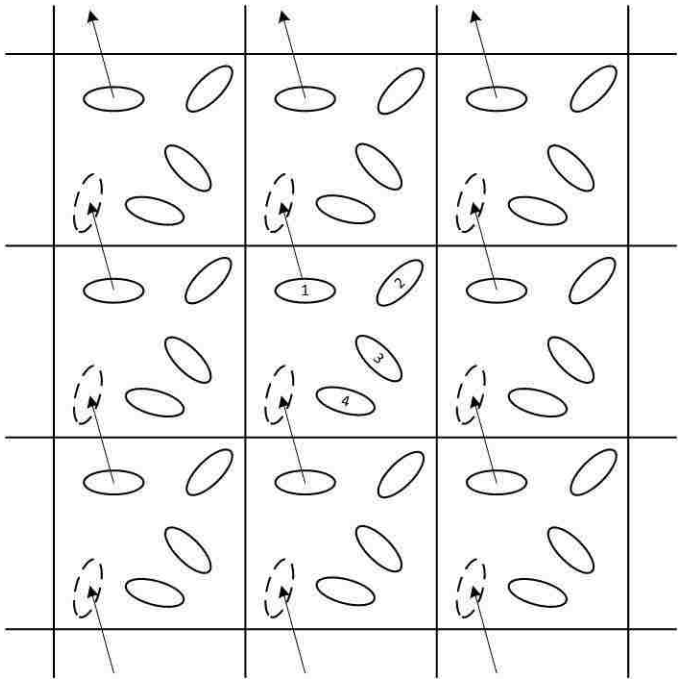

Figure 2: Schematic Representation of three-dimensional periodic simulation cell for calculation of Kapitza resistance

Although, the use of periodic boundary conditions substantially reduces the size of the system, it must be noted that the use of periodic boundary conditions inhibits the long wavelength phonons. That is, for the simulation system of size L, any phonons with wavelength greater than L are suppressed [53]. Although, this raises doubts on the accuracy of results, the common experience in simulation work has been that the equilibrium thermodynamic properties are little affected. Another important issue to keep in mind with periodic systems is that the total length of the system should be at least six times the maximum cut-off distance of the interatomic potential to prevent the atoms from experiencing forces from their own image.

2.3. NPT, NVT, and NVE Ensembles

In MD simulations, different ensembles can be used to characterize the thermodynamic states like constant volume or constant pressure, and constant energy. These properties are independent of the instantaneous position and velocity of the atoms, and are determined by statistical averaging over the simulation time. For example, for the *NVE* (micro-canonical) ensemble, the number of atoms, *N*, the system volume, *V*, and the system energy, *E*, are maintained constant whereas the temperature and the pressure are allowed to evolve with time and equilibrate to the respective average values. A simulation running with a thermostat but without a barostat will similarly be *NVT* (canonical) ensemble, or vice versa in *NPT* (isothermal-isobaric) ensemble. However, for both NPT and NVT ensembles, the total system energy is not conserved due to the application of thermostat and/or barostat.

2.4. Interatomic Potentials

In MD, interatomic potential functions are used to describe how the potential and kinetic energy of system depends on the coordinates of the constituent particles. The interatomic potentials are generally obtained by empirical methods and fitting the parameters of the potential function to experimental data. Another method to obtain the interatomic potential is by using the first principles ab-initio calculations which require the calculation of forces while taking into account the electronic structure of atoms. For this work, we used the Tersoff's potential to describe the matrix material SiC and Lennard Jones 6-12 potential to describe the interactions with dopant atoms.

2.4.1. Tersoff's Potential

Many body interatomic potential developed by Jerry Tersoff was used to describe the interatomic interactions between Silicon and Carbon atoms in SiC [58, 59]. Tersoff's potential is widely used because of its bond order nature. It is formulated so that the interaction between atoms becomes weaker as the distance between them increases, which is consistent with the physical behavior of chemical bonds between atoms. The interatomic interactions between any two atoms *i* and *j*, in the bond order potential described by Tersoff [60, 61], consists of a repulsive component and an attractive component:

$$V_{ij} = f_c(r_{ij})\left[A_{ij}e^{-\lambda_{ij}r_{ij}} - B_{ij}e^{-\mu_{ij}r_{ij}}b_{ij}\right] \tag{4}$$

here, $A_{ij}e^{-\lambda_{ij}r_{ij}}$ and $B_{ij}e^{-\mu_{ij}r_{ij}}$ represent the repulsive and the attractive pair potentials respectively, b_{ij} is the bond order parameter, and $f_c(r_{ij})$ is called the cut-off function and it cuts-off the interactions if the separation distance between the i^{th} and j^{th} atoms is more than outer distance, S, whereas it stays unity up to the inner distance, R. For all values between R and S, it varies smoothly as

$$f_c(r_{ij}) = \begin{cases} 1, & r < R \\ \frac{1}{2} - \frac{1}{2}\sin\left[\frac{\frac{\pi}{2}(r-R)}{(S-R)}\right], & R < r < S \\ 0, & r > S \end{cases} \tag{5}$$

Bond order parameter b_{ij} is a measure of the strength of the bonds between the i^{th} and the j^{th} atom. It depends on the presence of other atoms in the neighborhood of the interacting pair and has the following form:

$$b_{ij} = \frac{\chi_{ij}}{\left(1+\beta_i^{n_i}\zeta_{ij}^{n_i}\right)^{1/2n}} \tag{6}$$

where χ_{ij} determines the strength of the heteropolar bonds, relative to the value obtained by simple interaction, β and *n* are fitting parameters as provided in Table 1, and

$$\zeta_{ij} = \sum_{k\neq i,j} f_c\left(r_{ik} g\left(\theta_{ijk}\right)\right) \tag{7}$$

Here, the function $f_c(r_{ik})$ determines the cut-off distance between the central atom (i^{th}) and the neighboring atom (k^{th}). It is also evident that the bond order parameter is environment dependent, i.e., the increase in number of neighbors weakens the bond between i^{th} and j^{th} atom and can be controlled by modulating $f_c(r_{ik})$. In this work, the value of $f_c(r_{ik})$ was determined so that all Si-Si second neighbor interactions are completely excluded [55]. Due to this modification, the potential has been referred to as modified Tersoff 1994 potential in this study. The function $g\left(\theta_{i\,jk}\right)$ determines the impact of bond geometry on the strength of bonds and is given by

$$g\left(\theta_{ijk}\right) = 1 + \frac{c_i^2}{d_i^2} - \left[\frac{c_i^2}{d_i^2 + \left(h_i - \cos\theta_{ijk}\right)^2}\right] \tag{8}$$

here *c*, *d* and *h* are fitting parameters as provided in Table 1.

To find the maximum cut-off value for second neighbor interactions, radial distribution function, RDF, was calculated in LAMMPS using the Tersoff 1994 potential and a maximum cut-off of 2.65 Å was determined to be appropriate. The data from the RDF is provided in Appendix A.

Table 1: Parameters for the Tersoff potential, for atoms of carbon and silicon.

	C	Si
A (eV)	1393.6	1830.8
B (eV)	346.7	471.18
λ *(Å^{-1})*	3.4879	2.4799
μ *(Å^{-1})*	2.2119	1.7322
β	1.5724×10^{-7}	1.1×10^{-6}
n	0.72751	0.78734
c	3.8049×10^{4}	1.0039×10^{5}
d	4.384	16.217
h	-0.57058	-0.59825
R (Å)	1.8	2.7
S (Å)	2.1	3.0

2.4.2. Lennard Jones 6/12 Potential

The pairwise Lennard Jones (LJ) 6/12 interatomic potential was used to describe dopant-dopant and dopant-matrix interactions. Although LJ potential provides a realistic description of only a limited number of materials, it is often used to model systems where general effects are of greater interest rather than specific properties of the material. For example, the thermal transport properties for LJ solids have also been thoroughly characterized in numerous studies [45, 62, 63]. In this context, the LJ interaction is employed as it captures generically some of the anharmonic effects that govern phonon scattering and, thereby, thermal transport properties. In this analysis, we employed a shifted

LJ potential, $\phi(r_{ij})$, with energy and length parameters ε and σ, respectively, for atoms i and j separated by a distance r_{ij} to obtain the pair potential $E(r_{ij})$ given by

$$E\left(r_{ij}\right) = \phi\left(r_{ij}\right) - \phi\left(R_c\right) - \left(r_{ij} - R_c\right)\left.\frac{d\varphi}{dr}\right|_{r_{ij} = R_c}, \quad r < R_c \tag{9}$$

where

$$\varphi\left(r_{ij}\right) = 4\varepsilon\left[\left(\frac{\sigma}{r_{ij}}\right)^{12} - \left(\frac{\sigma}{r_{ij}}\right)^{6}\right] \tag{10}$$

and the cut-off distance $R_c = 4.5\sigma$.

In this case, either i or j (or both) must be a dopant atom. The potential parameters used in this study were σ = 2.0 Å (approximately half the lattice constant of SiC at 1000 K). Different dopant atoms were modelled by changing the ε and mass, m. The interaction strength between dopant-dopant atoms was kept constant, ε_{dd} = 0.3 eV, whereas, the interaction strength between dopant and matrix atoms (either Si or C) was varied between 0.03 eV < ε_{dm} < 0.3 eV. A time step of 0.1 femtoseconds was used in all simulations to ensure energy conservation.

2.4.3. Accuracy of Interatomic Potentials

The accuracy of the MD results is heavily influenced by the accuracy of the interatomic potential functions used. Tersoff's potential has been extensively used to describe interactions in Silicon, Carbon, and Germanium. However, the potential was not specifically created for SiC. Jerry Tersoff used various fitting parameters to match the results predicted by the potential to experimental values. Though, the parameterization advanced by Porter et al. provides good agreement with experimental results, the

"modified" Tersoff's potential used in this work still under-predicts the thermal properties in SiC. In light of these observations, the MD predictions for thermal transport in SiC are only used to qualitatively explore doping as possible solution to maneuvering thermal conductivity of the material. LJ potential is very well established for its high accuracy when used to model noble gases. The dopants modelled using LJ potential are an artificial material and are used only to explore qualitative impact of dopants on thermal transport.

2.5. Equilibrium and Non-Equilibrium Methods

The Green-Kubo method [64-72] and the direct method [66, 73-79] are the two most commonly used approaches to study thermal transport in MD simulations. The Green-Kubo method is an equilibrium technique that uses the fluctuation-dissipation theorem to calculate thermal conductivity, κ, from the heat current fluctuations. The direct method, on the contrary, is a non-equilibrium MD method that is analogous to experimental setup, wherein a thermal gradient is set up across the simulation cell and measurements on κ are made using the temperature gradient. Although, both of these methods require long simulation time to achieve a thermal equilibrium state and therefore reduce uncertainties due to thermal fluctuations, calculations using the direct method faces additional complications due to finite size effects. κ calculated from an MD system depends on the phonon mean free path, which is comparable to the system size and therefore, for small system sizes, phonon transport occurs partially in the ballistic regime. This necessitates performing multiple simulations with different system lengths to obtain results for a bulk system through extrapolation to infinite system size. The bulk value of κ can be calculated using Matthiessen's rule:

$$\frac{1}{\kappa} = \frac{1}{\kappa_{bulk}} + \frac{\alpha}{L} \tag{11}$$

where κ is the calculated thermal conductivity for the system of length L and α is a length independent coefficient. The extrapolation technique has been used by Schelling *et al.* [66] where they obtained satisfactory agreement between the calculated values of κ using Green-Kubo method and the direct method. However, similar studies conducted by Zhou et al [73] and Sellan et al [80] observed some discrepancies in the results obtained by the two methods. The Green-Kubo method has a major disadvantage as it requires a detailed expression for heat flux which in turn depends on the interatomic interactions. As such, each new system with a new class of interatomic potential necessitates rebuilding the expression for heat flux for use in Green-Kubo method [81]. Direct method on the contrary does not require the details of the interactions for studying local phenomenon, and is therefore straight forward to use.

In the work presented here, we use non-equilibrium MD method for our calculations as we will focus on grain boundary thermal (Kapitza) resistance R_k and we explore means to scatter phonons and reduce the effective κ of the system. Therefore, the finite size effects are not extremely critical. The direct method used and the procedure are discussed in detail in Section 4.

Chapter 3

3. Grain Boundary: Structure and Dynamics

3.1. Introduction

Crystalline solids are characterized by the unique and uniform atomic arrangement in the solid and in general are formed from the single nucleation point. More generally, when solids are formed for any application, they have multiple points of nucleation and as these multiple crystals grow in the process of solidification, they come in contact with each other resulting in the formation of grains. Grains are therefore crystals without the smooth edges or faces because of the impedance experienced in growth due to the adjacent (differently oriented) grains. The interface between different grains is called Grain Boundary (GB). The size of grains depends on many factors including the temperature, manufacturing technology etc., and which has a non-trivial effect on the mechanical, thermodynamic, and transport properties of the material [82].

3.2. Grain Boundary Structure

The structure of a grain boundary depends on the factors like the size and orientation of the grains that the GB interface is separating, energy of the GB, any special characteristics like the faults, defects, and dislocations, and the relative grain orientation. GBs, in general, can be fully described by five independent macroscopic degrees of freedom (DoF) and three microscopic DoF. Of the five macroscopic DoF, three determine the mutual orientation of the adjoining grains, that is, the rotation axis (2 DoF) and the

angle of rotation (1 DoF). The other two DoF are normal to the GB plane from the grains on either side of the plane [83, 84]. The three microscopic DoF are associated with the translation of the grains (2 DoF ∥ GB normal and 1 DoF ⊥ GB normal). The microscopic DoF are independent of the macroscopic DoF, resulting in a geometrical increase in the number of possible configurations for the same GB. However, the choice of the translation configuration is determined by the resulting energy of the GB. The translation configuration and the three microscopic DoF will be discussed in greater detail in Section 3.3.2.

Miller indices of the grain described by the DoF mentioned above, and the relative twist angle between the grains, the GBs can be classified into four simplified categories[83]. Symmetric tilt GBs are obtained when grains on either side of the GB plane can be described by the same Miller indices, such that the GB plane forms a plane of mirror symmetry. However, when grains form different angles with the direction normal to the GB plane, each grain will have a different Miller index and the GBs thus obtained are called asymmetric tilt grain boundaries. Twist grain boundaries are obtained when grains are rotated about the axis normal to the GB plane. Figure 3a) and b) show an example of the tilt and the twist grain boundary respectively. Grains in a 'real' system, however, have boundaries, when grains on either side of the GB plane are randomly oriented such that they have different Miller indices, and are rotated by different angles about the axis normal to the GB plane. Such grain boundaries are also called as general boundaries. Figure 3c) shows an example of grains as observed in a real system. In a real system, the chances of any two GBs being identical are extremely low. Such boundaries are extremely hard to be created on an atomistic scale, and have widely been studied in experimental work thus far.

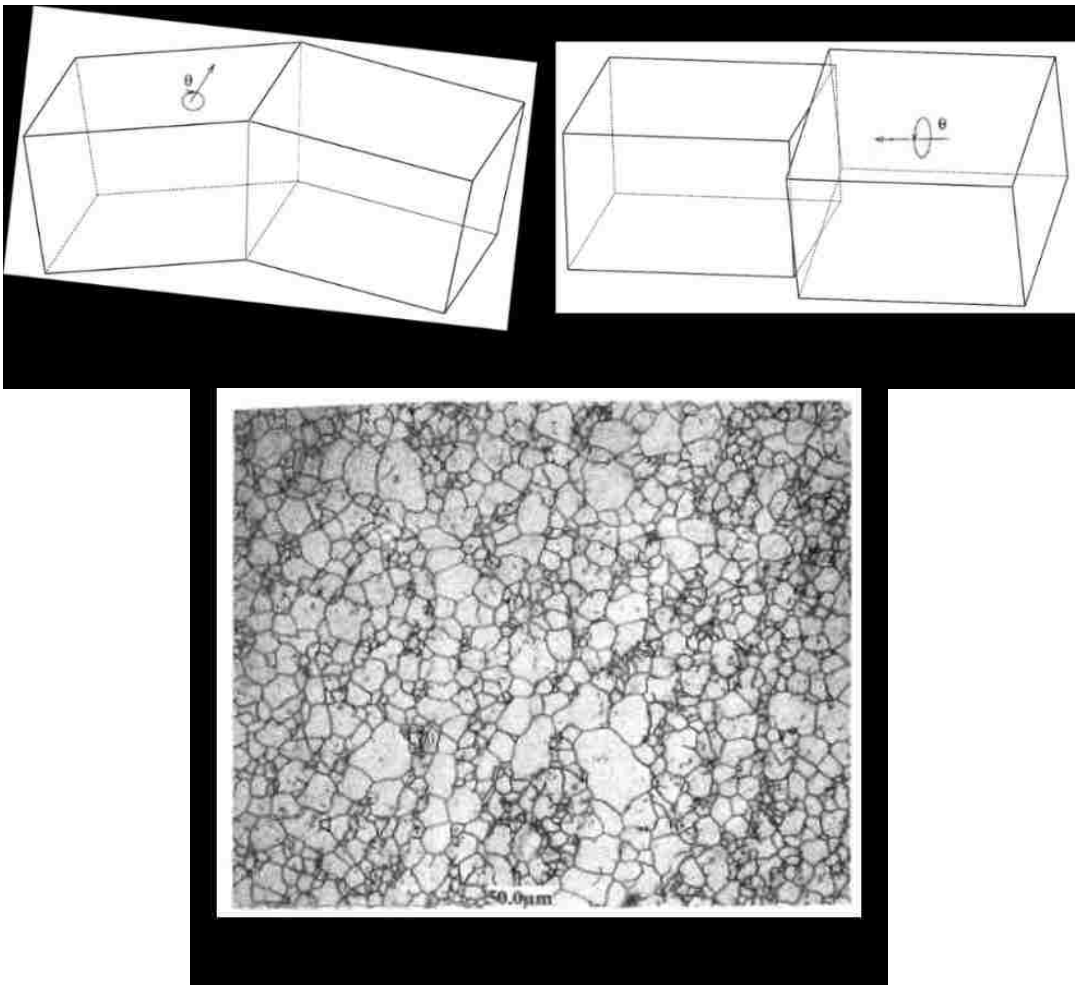

Figure 3: Example of a) tilt, b) twist and c) general grain boundary [82] Copyright © 2001 by John Wiley & Sons limited. (Reproduced with Permission)

MD simulations require an orthogonal simulation domain and thus creating general boundaries on atomistic scale would require an extremely large computational domain so that the lattice mismatch between the grains and the resulting stresses could be avoided. For example, for a GB with grains of periodic unit length $\sqrt{3}$ and $\sqrt{2}$ respectively we will need an infinite number of repeats on each grain on either side of the GB plane till we get the orthogonal edge of the simulation box to be the same length on either side of the GB plane. Furthermore, although the computational capabilities of the state of the art HPC resources has substantially increased in recent years, they are still insufficient to handle

general boundary system of this scale. As such, the scope of the work presented here has been limited to symmetric tilt grain boundaries. More details about the GB systems studied are provided in Section 3.3.

Other than the systems built with nano-grains to control the material properties, the GBs in a real system are also formed due to the presence of defects like point defects, line defects, and planar defects [85]. These defects disrupt the atomic arrangement in the lattice and therefore affect the bulk properties of the material. The presence of impurities also disrupts the lattice arrangement and this phenomenon is frequently exploited to enhance the material performance for specific applications like those in batteries and semiconductors. However, impurities have also been shown to migrate to the GB, which can have a detrimental effect on the macroscopic properties. Through a subtle control of chemistry, Harmer et al. [47, 48] created several different structures at the GB, also called complexion phases, which caused material strengthening and enhancement. The focus of this work is to understand why and how different impurities behave differently at the GB and if that can be used to maneuver the thermal transport across the GB

3.3. Grain Boundary Construction

The material of interest in this work is 3C-SiC (β-SiC), which has a Zinc blend structure. Such a structure can be visualized as two offset FCC lattices, one each for Si and C, such that each Si atoms is connected with four C atoms and vice versa. 3C-SiC primitive unit cell has 8 atoms (4 C and 4 Si), the bravais lattice can be built with primitive vectors: $a(1/2,1/2,0)$, $a(0,1/2,1/2)$, and $a(1/2,0,1/2)$ for a system with lattice constant a and axis along the low indices. The pairing carbon atom for each Si atom is offset by $a(1/4,1/4,1/4)$

from the corresponding Si atom. An infinite array of discrete lattice points can be generated by using the equation:

$$R = n_1\alpha_1 + n_2\alpha_2 + n_3\alpha_3 \tag{12}$$

where R is the array of lattice points, n_i are integers and α_i are the primitive vectors mentioned above. The atoms in 3C-SiC crystals have 'abc' stacking along the $[1\ \ 1\ \ 1]$ direction. In order to probe the impact of dopants at the GB, it was desirable to avoid stacking faults between the planes of atoms. As such, the crystals were modelled such that the $[1\ \ 1\ \ 1]$ direction was maintained along the Z axis and the other two orthogonal directions $[1\ \ 1\ \ \bar{2}]$ and $[1\ \ \bar{1}\ \ 0]$ were oriented towards the X and Y axis respectively.

3.3.1. Rotation Matrix and Crystal Orientation

In this work, five different misorientation angles (1.8038°, 3.9632°, 7.5891°, 12.2163°, and 16.1021°) are studied. Each of the stated misorientation angles is the angle that $[1\ \ 1\ \ \bar{2}]$ and $[1\ \ \bar{1}\ \ 0]$ vectors subtend to the X and Y axis, respectively. $[1\ \ 1\ \ 1]$ direction is the axis of rotation. For example, a mono-crystal with 7.5891° misorientation angle was created by using a code that determined that the vector $[6\ \ \bar{7}\ \ 1]$would subtend the requisite misorientation angles with the $[1\ \ \bar{1}\ \ 0]$ direction and subsequently the third orthogonal vector $[\bar{8}\ \ \bar{5}\ \ 13]$ was also calculated, keeping $[1\ \ 1\ \ 1]$ fixed. Rotation matrix was then created using the unit vectors along each of the three new and original directions as follows:

$$R(\theta) = \begin{bmatrix} \hat{i}_1 \cdot \hat{i}_2 & \hat{j}_1 \cdot \hat{i}_2 & \hat{k}_1 \cdot \hat{i}_2 \\ \hat{i}_1 \cdot \hat{j}_2 & \hat{j}_1 \cdot \hat{j}_2 & \hat{k}_1 \cdot \hat{j}_2 \\ \hat{i}_1 \cdot \hat{k}_2 & \hat{j}_1 \cdot \hat{k}_2 & \hat{k}_1 \cdot \hat{k}_2 \end{bmatrix} \tag{13}$$

here the unit vectors *i, j, k* are along the X, Y and Z axis respectively and the subscripts 1 and 2 represent the original and the new vector directions respectively. This rotation matrix when multiplied with the lattice array R in equation (12) gives the new lattice positions for the rotated monocrystal. An illustration of the rotated vectors and the lattice array are shown in Figure 4. Here the circles represent the atoms in a layer in the $[1\ \ 1\ \ 1]$ plane. In MD simulations, it is desired to maintain the periodicity in the system, particularly when studying the bulk properties like thermal transport. Lack of periodic boundary can result in undesirable surface effects. As such, when rotating the crystal, the grain must reside perfectly within the orthogonal cell. This can be achieved by ensuring that the magnitude of the new vector that defines the X or the Y axis, is large enough that the cell defined by the vector length reaches another atom that would represent the periodic pair of the atom at the origin of that vector. In other words, the new unit cell created with the rotated vectors must be repeatable in all three directions.

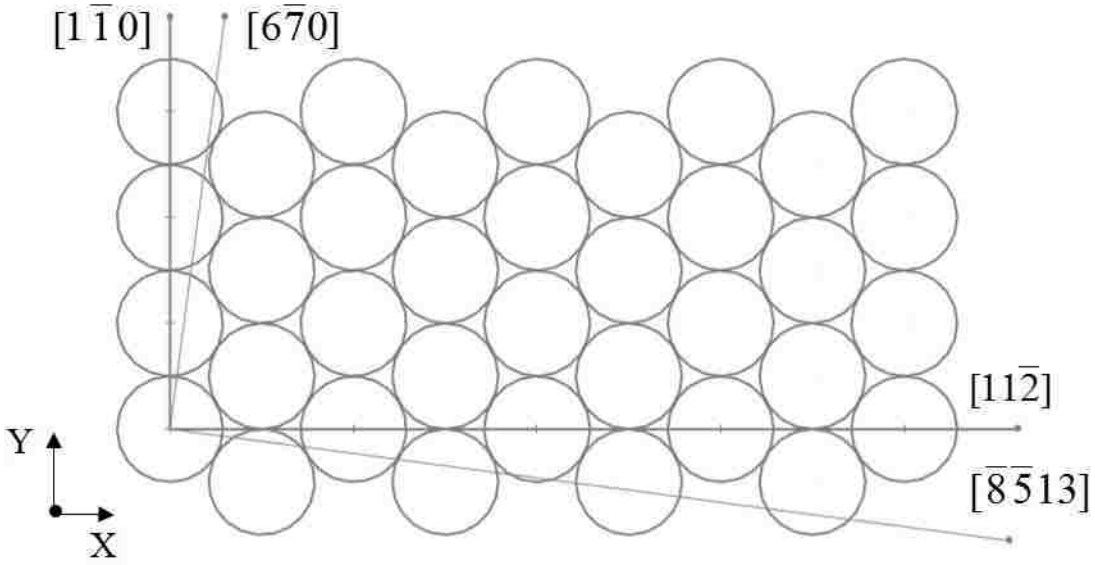

Figure 4: Schematic showing atomic arrangement is [1 1 1] plane for 3C-SiC.

The lattice constant used to form the initial crystal system is the zero-pressure value for the desired temperature, as determined from previously performed isobaric/isothermal (NPT) simulations using the Nosé-Hoover thermostat. This unit cell is then replicated in three dimensions to give a single rotated crystal system. This half crystal is then relaxed in constant volume/temperature (NVT) simulations for 40ps to allow for any artificial stresses in the system to be removed. Following equilibration, this half crystal was mirrored about the YZ plane to create a second half crystal, thus creating the GB between the two crystals. One such symmetric tilt GB system with misorientation angle of 7.5891° with the GB plane is shown in Figure 5. Here the light grey spheres are Silicon atoms and the darker grey atoms are the Carbon atoms.

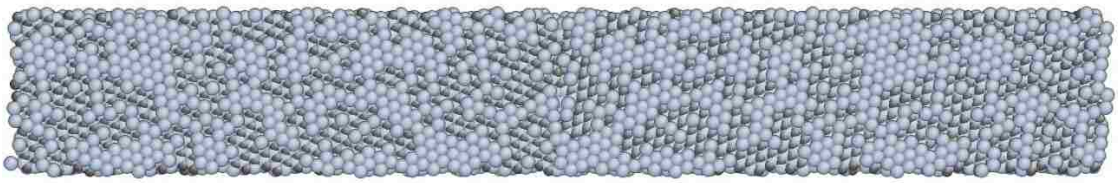

Figure 5: XY plane view of the symmetric 7.5891° tilt system (i.e., along [111]). With periodic boundary conditions at the ends, there are two GBs: one in the middle and one split at either ends.

A bicrystal created in this manner can often times be unstable. Since these systems are created artificially by placing two monocrystals adjacent to each other, there is a significant possibility that the atoms at the two GBs might not be at the equilibrium molecular separation distance from each other, i.e. can be closer to each other than the equilibrium bond length between the atoms. Such atoms are referred to as overlapping atoms. This can result in high interatomic forces between the atoms at the GB, resulting in ballistic movement of atoms which makes the system unstable. Also, when the grains are formed in a real material, the size and shape of grains continuously changes till the grains,

and the material in general attains a low overall energy. In the same line of thought, the GB created above might not be at the minimum energy system as the GB was not allowed to evolve for significant amount of time to equilibrate. Olmsted et al. studied the different GBs created by iterating over the microscopic DoF to determine the lowest energy configurations of the systems[86, 87]. The same procedures are followed to created symmetric tilt GB systems in this work.

3.3.2. Olmsted's Method and Microscopic Degrees of Freedom

Minimum energy systems are created in two steps. First, the problem of overlapping atoms is addressed. When creating a GB, since SiC is diatomic, there are three possible overlap possibilities: Si overlapping Si, C overlapping C, and Si overlapping C. The minimum equilibrium bond length between these combinations of atoms is determined from the lattice constant for 3C-SiC. The distance between atoms at both the GB is measured as a function of the minimum atomic bond length for each of the overlap possibility. Subsequently, atomic deletion criterion is determined as a percentage of the bond length. For example, consider the atomic deletion criteria of 85% of the bond length. The Si-Si and C-C bond length is given as $\left(\sqrt{2}/2\right)\times a$, while that between Si-C is given as $\left(\sqrt{3}/4\right)\times a$. C atoms that are determined to be closer to each other than 85% of the C-C bond length are determined, and the one closer to the GB plane is removed along with its pairing Si atom and vice-versa. Since each C atom is bonded to four Si atoms, the Si atom closest to the GB plane is regarded as the pairing Si atom for removal with C. The process is repeated for the overlapping Si-Si atoms and overlapping Si-C atoms as well. After all the overlapping atoms are removed, the energy of the system is minimized using the minimize routine in LAMMPS. This routine uses the Polak-Ribiere version of the

conjugate gradient algorithm and calculates the local potential energy minimum by iteratively adjusting the atom coordinates. The process is repeated for several deletion criteria between 0% and 90% of the equilibrium bond length. The GB energy, E_{GB}, is the internal energy of the boundary per unit area of the GB [86, 88]and can be calculated from the following equation:

$$E_{GB} = \frac{E_{System} - E_{Bulk}}{2A_{GB}} \tag{14}$$

where E_{System} is the potential energy of the system obtained from the energy minimization, E_{Bulk} is the potential energy of a bulk crystal with the same number of Si and C atoms as the GB system and A_{GB} is the cross-sectional area of the GB. Since we have two GBs in the system due to the periodic boundary conditions, the area of the GB also doubles. Hence, the factor 2 in denominator in the above equation. E_{Bulk} is also called as the energy of the ideal crystal used as a reference system. Such a system minimizes in a single iteration and can be used to calculate the energy per atom for the bulk system. This energy per atom, $Eatom_{Ideal}$, of the reference system can be used to calculate E_{Bulk} by multiplying it with the number of atoms, N, in the GB system. Equation 14 can then be re-written as:

$$E_{GB} = \frac{E_{System} - N \times Eatom_{Ideal}}{2A_{GB}} \tag{15}$$

Figure 6 shows the E_{GB} for symmetric 7.5891° GB system, at 500 K, for several atomic deletion criteria. From the plot, the deletion criteria which returned the minimum GB energy was determined to be 35%. Atomic deletion criteria of 30% and 40% of the equilibrium bond length were also selected for further evaluation using Olmsted's method. It was also observed that the bicrystals created with different lattice constant for different temperatures did not necessarily have the same atom deletion criteria. For each temperature

case, the lattice constant was determined individually and a new system was built from scratch each time. It is possible that temperatures altered the equilibrium position of the atoms at the GB, resulting in a different atomic overlap at the GB.

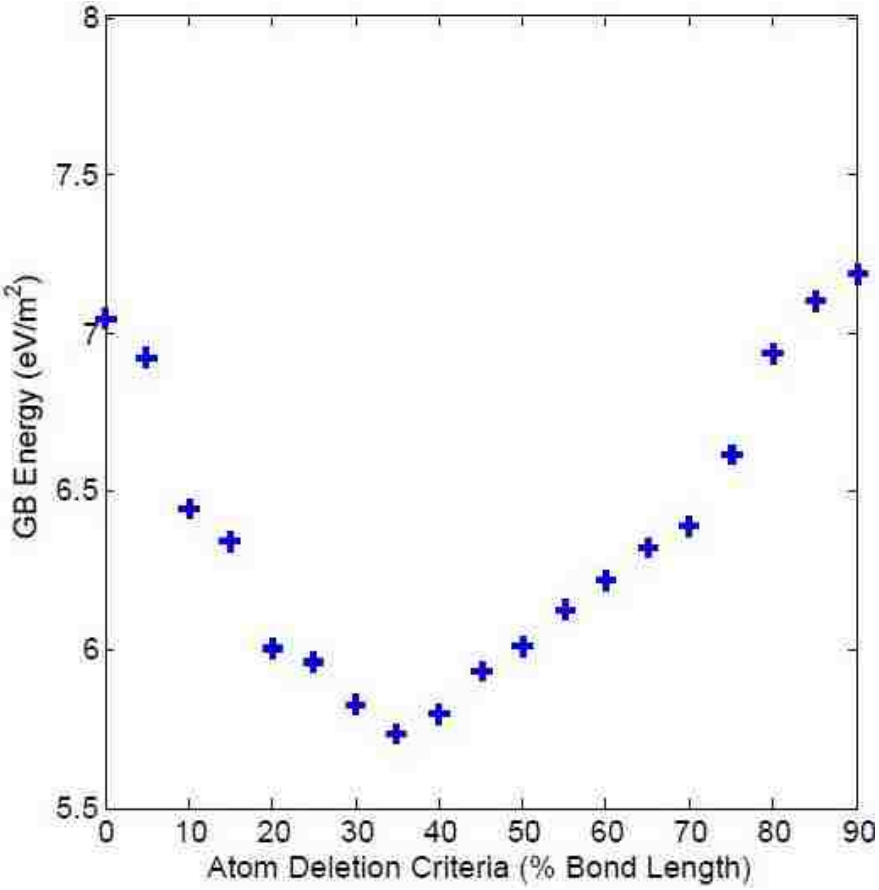

Figure 6: GB energy for 7.5891° symmetric tilt system, at 500 K, with different overlapping atom deletion criteria and zero lateral scroll.

The system obtained after removing the overlapping atoms might still not be lowest energy configuration. Therefore, in the second step, we take advantage of the microscopic DoF to translate one half of the bicrystal in the X and Y direction, while keeping the second half of the bicrystal fixed. Consider the schematic shown in Figure 7. Keeping the half crystal 'A' fixed, the half crystal 'B' is iteratively translated along the positive X and Y directions by 1 Å at a time. Keeping in mind the periodic boundary conditions applied in

both the X and Y directions, any atom that moves outside the simulation cell is wrapped back into the simulation cell by subtracting L_Y (upon crossing the Y simulation cell bound) and $L_X/2$ (upon crossing the X simulation cell bound). Subtracting $L_X/2$ in X direction ensures that the half crystal B does not lose atoms to half crystal 'A' and any atom leaving the outer GB returns to the central GB in half crystal 'B'.

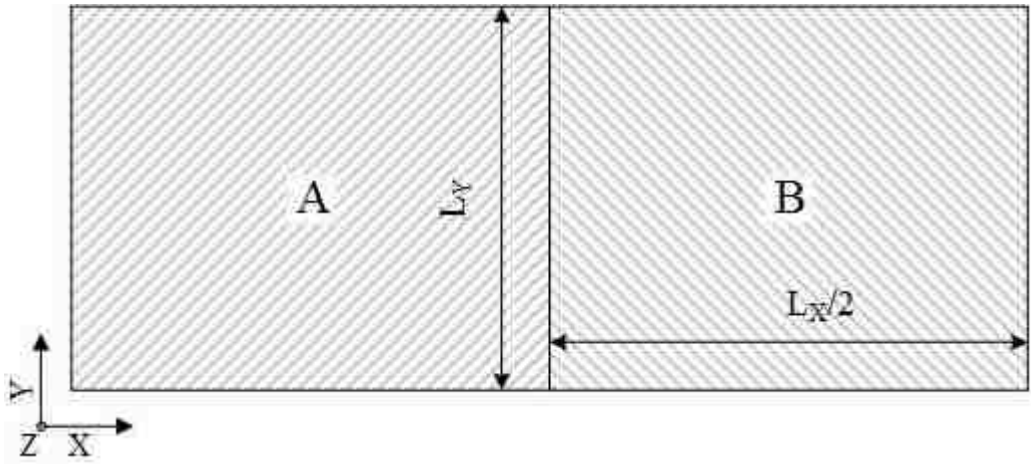

Figure 7: Schematic for obtaining low energy GB system by iterating over the microscopic DoF

Once the translation of atoms is completed, the minimum energy of the system is calculated for each of the three atomic deletion criteria from the first step. In other words, all the three atomic deletion criteria are tested for each translation in X and Y directions. It must be noted that the translation along the Z direction is not performed. As mentioned earlier, any rotation or translation along the Z direction can result in stacking faults in the 'abc' lattice arrangement and the focus of this work is to evaluate the impact of dopants on GB thermal resistance. The iteration over the entire half crystal lengths in X and Y direction can become computationally expensive for large systems. Therefore, the iterations are only performed for the periodic lengths of the unit cells. Any translation beyond that would be redundant as further translations in X or Y would produce identical crystal as previously

analyzed. The minimum energy for each of the iteration analyzed is then plotted for each of the atomic deletion criteria to determine configuration with the least energy. A plot for the analysis done for the symmetric 7.5891° tilt system at 500 K is shown in Figure 8.

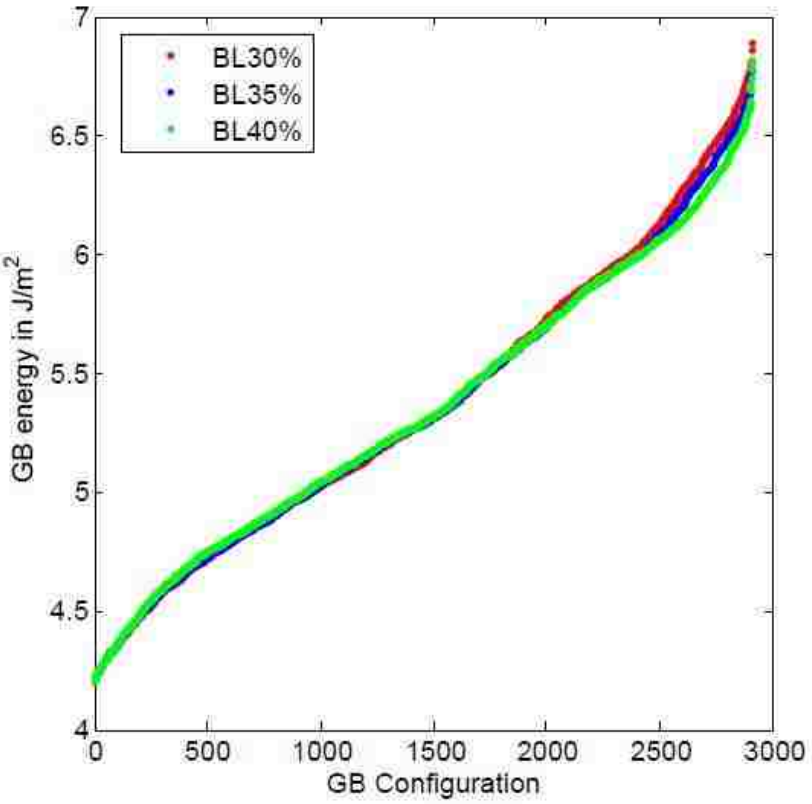

Figure 8: GB energy vs. GB configuration iteration (sorted by increasing GB energy) for atomic deletion criteria of 30%, 35%, and 40% of the equilibrium bond length in 7.5891° symmetric tilt GB.

Similar plots were obtained for all the tilt angle GBs studied in this work. It was observed that the GB energy for ceramic material was much higher than those in metals studied by Olmsted *et al*. [86, 87]. This observation can be attributed to the higher material stiffness for ceramics. It must be pointed out here that the minimum energy system, determined from the process above, might not be the absolute minimum energy configuration. One should ideally perform several more atomic overlaps in tandem with

iteration over the microscopic DoF or use Monte-Carlo methods to obtain true minimum energy systems. Once the minimum energy configuration was found, the GB system was constructed and allowed to relax using the minimization routine in LAMMPS. The system was then equilibrated using the canonical and the micro-canonical ensemble before turning on the dynamics and pumping flux in to the system as described in Section 4.2. R_k is relatively insensitive to system length at higher temperatures given the relatively short phonon mean-free paths and low-frequency phonon GB scattering[62], the system length was limited to L_X =27.6 nm perpendicular to the boundary.

3.3.3. Dopants at Grain Boundary

The foreign particles present in a material are often times alternately called dopants and impurities. However, impurities generally refers to the particles that are usually present from the processing and raw material stage, whereas, dopants refers to particles that are deliberately added in controlled concentration to obtain an intended beneficial effect on material properties. While the presence of impurities has detrimental effect on material properties, controlled doping is extensively used to obtain a host of benefits. For example, the presence of metallic dopants aids in increasing the electrical conductivity of semiconductors, or the most common observation vis a vis mechanical properties of alloys with different dopant concentrations[85]. The choice of dopants is most critical for any application as the addition of dopants can result in increased stresses in the system as well.

The focus of this work is to probe the effect of dopants on the thermal conductivity of the material. The two most commonly used dopants for SiC are Bismuth and Aluminum. However, in this study dopant atoms were modelled as Lennard Jones solid in order to steer clear of any chemical interactions between the matrix atoms and the dopant atoms. For

each symmetric tilt GB studied, the minimum energy system with the required tilt angle, created using Olmsted method, was used as the base system and dopant atoms were substituted into the atomic positions at the GB. More specifically, a Si atom was randomly selected close to the GB along with its pairing C atom to which it was bonded. Similar to atomic deletions criteria described in the previous section, if more than one pairing C atoms were identified, the C closes to the GB was determined as the pairing C atom. Each SiC pair was then removed, and a dopant atom was inserted at the Si atom's coordinates. It must be acknowledged that Monte Carlo method is the ideal method for dopant insertion but with the intent to observe only the impact of dopant concentration and dopant-dopant interactions, a random number generator was used to identify Silicon atoms close to the GB. The process is repeated to obtain the required dopant concentration at GB. For concreteness, dopant concentration is defined relative to the areal density of the $[1\ 1\ 1]$ plane. In particular, the number of LJ atoms in one $[1\ 1\ 1]$ plane of dopant atoms with the cross-sectional area 40 Å × 44 Å was calculated and denoted as one monolayer (1 ML). GB system with 7.5891° misorientation angle was the first and most extensively examined system in this study. The dopant concentration was thus calculated based on the plane of LJ atoms, with the same area of the cross section as that of the 7.5891° misorientation system as reference. In all simulations performed, dopants were inserted at each of the two GBs to maintain periodicity and several analyses were done with dopant concentration varying from zero to 1.007 ML. The different dopant concentrations studied are provided in Table 2. The other parameters varied include the dopant-dopant interaction strength as well as the mass of the dopant material as described in the later chapters.

Table 2: List of dopant concentrations studied. 1 ML = 432 LJ dopant atoms

Concentration (C) in ML	0.048	0.12	0.167	0.25	0.33	0.412	0.567	0.896	1.007
No. of dopant atoms	21	52	72	108	144	180	245	387	435

Chapter 4

4. Calculating Kapitza Resistance using NEMD

4.1. Introduction

In an isotropic crystalline material with a constant heat flux, q, maintained across its either ends, a temperature gradient is obtained in the direction of the heat flux and can be directly calculated from the Fourier's law: $q = -\kappa(dT/dx)$. Here κ is the bulk thermal conductivity and is dictated by two contributions: electronic heat conduction κ_e and lattice wave (or phonon) heat conduction κ_p (i.e. $\kappa = \kappa_e + \kappa_p$). In conductive materials (i.e. metals), electronic degrees of freedom contribute significantly to κ; however, for insulators and semiconductors, κ is largely determined by phonon contributions (i.e. κ_p). Phonons are elastic waves that propagate through the bonding network of an atomic assembly. Atoms at higher temperature have greater vibrational energy than atoms at lower temperature. In the presence of a temperature gradient, atoms transfer vibrational energy from hot regions to relatively colder regions through their interactions with nearby atoms. The energy carried by phonons is proportional to the phonon mean free path, which is the defined as the average distance of phonon propagation between non-momentum conserving scattering events. Nano-crystalline materials trim the bulk phonon mean free path by a few orders to the size of the grain, thereby effectively reducing the κ_p.

Alternately, phonon scattering at the GB can also be described through thermal GB resistance, R_k. When a constant heat flux is maintained across a GB, a characteristic

discontinuity exists at the GB, in the otherwise linear temperature gradient. The Kapitza resistance of a GB is obtained by dividing the magnitude of the temperature discontinuity ΔT by the imposed heat flux, q as follows: $R_k = \Delta T / q$. Several advances have been made for experimental determination of R_k [89]. However, the current knowledge of thermal transport at internal material boundaries is greatly limited owing to the inability to probe the transport behavior of a specific boundary and connect that behavior to the structure of the GB. Recent work using nanocrystalline assemblies demonstrated some promise to probe thermal boundary effects in experiment [90]. Theoretical attempts to describe thermal boundary resistance include the acoustic mismatch model (AMM) and the diffuse mismatch model (DMM) [91]. While both have proven useful for understanding some aspects of the phenomenon, they are unable to make predictions in agreement with existing experiments [92]. An alternate approach is to directly model thermal boundary resistance in atomic scale, MD simulations. The first such work in this area was advanced over a decade ago [66, 76], and this has been followed by many studies demonstrating the efficacy of this approach. The NEMD approach used for calculating R_k in the work presented here is described in the next section.

4.2. Procedure

All the simulations were performed using the Large-scale Atomic/Molecular Massively Parallel Simulator (LAMMPS), open source molecular dynamics package developed by Sandia National Lab [51] and a simulation time step size of 0.1 fs is used throughout. All the GB systems are built in the form of an orthogonal box as described in detail in the previous chapter. Once the system was built, the general procedure for

calculating R_k is the same for both the undoped and the doped systems. Figure 9 shows the 3D schematic of the simulation cell with the third dimension pointing out of the paper labelled as Z axis in the figure.

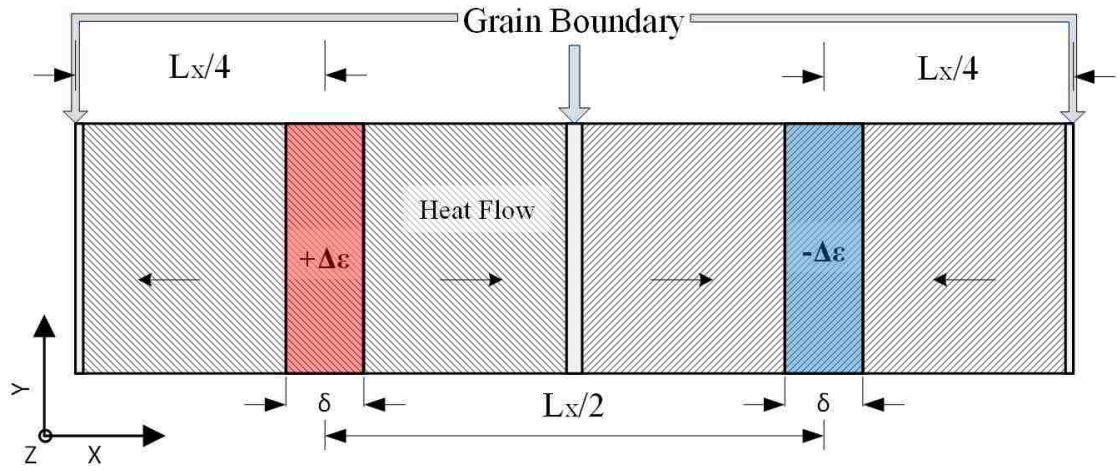

Figure 9: Schematic representation of three-dimensional periodic simulation cell for calculation of Kapitza resistance.

As mentioned earlier, R_k can be calculated from the temperature discontinuity at the GB, which in turn requires that the system be subject to a temperature gradient. There are two commonly followed techniques to achieve that, the EMD and the NEMD. The two methods were described very briefly in Section 2.5. In both the methods, the simulation cell is generally long along one dimension (along the X direction in this work) while the other two dimensions are much smaller. Each simulation cell contains a heat source and a heat sink in order to establish a heat current parallel to the direction of the longer dimension. In the EMD technique, both the heat reservoirs are maintained at the respective desired temperatures using a suitable thermostat and the system is evolved till a steady heat current through the system is established, i.e., the system reaches equilibrium. The thermal conductivity of the material can then be calculated using the heat current auto-correlation function (HCACF), which can in turn be used to determine the temperature drop at the GB.

(For the details regarding calculation of the heat current vector see Ref [53, 64, 93-95]). Significant amount of data is required to get good auto-correlations, thus making the simulations extremely long and often tedious. NEMD technique, used in this study, is much simpler to apply. In this technique, a known heat flux is generated by adding energy to the atoms in the heat source and removing the same amount of energy from the atoms in the heat sink at a pre-determined rate. In response to the heat current generate this way, a temperature gradient is obtained through the system.

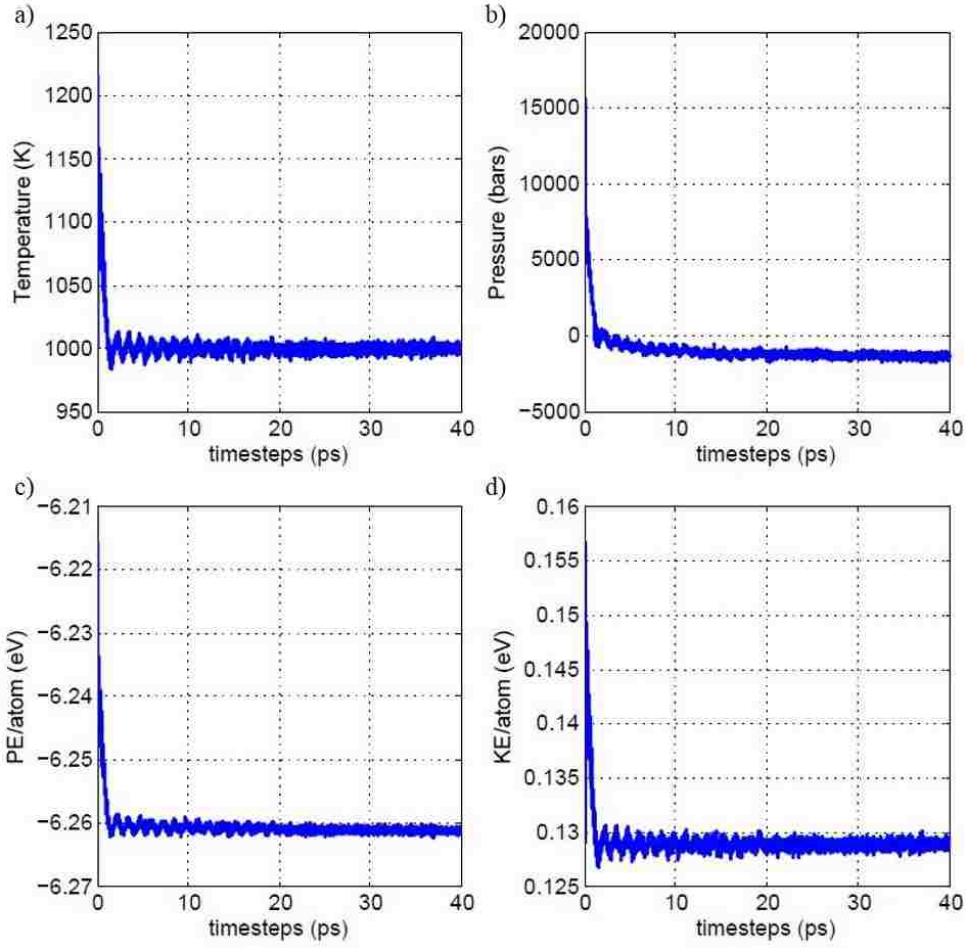

Figure 10: Plots for a) temperature, b) pressure, c) PE/atom and d) KE/atom in 7.5891° tilt GB system after NVT and NVE equilibration at 1000 K. Plotted on the same plot, first 20 ps show the evolution over NVT and the following 20 seconds show evolution over NVE.

The minimum energy system created using the Olmsted's method, as described in Chapter 3, is first allowed to relax at the desired temperature using the canonical ensemble for 20 ps. The relaxed system was then evolved with a constant energy at fixed volume for another 20 ps, and temperature and pressure plots are generated to ensure the system reached equilibrium. Figure 10 shows the temperature, pressure and energy plots for 7.5891° symmetric tilt GB system after the NVT and NVE equilibration at 1000 K. It is seen that the system is stable and fully evolved after the first 15 ps as both the Kinetic and potential energies as well as the temperature of the system appear to have reached a stable state. Also, the system has a negative pressure, indicating that the system is under tensile stress. This is due to the deletion of atoms from the atomic deletion criteria which creates some room for atoms at the GB to stretch the system. It was determined that the resulting strain in the system was negligible to cause any concern for the stability of the system. Further, turning on the dynamics in the system is also expected to relieve some of these stresses.

The schematic in Figure 9 also shows the general location of the heat reservoirs with respect to the GBs and the direction of the resulting heat current. Two slabs of thickness δ = 8 Å each are defined perpendicular to the X axis, centered at a distance $X = -L_x/4$ and $X = +L_x/4$ from the GB, with GB assumed at the $X = 0$. Here, L_x is the total length of the simulation cell. Notice a second GB is also present and is split at the either ends of the simulation cell. When Periodic boundary conditions are imposed on the system, it can be visualized as an infinitely long system with the two crystals (along with their respective reservoir) present alternatingly. The slab at $X = -L_x/4$ is treated as the heat source while that at $X = +L_x/4$ is treated as the heat sink. The atoms inside the slabs are

identified and a heat increment $\Delta\varepsilon$ is added by rescaling velocities at every MD time step to the atoms in the heat source slab and removed from the atoms in the heat sink slab, as described by Jund *et al*. [66, 78]. This method ensures that no artificial drift develops by conserving the total momentum of the slabs. This is achieved by adjusting the velocity of each atom, v_i, in the heat source and heat sink slabs with respect to the velocity of the center of mass, v_G, of the ensemble of atoms in the respective slab using the formula:

$$v_i = v_G + c\left(v_i - v_G\right) \tag{16}$$

$$c = \sqrt{1 \pm \Delta\varepsilon / \left(E_{KE} - E_G\right)} \tag{17}$$

where E_{KE} is the instantaneous total kinetic energy of the atoms in the slab and E_G is the kinetic energy associated with their center of mass.

The corresponding heat current is generated is calculated as $J = \Delta\varepsilon / 2A\Delta t$, where the factor 2 accounts for the flow of heat on either side of the flux, resulting in twice the surface area, A. The system is evolved for 4 ns with a simulation time step size of 0.1 fs, and the heat current moving from the heat source to the heat sink and a steady-state energy distribution is generally obtained between the 1 and 2 ns of the simulation. To calculate the local temperature, the system is divided into bins of equal length along *X*, and the average temperature in each bin, T_p, is calculated from the instantaneous kinetic energy, KE_P, of the N_P atoms in each bin using the equipartition theorem,

$$\frac{3}{2} N_P k_B T_P = KE_P \tag{18}$$

where k_B is the Boltzmann's constant. Bin-wise T_p samples were obtained every 100 time steps and averaged over 2 x 10^5 time steps, or 2000 temporal samples per bin. Time and bin averaged data were stored to memory, enabling subsequent additional temporal

averaging. At the high temperatures considered here, this classical determination of the temperature was determined to be satisfactory.

The averaging technique used for computing the temperature gradient and the temperature discontinuity developed at the boundary is illustrated in the two sets of sample data for undoped 7.5891° misorientation GB system. Figure 11 shows the average bin-wise temperature profile along the length of the system, perpendicular to the GB. The bin-wise temperature distribution was formed by post-process averaging over the temperature data generated for the final 1 ns of the simulation. As described above, this ensured that a steady state ensemble was sampled; furthermore, this significant temporal averaging resulted in a very small error. From Figure 11, it can be seen that the average error in temperature for each bin was less than 1 K.

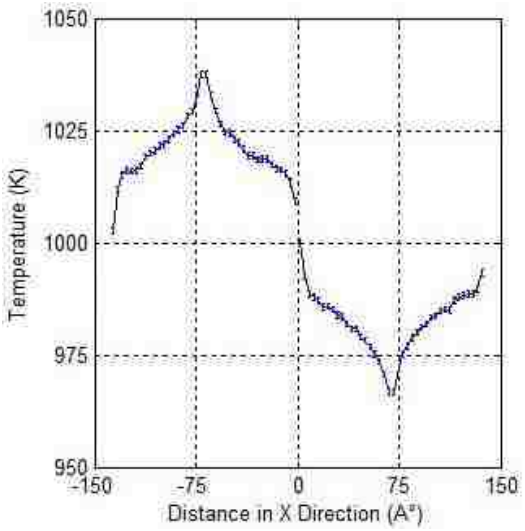

Figure 11: Time- and space-averaged temperature distribution in the undoped 7.5891° GB system at 1000 K generated from a total of 100,000 samples taken every 100 time steps.

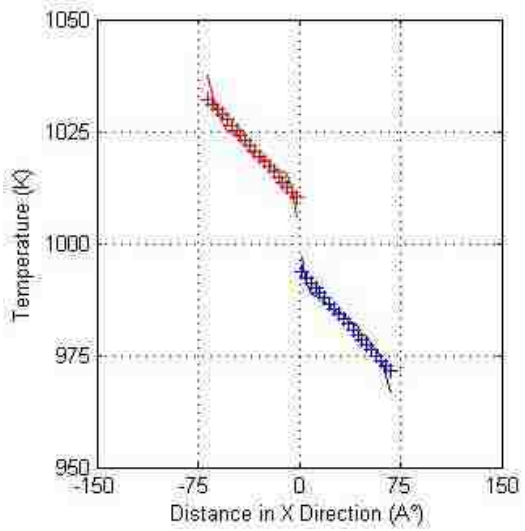

Figure 12: The temperature distribution obtained by averaging the data used in Figure 11 about the flux planes with the first GB located at X=0 Å

It can also be seen that non-linearities exist and that a discontinuous drop in temperature occurred across the GBs, as expected. In order to calculate the steady-state

flux, a region of width 10-12 Å was excluded on either side of the flux planes, depending on dopant concentration. Furthermore, given the symmetry of the system, data were averaged on either side of the heat source and sink planes (see Figure 12). These highly averaged data were then used to compute the Kapitza resistance via a least-squares fit of the temperature profile and determining the interfacial temperature jump, ΔT, and R_k is calculated by:

$$R_k = \frac{\Delta T}{J} \tag{19}$$

The same procedure was used for calculating R_k for the doped systems.

4.3. Sources of Error

While the NEMD is a straightforward and conceptually very simple approach, it requires careful consideration of several aspects for sound results. Some of these aspects along with the appropriate measures that were taken to address them are discussed below:

4.3.1. Periodic Boundary Conditions

In practice, periodic boundary conditions are generally applied in two different variations. While both the variations use periodic boundary conditions in the directions orthogonal to the direction of heat flux (parallel to the GB plane), one variation applies periodic boundary condition in the direction of the heat current as well (referred to as periodic system in this work) while the other doesn't (referred to as non-periodic system in this work). Figure 9 above is a schematic of a periodic system. A schematic of the non-periodic system is shown in Figure 13. In a periodic system a heat source and a sink are symmetrically spaced within the simulation cell, whereas in a non-periodic system, a heat source and a sink are placed at the ends with either ends terminated using a very thin layer

of atoms to cap the ends. The lattice positions of these atoms (in the end caps) are kept fixed, by reducing the velocity of the atoms to zero, throughout the simulation to prevent any loss of atoms across the boundary.

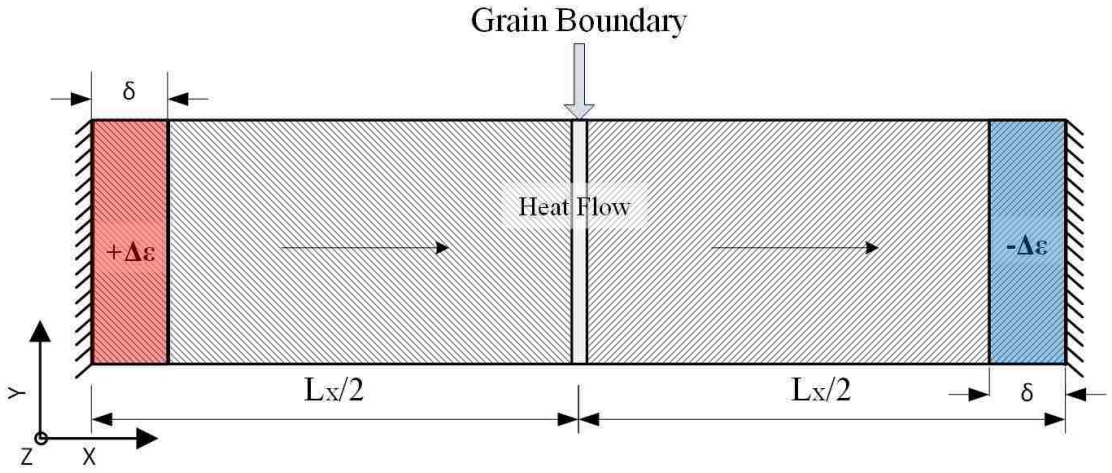

Figure 13: Schematic representation of Non-periodic simulation cell.

For a given sample size and number of atoms in the system, non-periodic boundary conditions allow for longer separation between the heat source and the heat sink, resulting in a longer temperature gradient for a better statistics. However, at the same time, it can also introduce scattering of phonons from the fixed boundaries which can cause artificial effects in the results. We use the periodic system in all our simulations as shown in Figure 9 as it provides two independent temperature gradients between the heat source and the heat sink, which can be used to obtain better statistics due to symmetry about the heat reservoirs (Refer temperature plot in Figure 11). Both options have been successfully used in several studies [66, 74, 76, 80, 96, 97]. The choice primarily depends on the finite size limitation for the materials, for example nano-wires; and the material properties like conductivity. Phonon dynamics are especially important when evaluating a semi-conductor material for thermal transport applications. In such a case it is deemed important to avoid

the unwanted phonon scattering from the fixed boundary in non-periodic system. It is reasonable to argue that a periodic system will have gradient regions of half the length compared to a non-periodic system, however, the system size has very limited effect on this work as explained in Section 4.3.2.

4.3.2. Simulation Cell Finite Size Effect

As pointed out earlier in the chapter, thermal transport in a material can either be due to the electrons or the phonons, depending on the material. In semiconductor materials where phonons are responsible for majority of the heat transfer in the material, one is ideally required to use simulation cells that are larger than the longest phonon mean free path. Simulations with cell size smaller than the phonon mean free path can result in scattering of these phonons at the interfaces of heat reservoirs. System size can limit the thermal conductivity of the system significantly. Chapter 5 discusses the thermal conductivity work done as a part of this study in more detail.

Although, previously explored finite size effects on R_k have provided reason to speculate that R_k is dependent on system size [32, 37, 80, 98, 99], its sensitivity to system size has not been established. The effect of system size on R_k depends on many factors like GB energy and type of GB interface[76], besides the material, geometry, and temperature. For example, Jones *et. al*. determined that while R_k was proportional to the ratio of lengths of the two monocrystals that comprise the bicrystal in low temperature regimes, it was insensitive to system size at high temperatures [62]. It is also determined that the presence of periodic boundary conditions in the directions orthogonal to the direction of heat current allows the phonons to travel freely across the simulation cell limits, thus making R_k independent of the cross-sectional area of the simulation cell [62, 66]. Since, majority of

the work performed in this study is at 1000 K, we expect the results presented here to be independent of any finite size effects. Therefore, the simulation cells were modelled such that each monocrystal was at least 14 nm × 4 nm × 4 nm. Refer Table 5 for specific system dimensions.

4.3.3. Size of Heat Reservoir and Rate of Heat Addition

The size of heat reservoir and the rate of heat addition have a non-trivial influence on the temperature drop between the heat source and heat sink. In MD simulations, it is not out of the ordinary to observe a temperature drop of the order of 100K or more for systems of size tens of nanometers. Although unreal, this kind of temperature gradient is needed because a large gradient can help minimize the thermal fluctuations and help achieve a steady state in a shorter simulation run time, i.e., reach convergence faster. However, the larger the temperature gradient, the larger the non-linearities in the system. The effect of non-linearities, as relevant to this work, is discussed in Section 4.3.4.

There are no established rules or standard practices for the size of the reservoirs. In the absence of widely accepted guidelines, we decided to size the thermal reservoirs big enough to comprise at least 4 planes of atoms. For a rotated system where discrete planes of atoms cannot be identified along the direction of rotation, the reservoirs width is kept constant at 8 Å. Planes of this width and spanning the entire cross-section of the simulation cell had more than 2000 atoms in them. Although the size of the heat reservoirs doesn't change the observed R_k at the GB, for a given rate of heat addition, small reservoirs can result in sharp rise of drop in temperature in the reservoirs resulting in an increase in non-linear temperature distribution in the region adjacent to the reservoir [81]. In a recent work published by P. C. Howell, it was observed that the size of the thermal reservoirs had

qualitatively similar effect on the temperature profiles for both periodic boundary systems as well as the non-periodic boundary systems.

Independent studies performed by Schelling *et al*. [66] and Zhou *et al*. [73] have demonstrated that the rate of heat flux does not have a significant affect the thermal conductivity of the crystal. In simulations for R_k, equation (18) indicates inverse relationship between heat flux and R_k. Also, the ΔT is also proportional to the heat flux. Higher the heat flux, more is the ΔT obtained at the grain boundary. As a result, the overall effect of heat flux on R_k is negligible. However, high heat flux causes increase in non-linearities in the regions adjacent to the thermal reservoirs. Therefore, the rate of heat flux was determined based on the area of cross-section of the simulation cell and the temperature of evaluation. It was also observed that the same heat flux resulted in greater non-linearities at low temperature of the order of 300K, for example, compared to the non-linearities in the analyses done at 1000 K. In this work, the energy added or removed from the thermal reservoirs was between 3 eV/ps – 17 eV/ps depending on the area of cross-section and the simulation temperature.

4.3.4. Non-Linearities

In the presence of thermal reservoirs, strong non-linearities are observed in the regions adjacent to the reservoirs. These non-linearities have been attributed to the increased phonon scattering caused by the heat source and the heat sink [66, 74, 75, 100]. These observations are particularly true for good thermal conductors. Thermal diffusivity of a material is directly proportional to the thermal conductivity as per the formula:

$$\alpha = \frac{\kappa}{\rho c_p} \tag{20}$$

here κ is the thermal conductivity, ρc_p is the volumetric heat capacity. As mentioned earlier, κ is affected by the size of the system. This in turn affect the thermal diffusivity from the thermal reservoirs to the rest of the simulation cell domain. Subsequently, the rate of thermal diffusion is not able to keep up with the high rate at which heat flux is added to, and removed from, the reservoirs. This results in thermally overdriving the regions adjacent to the reservoirs. Figure 14 shows the temperature distribution in the monocrystal that contains the heat source region. A similar distribution is obtained in the other monocrystal of the bicrystal system with the temperature dropping as we get closer to the heat sink.

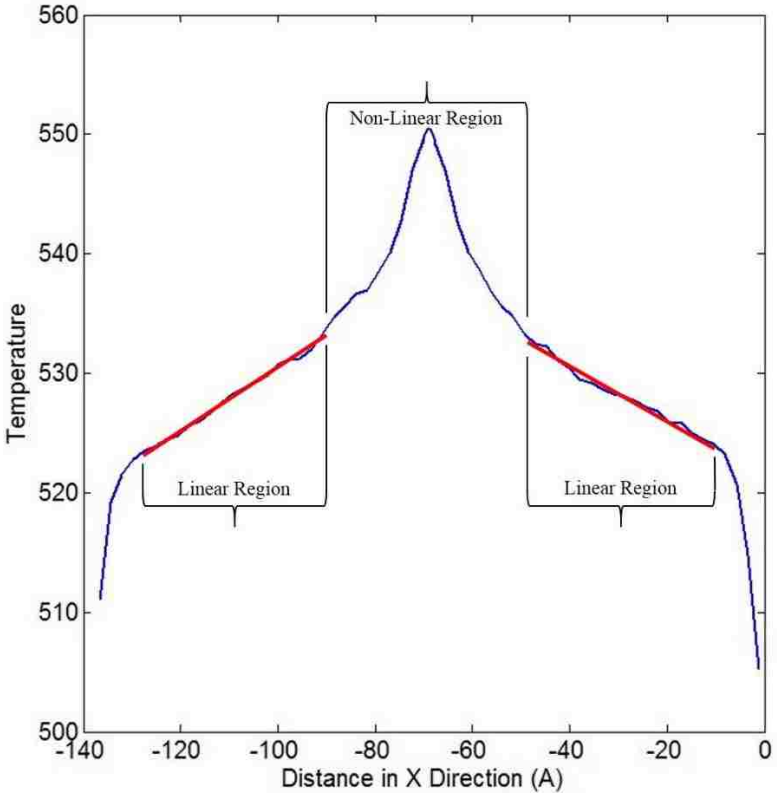

Figure 14: Non-linear and linear temperature regions of temperature distribution in 7.5891° symmetric tilt GB system at 500 K. Only one monocrystal has been shown in the figure here.

From the Figure 14, it can be seen that the non-linear regions slowly decay to produce a linear temperature gradient as we move away from the reservoirs, deeper into

the simulation cell. These non-linear regions must be excluded and all calculations must be performed on the section with a roughly linear temperature gradient in accordance with the Fourier's law. From Figure 14, it is also noted that there is no distinct boundary between the regions of linear and non-linear temperature gradient. Therefore, the choice of the width of excluded region is somewhat arbitrary. Howell performed a short analysis to determine the impact of the width of excluded region on the calculated thermal conductivity but a consistent result was not obtained between systems with periodic boundary conditions and those with non-periodic boundary conditions [81]. There are also some non-linearities in the temperature distribution in region adjacent to the GB. These non-linear regions are also excluded. In the work presented here, the width of excluded region was decided on a case by case basis. However, it was ensured that in all the analyses, the linear region selected for computation was more than half the length between the center of the heat reservoir and the GB.

4.3.5. Temperature Transients and Time Evolution of System Temperature

After the heat source and the heat sink are turned on, the well equilibrated system obtained after NVT and NVE equilibration starts evolving as the heat starts diffusing from the hot region to the cold region. The system takes some time for the thermal transients to subside and reach a steady state again. It is important to ensure that the data over the transient state are not included in the calculations. The time taken by the system to reach steady state depends on several system variables like the heat current, system dimensions, boundary conditions etc. It becomes even harder to predict the time taken to reach steady state for a system at nano scale due to the change in thermal conductivity of the material. Therefore, the traditional approach to avoid the temperature transients is to run the

simulation long enough to presume that the system reached a steady state, before gathering the data. In this study, all the simulations were run for a total simulation time of 4 ns. For each system developed a temporal evolution plot of temperature was generated to ensure that the system indeed reached a steady state condition.

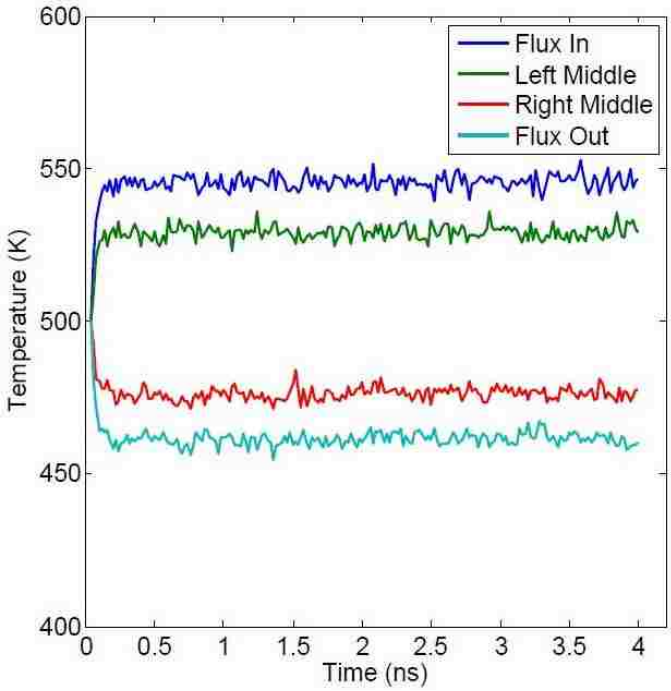

Figure 15: Evolution of temperature in simulation system in heat source (blue) and heat sink (cyan) regions as well as planes of width 8 Å in the middle of the GB and heat reservoirs on the hot (green) and the cold (red) side.

Figure 15 shows the evolution of temperature in a 7.5891° symmetric tilt GB system at 500 K. and shows the temperatures in 4 different regions, namely, the heat source or the flux in region (blue), the region in the middle of the heat source and the central GB (referred to as left middle in the plot and modelled in green color), the region in the middle of the heat sink and the central GB (referred to as right middle in the plot and modelled in red color), and the heat sink region (referred to as flux out in the plot and modelled in cyan color). For the majority of the simulations, the steady state was obtained with in the first 1

ns of simulation time. The simulation was allowed to evolve for another 3 ns and calculations were performed on the last 1 ns of the data. It must be noted here that the temperature plotted in Figure 15 is not the instantaneous temperature in the stated regions, but the temperature sampled over every 100 time steps for 2000 samples and averaged to gain good statistics.

4.3.6. Statistics and Error Bars

Molecular dynamics simulations use an extremely small simulation time step of the order of pico-seconds and femto-seconds. Since, it is currently impossible to observe heat flow at these timescales in an experimental setting, one can argue that the experimentally measured quantities are time averaged quantities. In Section 2.2, it was described how MD simulations apply Newton's law of motion to obtain discrete set of data for atomic arrangement in the simulation cell. The results obtained are the instantaneous positions and the corresponding energy of the system. However, the atomic positions obtained are normally distributed in accordance with statistical physics due to the NVE and NVT integrators used in the calculations. Even so, the instantaneous values cannot be directly used to predict the properties investigated and need to be time-averaged for comparison with experimental results.

P.C. Howell studied the different methods to calculate thermal conductivity in semi-conductor materials with good confidence intervals and determined that simulations performed over large simulation cells had smaller error when compared to smaller sized simulations run for much longer duration [101]. The simulation cell size in this study is limited to smaller sizes for the reasons elaborated in Section 4.3.2. Therefore, this work

relies on collecting samples over long simulation durations with sampling rates large enough so that the data is de-correlated to the values at the previous time step.

Averaging over the data is done in three different steps. In the first step, the averaging is done in parallel with the ongoing computation using LAMMPS. A data sample is collected every 100 time steps and stored to memory until 2,000 such samples are collected. These samples are then averaged to obtain the energy of each atom and printed to file. In the second step, 50 such files are collected between the 3 ns and 4 ns of simulation run time and for each file, the simulation cell is divided in to bins to calculate temperature as described in Section 4.2. The choice of number of bins is dependent of the choice of spatial resolution desired. While increasing the number of bin results in lesser number of atoms per bin and could result in higher noise in the system, choosing a few thicker slices can provide better spatial resolution. However, the two effects generally counteract each other [101]. We chose to divide the simulation cell into 52 bins, after excluding the non-linear regions. The temperature of each bin is an average over all the atoms in that bin. Subsequently, we take advantage of the symmetry in temperature gradient about the flux planes and the temperature distribution on either side of the reservoir is averaged to obtain temperature gradient between the two reservoirs and calculate R_k. This is repeated for each of the 50 data files and the data is stored to memory. In the third and final step, mean R_k and its standard deviation are calculated using the least squares method over the 50 data files. This amount of averaging is determined to be very significant and the error bars obtained for the results were extremely small. Figure 11 shows the temperature distribution obtained in 7.5891° symmetric tilt GB system where the error bars can barely be identified as minor indentations in data.

Chapter 5

5. Thermal Conductivity of β-SiC

5.1. Introduction

It is long since known from experiments that the thermal conductivity of crystals depends on the size of the crystal examined, due to the confinement of the bulk phonon mean free path. This phenomenon is referred to as the Casimir limit [66, 75]. With the advent of nano-technology and advancements in manufacturing technologies, several applications like space technology, data servers, and many more area that use semi-conductors, are observing a shrinking in equipment sizes. Even larger devices are designed to obtain benefits from nano-technology through material grain structures customized for the said application. Thus, much effort is being spent on developing multi-scale methodologies to extend techniques from nano-scale regime to macro scale. One example would be the thermal conductivity in nano-structured material. By thoroughly understanding the thermal transport in nano-grains, one can obtain a parametric equation that can be used in finite element models to describe the thermal conductivity of individual grains in a material. This equation can be built so as to account for the grain size as well as structure. Subsequently, finite element method can be used to calculate the effective thermal conductivity of a material with nano-grains. Although non-trivial, the development of methods that would enable such multiscale modeling are already a hot topic of research in computational modeling. In this chapter, we strive to predict the thermal conductivity of

β-SiC and in the process describe the finite size effects as relevant to MD simulation systems.

5.2. Simulation Cell Size Effects and Matthiessen's Rule

The flow of heat by phonons can be obstructed by other phonons, electrons, impurities and boundaries or defects. At higher temperatures, the phonon-phonon Umklapp processes limit the phonon mean free path to a much smaller value, making the size effects irrelevant. Therefore, κ is not expected to vary significantly with the system size as high temperatures. However, at lower temperatures, the reduction in system size to lengths comparable or smaller than the phonon mean free path in an infinite system (bulk), limits the mean free path of phonons, causing them to scatter at the surfaces or edges [102]. System size effects or Finite size effects become even stronger in computer simulations of nano-scale systems as briefly discussed in Section 4.3.2. One way to deal with this phenomenon is to perform simulations for several different system sizes and extrapolate the κ calculated for a system of infinite size as described by Schelling *et al*. [66]. It is assumed that the Matthiessen's rule can be used to determine effective phonon mean free path, λ_{eff}, in the system of given size L_x, from the phonon mean free path in the bulk (or a system of infinite length), λ_{∞}, and the effect of the finite length of the system, as per the equation:

$$\frac{1}{\lambda_{eff}} = \frac{1}{\lambda_{\infty}} + \frac{4}{L_x} \tag{21}$$

here, factor 4 with the boundary scattering term depends on the way the simulation is set up. Figure 16 shows the schematic of the simulation cell used for the calculation of κ and it can be seen that the phonons travelling between the heat source and the sink will travel

an average distance of $L_x/4$ before scattering at the heat reservoir. From the kinetic theory, κ is given by [103]:

$$\kappa = \frac{1}{3} C_v v L_x \tag{22}$$

where C_v is the heat capacity per unit volume, v is the phonon velocity and L_x is the phonon mean free path. Equation (21) can then be restated as:

$$\frac{1}{\kappa} = \frac{3}{C_v v}\left(\frac{1}{\lambda_\infty} + \frac{4}{L_x}\right) \tag{23}$$

The above equation suggests that by plotting $1/\kappa$ vs $1/L_x$, finite size effects can be avoided. As $L_x \to \infty$, $1/\kappa$ will attain a constant value based on the phonon mean free path in the bulk for the material, and can in turn provide the bulk thermal conductivity. This method has been verified and used in many works [66, 75, 104, 105]. In a different study, Sellan *et al*. [80] applied Matthiesen's rule to draw the system finite size effects on κ, and using the Taylor series expansion approximated a relationship similar to that drawn by Schelling *et al*. [66]. We use the same method to calculate the thermal conductivity of β-SiC at 500 K to verify the Tersoff's interatomic potential by comparing with the results obtained by Porter *et al*. [67].

5.3. Interatomic Potential Validation

There are several empirical potentials developed for the matrix material, SiC, and a comparative study of these potentials was performed by Crocombette *et al*. to assess their thermal transport behavior [106]. We employ a modified Tersoff potential based on a parameterization by Porter *et al*. [55] as it accurately reproduces the observed acoustic phonon spectrum [67]. Tersoff used the parameters from pure elemental Si and C to

describe the interactions between elements in SiC [61]. Porter *et al* pointed out that unlike elemental Si and C, since each Si atom in β-SiC is bonded to a C atom (and vice versa) to form a *Zinc Blende* structure, the choice of parameters could result in a weakening of the Si-C bond due to the second neighbor Si atoms falling within the cut-off distance (especially at higher temperatures). In the event that the second neighbor Si atoms falls within the cut-off distance, the effective coordination number of Si atom can potentially jump up to 16 from 4 originally. This could significantly increase the energy of the neighboring atoms, while the extent of impact would depend on the proximity of the second neighbor Si to the SiC pair. In order to prevent this, Porter et al. suggested the cut-off distance should be reduced to exclude all Si-Si interactions.

The modified Tersoff's potential has been validated by calculating the thermal conductivity of β-SiC at 500 K [67, 105]. A similar evaluation was performed as a part of this work. Thermal conductivity of β-SiC was calculated using the modified Tersoff potential with the cut-off distance reduced to 2.65 Å (as alluded to in Section 2.4.1). The simulation set up for calculating κ is similar to that for calculating R_k, with the exception that the simulation consists of only one monocrystal. The crystals are oriented such that the X, Y, and the Z axis correspond to the (1 0 0), (0 1 0), and the (0 0 1) directions. Simulations are performed on systems of varying lengths along the X direction, as detailed in Table 3, and each simulation system is 10 × 10 unit cells in the transverse direction.

Table 3: Dependence of κ on system size using NEMD method

Dimensions	L_x (nm)	L_y (nm)	L_z (nm)	Number of Atoms
48 × 10 × 10	20.6	4.3	4.3	38,400
96 × 10 × 10	41.2	4.3	4.3	76,800
144 × 10 × 10	61.8	4.3	4.3	115,200
192 × 10 × 10	82.4	4.3	4.3	153,600
240 × 10 × 10	103.0	4.3	4.3	192,000
288 × 10 × 10	123.6	4.3	4.3	230,400
336 × 10 × 10	144.2	4.3	4.3	268,800

The lattice constant was obtained from zero-pressure value from isobaric/isothermal (NPT) simulation at 500 K using the Nosé-Hoover thermostat. Each system created, was then relaxed at 500 K using the canonical ensemble for 20 ps. and then further evolved with a constant energy & constant volume NVE ensemble for another 20 ps. Periodic boundary conditions were applied in all three directions and the method by Jund and Julien [78] was used to develop a heat current through the system as shown in Figure 16. The width δ of thermal reservoirs was chosen such that the edges of the flux region did not split planes of atoms. The number of planes of atoms that comprised the flux region was determined by the applied heat flux as explained in Section 4.3.3. For larger

systems, heat flux value used was generally higher to ensure that the system reached steady state within 1 to 2 ns of simulation time.

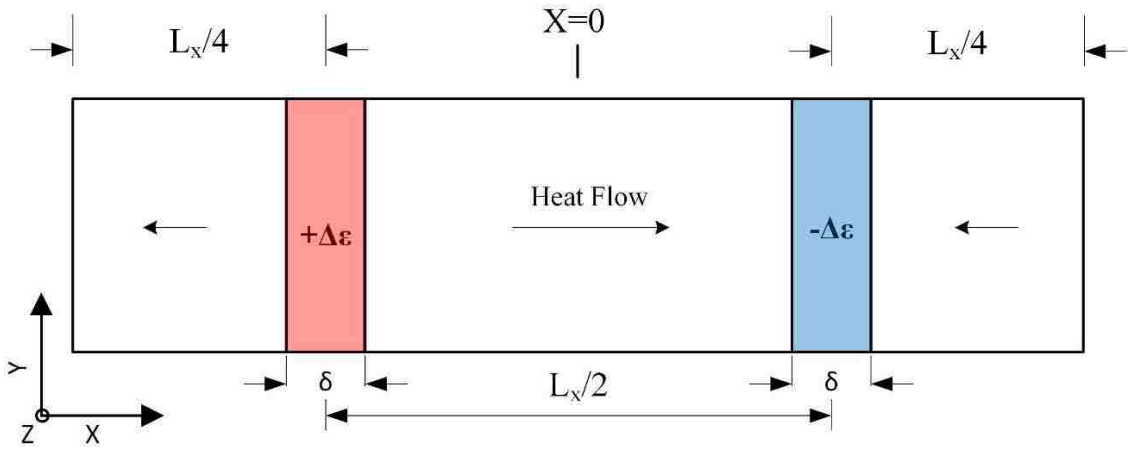

Figure 16: Schematic representation of three-dimensional periodic simulation cell for calculation of Thermal Conductivity.

The simulations were run for a total of 4 ns using a time step of 0.1 fs. Such a small time step was used to prevent any velocity drift in the system. A steady-state energy distribution was generally obtained between the 1 and 2 ns of the simulation time. Subsequently, the temperature distribution across the length was obtained using the Equipartition theorem as described in detail in Section 4.2. The final temperature distribution was obtained by averaging over the data generated for final 1 ns of the simulation. The averaging performed provided good statistics as the error bars on the data points obtained were very small. The $1/\kappa$ calculated for the seven different systems is plotted against the inverse length, $1/L_x$, for each system in Figure 17. A linear relationship between $1/\kappa$ and $1/L_x$ is observed in the plot. The intercept obtained by extrapolating the fit determined κ = 125 W/mK at 500 K temperature. The error bars provided on the plot show the observed standard deviation in the value of thermal conductance for each simulation and were mostly smaller than the size of the symbols on the plot. The bulk value obtained

is less than the experimentally measured κ ~ 210 W/mK at 500 K [67]. However, other published MD calculations for κ for β-SiC have reported similar values of bulk κ using the same potential and parametrization [105, 106].

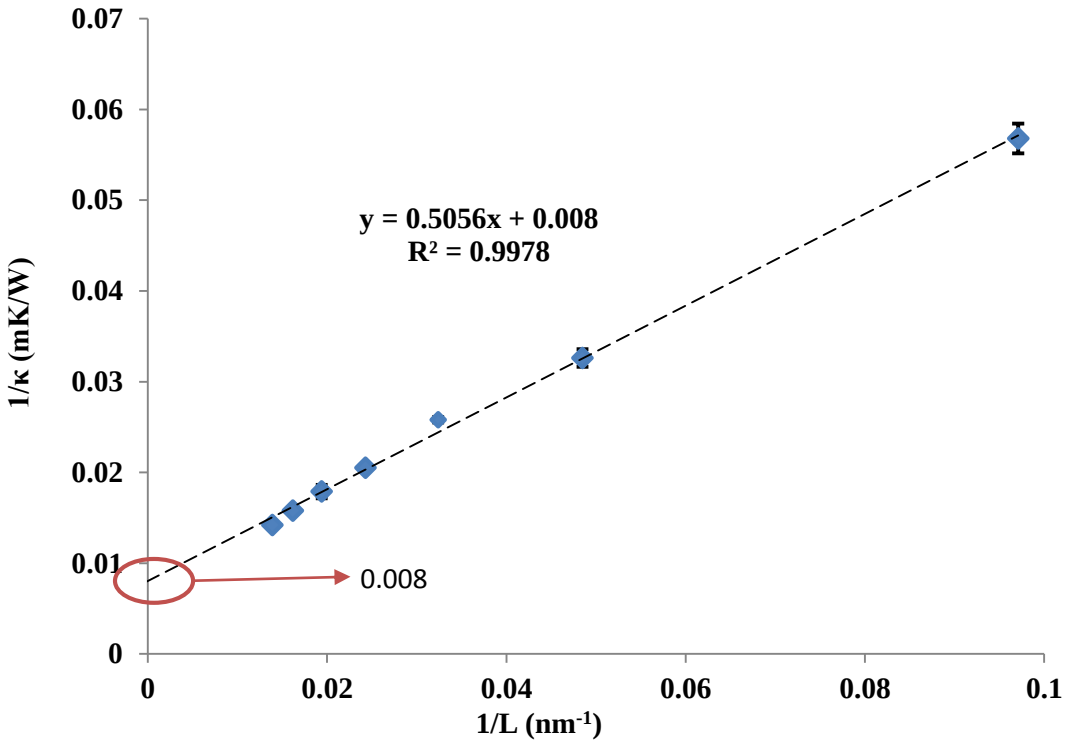

Figure 17: System size dependence of 1/κ on $1/L_x$ for β-SiC at T=500K using modified Tersoff's potential. Some error bars are of the size of the symbol and are therefore not visible.

There are several reasons for the under-prediction of κ from NEMD simulations. Besides the description of the interatomic potential used, Schelling *et al*. [66] pointed out that though, the phonons should not be scattered at the boundaries with the periodic boundary conditions applied in the directions perpendicular to the direction of heat current, in order to obtain κ within 10% of the bulk value, systems with size at least 10 times that of the bulk phonon mean free path would be required. Another reason is the classical nature of MD simulations as explained in the next section.

5.4. Quantum Effects and Temperature Correction

The Debye temperature for β-SiC is ~1200 K. Therefore, at lower temperatures where temperature effects on Bose-Einstein distribution are more significant, the quantum effects on phonon mode population become important. Including the quantum effects in MD simulations is an extremely difficult task. Several models have been proposed to correct the MD simulation results to include quantum effects. One such method is by scaling the MD temperature to real temperature [55, 67, 93]. In MD simulations, the total system energy in a harmonic system of N particles at temperature T_{MD} is given as:

$$E = 3(N-1)k_b T_{MD} \tag{24}$$

The MD simulation temperature T_{MD} can then be directly related to the real temperature T_{real} by equating the total energy in equation (24) to the energy of a quantum phonon system.

$$3(N-1)k_b T_{MD} = \sum_k \hbar\omega_k \left(\frac{1}{2} + \frac{1}{\exp(\hbar\omega_k / k_b T_{real}) - 1} \right) \tag{25}$$

where $\hbar$ is Planck's constant divided by 2π and ω_k is the k^{th} normal mode frequency. For the simulation setup used to calculate κ, the heat current, J_q, can be assumed to be the same as one would observe in an experiment to obtain the relationship:

$$J_q = -\kappa_{MD} \nabla T_{MD} = -\kappa \nabla T_{real} \tag{26}$$

$$\kappa = \kappa_{MD} \left(\frac{dT_{MD}}{dT_{real}} \right) \tag{27}$$

here dT_{MD}/dT_{real} is the gradient correction that must be multiplied to the κ calculated from MD simulations. These temperature corrections were however not performed on the κ

calculated in this study as the primary focus of the work is determination of Kapitza resistance R_k.at the grain boundaries in nanostructured system.

5.5. Summary

Thermal conductivity of β-SiC was calculated using non-equilibrium MD method at 500 K. Tersoff's potential was used to describe the interactions between Si and C atoms. Slight modifications were made to the cut-off distance in the interatomic potential file to completely ignore second neighbor interactions based on the parametrization proposed by Porter *et al*. [55]. Finite size effects were observed due to the presence of thermal reservoirs which reduced the largest allowed phonon wavelength in the system significantly. Matthiessen's rule was applied to extrapolate the results obtained from simulations of multiple system sizes and the bulk thermal conductivity was obtained as 125 W/mK. Although less than the experimentally obtained bulk thermal conductivity of β-SiC, opportunities to get better agreement with experimental results exist by making further improvements in the interatomic potential by including the explicit electronic structure effects. However, the results obtained are sufficiently encouraging to use the "modified" Tersoff's potential to study thermal interface Kapitza resistance in β-SiC.

Chapter 6

6. Effect of Grain Boundary Segregation

6.1. Introduction

The interface between dissimilar materials has been known to produce thermal resistance due to the difference in the densities of the two materials. The thermal resistance is results of mismatch in the speed of sound through the material on either side of the interface. This observation intuitively gives rise to the idea of thermal resistance from the GB interface in nano-structured material as they should also cause a similar interruption in the propagation of phonons through the material. However, the interaction of the phonons with the GB interface is much more complex, as the phononic transmission can be interrupted due to multiple factors like point defects or lattice defects in the crystal, presence of dopants, and vacancies. While, each of these factors might cause phonons to scatter to different extents, it is nevertheless important to elucidate the correlation between GB structure resulting from these defects and the thermal transport properties, to be able to tailor make the material with required thermal properties per the specific application requirements. Interpretation of the contributions from individual defects from experimental observations can be difficult as they are hard to de-convolute from each other. MD simulations are proven to be suitable for studying these issue as they allow to study each defect individually. In this Chapter, we explore how dopants with different strengths of interaction affect the GB structure and its subsequent effect on the GB resistance. The

observations are explained using structure factor calculations and the atomic number density at the GB.

6.2. Kapitza Resistance for Undoped Grain Boundary

Crocombette *et al*. [34] employed the Tersoff potential with the parametrization proposed by Porter *et al*. [55] to study the thermal resistance of different symmetric tilt GBs in β-SiC. They observed that the R_k changed significantly with the tilt angles for low angle GBs while the change in R_k was inconsistent for the large angle GBs. They created low angle boundaries by inserting edge dislocations, and used a shift procedure to create low energy high angle boundaries. More importantly, they analyzed symmetric 8° tilt angle boundary created by both the edge dislocation as well as the shift procedure. Although the 8° tilt boundaries created using the two methods had a significant difference in the GB energy, they measured the almost the same R_k for both the cases. Using the work done by Crocombette *et al* as foundation, 8° symmetric tilt angle was used to study the impact of dopants at GB. In our work, the exact angle of the tilt boundary is 7.5891°. The GB was built with the lattice constant at 1000 K using the procedure outlined in Section 3.3. The undoped system was studied first. Using the simulation set up schematic shown in Figure 9, a heat increment $\Delta\varepsilon = 8\text{x}10^{-4}$ eV was added by rescaling velocities at every MD time step in a thin layer of width $\delta = 8$ Å centered at $X = -L_x/4$ and removed from a layer of same thickness at $X = +L_x/4$. This manifested a heat current flowing from the hot reservoir to the cold reservoir. The system was evolved for a total of 3.6 ns and a steady-state energy distribution was obtained between the first 1 and 2 ns of the simulation time. R_k was calculated at the GB by measuring the temperature drop at the GB, obtained by calculating

the temperature distribution through the length of the system using Equipartition theorem. More detailed specifics of the procedure are provided in Section 4.2.

Figure 11 shows the temperature distribution in the undoped 7.5891° symmetric tilt angle GB system at T =1000 K. R_k was calculated from the intercept at the GB by extrapolating the slopes in the average temperature distribution in Figure 12. For this GB system R_k was calculated to be 5.8×10^{-10} m^2K/W. The average error for R_k was $\pm 0.3 \times 10^{-10}$ m^2K/W for this undoped GB system. R_k was calculated for the second GB as well and difference between the measured R_k for the two GBs was determined to be negligible. For the 8° tilt system at 300 K, Crocombette *et al*. measured $R_k \sim 4.6 \times 10^{-10}$ m^2K/W. The authors noted that at a temperature of 1273 *K,* the R_k was half the value of obtained at 300 K. The R_k at 1000 *K* should therefore lie between these two values for their system and in the absence of confidence intervals, the results obtained in this work for the undoped system are within the statistical error. It should be noted that there are some differences in the GB creation methodologies such as different temporal and spatial averaging procedures and different boundary conditions as Crocombette *et al.* employed a free surface boundary condition whereas we employed a periodic boundary condition. Nevertheless, the results are still in good agreement with each other.

6.3. Effect of Dopants on Kapitza Resistance.

The presence of dopant atoms has been shown in earlier low-temperature studies to alter the Kaptiza resistance. In particular, impurity mass, concentration, and the bond strength have been identified as important factors in determining Kapitza resistance. Duda *et al*. [45] observed that for a given set of parameters defining the impurities, R_k increased

non-linearly with the increase in impurity concentration. They also determined that the strength of bonds between impurity atoms did not have a statistically significant impact on R_k. In the simulations performed by Duda and company, the strength of interaction between the impurity atoms and the matrix atoms were calculated from the Larentz Bertholet mixing rules. Given the importance of GBs in determining R_k, it is of interest to investigate the impact of boundary segregation on the resistance. Dopant atoms preferentially segregate to GBs owing, for example, to the elastic driving force associated with a relative size mismatch with lattice atoms [47-50].

In this Chapter, doped GBs are evaluated at 1000 K. Dopant atoms are preferentially inserted at the GB by replacing a SiC pair as described in Section 3.3.3. Described as LJ solid, the zero energy separation distance between the dopant particles and the strength of interaction between dopant atoms were held fixed at σ = 2.0 Å and ε_{dd} = 0.3 eV, and two cases of dopant/matrix interaction, ε_{dm}, were explored: In one case the dopant/matrix interaction strength is the same as that of the dopant/dopant interaction (strong interaction case) ,and in the second case, the dopant/matrix interaction strength is one tenth that of the dopant/dopant interaction (weak interaction case). The concentrations employed here range from C = 0.048 to C = 1.007 ML. We note that, although the time scales of the simulation do not permit long-ranged diffusion, dopant atoms with a radius comparable to that of a Si atom will have considerable mobility at the GB and enable structural changes. These structural changes at GBs in the simulations occur over 1 to 2 ns and T data used for computing R_k were obtained well after GBs reached a steady state. The percent error in R_k for doped systems was estimated to be 3% on average at low concentrations and less than 1% at high concentrations.

Figure 18 illustrates the atomic arrangement of dopants and matrix atoms at one GB (located at $X = 0$) for the weak interaction limit (a_1 through a_5) and for the strong interaction limit (c_1 through c_5); images are shown for (from top to bottom) $C = 0.048$, 0.167, 0.33, 0.567, and 1.007 ML at 3.2 ns for the constant heat flux simulation. Two distinct morphologies were evident. In the weak interaction limit, dopant atoms rearranged to form clusters whereas, in the strong interaction limit, dopant atoms remain more spread out forming layers like distribution. At the highest concentration studied, the size of the cluster shown for the weak interaction limit was approximately 2.5 nm in *Y* by 4 nm in *Z*; for the strong interaction limit, dopants were distributed fairly evenly across the entire GB plane. Also shown in Figure 18 are the corresponding density profiles perpendicular to the boundary plane, b1-b5 for the weak interaction limit and d1-d5 for the strong interaction limit. It is evident from these figures that as dopant concentration increased, dopant atoms increased their extent in *X* for both weak and strong interaction cases; however the extent in *X* was somewhat larger for the weak interaction case. The full-width at half-maximum of the dopant density distribution at the highest concentration is approximately 0.35 nm for the strong interaction case and approximately 0.5 nm for the weak interaction case. Hereafter, the weak and strong interaction cases are referred to as clustered and layered cases. As the resulting segregation profiles are qualitatively similar for the well-separated GBs after equilibration, R_k is calculated as an average over the two boundaries.

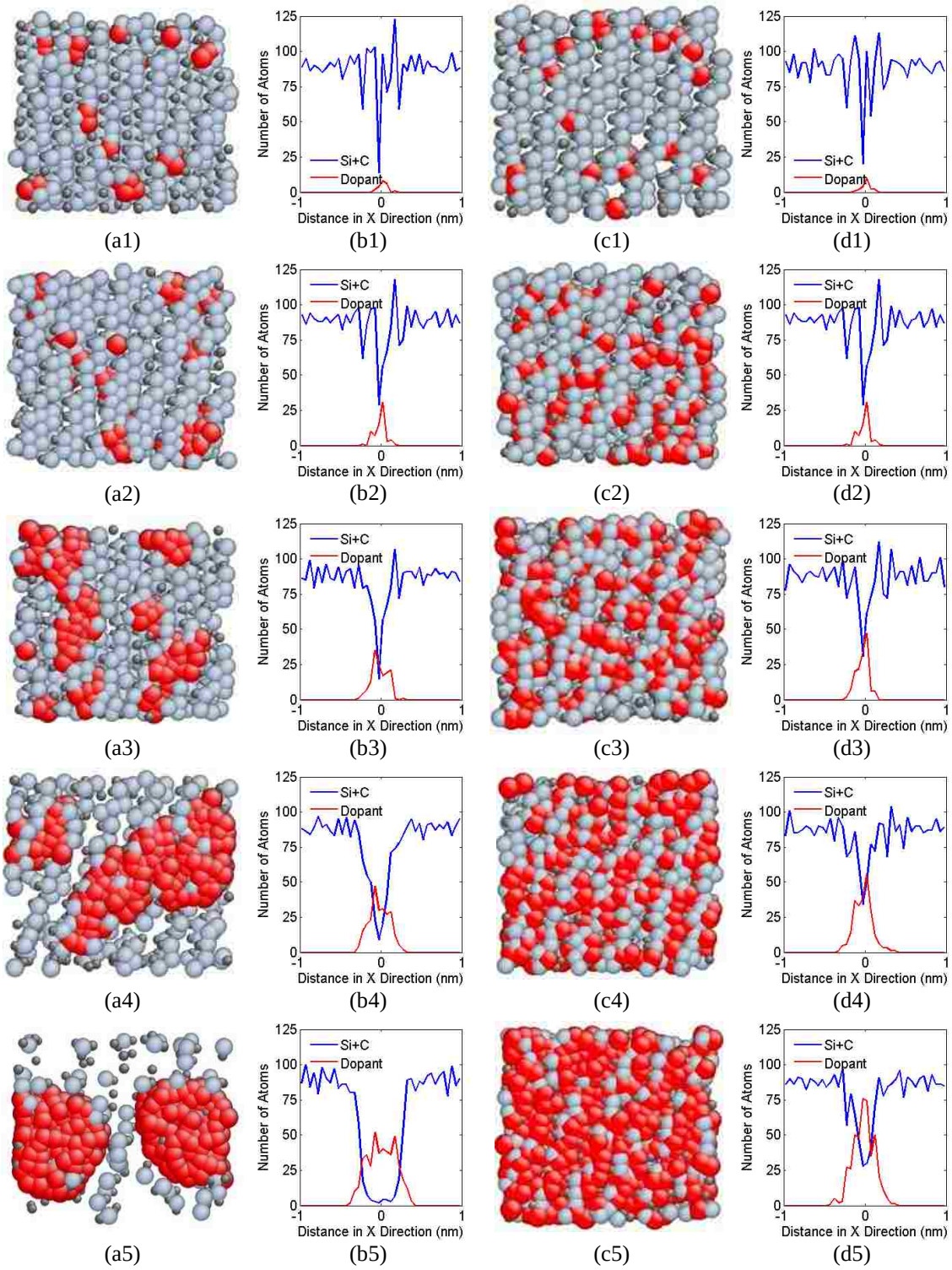

Figure 18: (a and c) Atomic arrangement at GB (at X = 0) and (b and d) density profiles across the GB. Data are shown for the weak (a and b) and strong dopant/matrix interaction limit (c and d). Data shown are for dopant concentrations 0.048, 0.167, 0.33, 0.567, and 1.007 ML (1-5). Large dark spheres are dopant atoms; Si and C atoms \whereas bright red atoms are dopants

From the density distribution data for the matrix material near the GB it can be observed that in the layered limit, the lowest density of the matrix material observed at the GB was ~35% of the bulk crystalline value whereas, for the clustered limit, the density of matrix material at the boundary goes nearly to zero. This is particularly true at the highest dopant concentrations shown. If a summation of matrix atoms and dopant atoms is considered, the number density at the GB in the layered limit increased, whereas it decreased in the clustered limit.

The dependence of R_k on C in the clustered and layered limits is shown in Figure 19. In both limits, R_k increased with the increase in C. The increase was substantially more pronounced in the clustered limit as the dopant concentration increase beyond a certain value $C > 0.4$ ML. In particular, it was noted that for $C = 1.007$ ML (the highest concentration explored), R_k was nearly 10 times greater than the value for the undoped GB system, indicated as a green triangle on the plot. By contrast, for the same large value of C, R_k in the layered limit is slightly more than 1.5 times that of the undoped GB system. This was true for both the GBs in each system even though the cluster shapes assumed by the dopants at each GB was different in the weak interaction limit for all the different dopant concentrations simulated. The density distribution obtained at either GBs was however similar for any given dopant concentration evaluated in both the limits. The error in presented values of R_k are of order the symbol size in all cases.

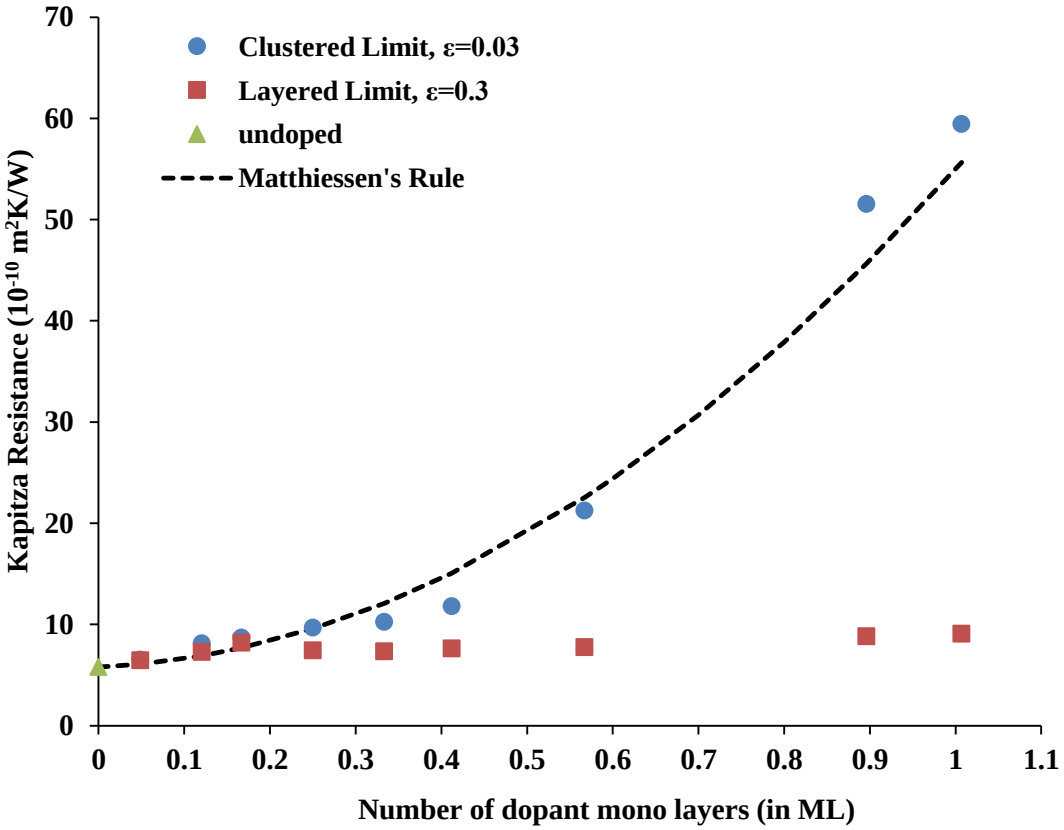

Figure 19: Kapitza resistance versus dopant concentration for the clustered (circles), the layered (squares) limits and the undoped system (triangle); a fit to the clustered data is also shown

To have a better understanding of the observed differences in R_k and their dependence on dopant concentration (and structure), 2D temperature contour plots were computed in the YZ plane for a 0.6 nm thick slab (in X) centered on the GB at X=0, as well as for slabs adjacent to and far from the GB. Figure 20a is a schematic of the simulation cell that also shows the slabs selected for computing planar temperature contours (though analysis bins were 0.6 nm thick in X, they are denoted as contour planes, or CPs). These plots were generated for C = 1.007 ML cases at both clustered and layered limits. To obtain these CPs, the slabs were divided into 15x15 bins in Y and Z and the temperature within each bin was computed using the equipartition theorem using velocities sampled every 100 time steps, with 100,000 samples used to calculate each bin temperature. In the layered

limit, the CPs (see Figure 20c) exhibit temperature uniformity within the plane, even for the CP centered on the GB. Given the simulation setup, the temperature at the GB CP should nominally be near 1000 K, and this was indeed observed in this limit. The ~50% increase in R_k observed for this system likely results from alterations in phonon modes due to doping. By contrast, in the clustered limit, while the temperature was relatively uniform in CPs away from (and even adjacent to) the GB, substantial temperature variations occurred for the CP centered on the GB (see Figure 20b). By comparing CP3 from Figure 20b to the image shown in Figure 18(a5), it was found that regions occupied by dopant clusters had temperatures near 1000 K while other regions showed significant variations in temperature. These variations result in significant lateral temperature gradients that result in reduced phonon transport across the GB. It is important to highlight that the analysis grid defined is such that some bins only sample small clusters of matrix atoms. Thus, the meaning of local temperature should be carefully considered. Though the number of atoms in certain bins was consistently small, significant temporal averaging was employed such that the largest error observed in computed T was less than 10 K. Moreover, spatial averaging is implicit in the interpolation used to generate Figure 20. To determine the impact of binning on our results, the presented analysis was repeated with coarser grids (10 x 10 and 8 x 8) and found that lateral T variations existed still existed within the matrix material in the plane of the GB.

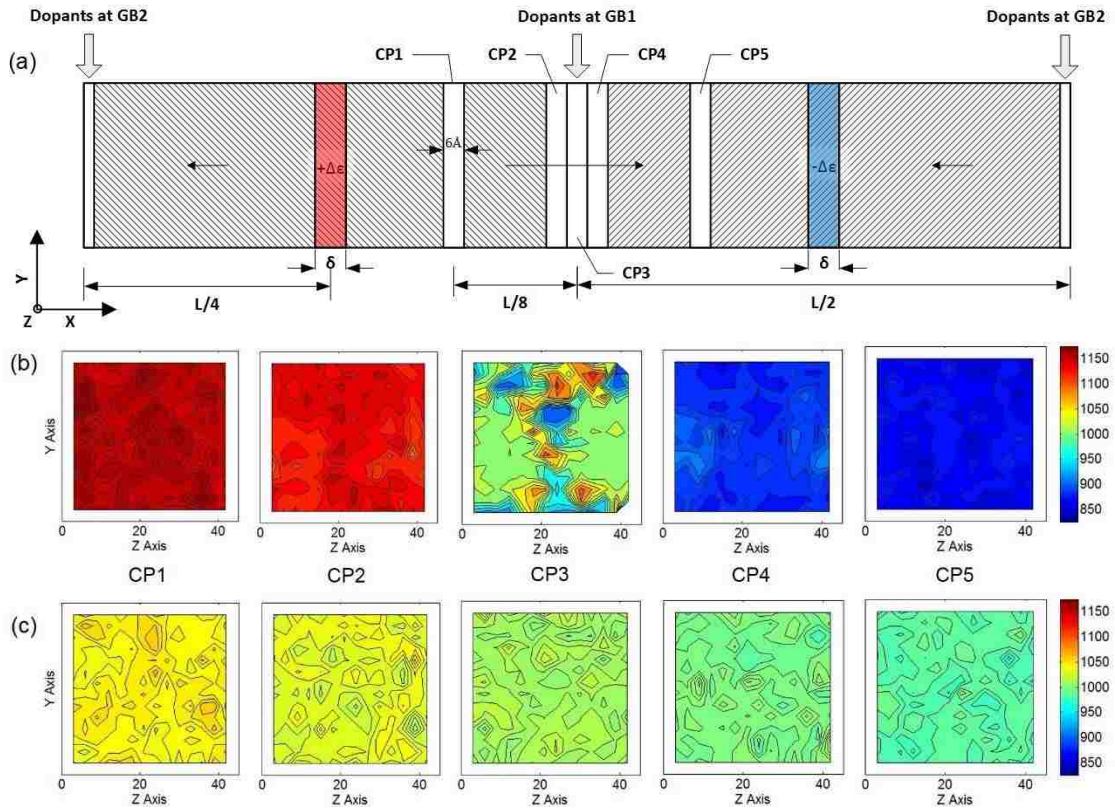

Figure 20: Temperature contours in different planes perpendicular to the direction of heat flux for a) clustered limit and b) layered limit for the contour planes (CPs) 1 through 5, from left to right. CP1 and CP5 are half way between the GB and the flux in and out planes, respectively, while CP2 and CP4 are adjacent to the GB and CP3 is on the GB.

One can understand the impact of these lateral gradients on the Kapitza resistance by examining a lattice dynamics expression for the Kapitza conductance given by

$$\sigma_k = \sum_{\lambda} \int_{v_x>0} \frac{d^3k}{(2\pi)^3} \hbar\omega\left(\lambda,\vec{k}\right) v_x\left(\lambda,\vec{k}\right) \frac{\partial\left\langle N_{\lambda\vec{k}}(T)\right\rangle}{\partial T} t\left(\lambda,\vec{k}\right) \tag{28}$$

where $\omega\left(\lambda,\vec{k}\right)$ are phonon frequencies for wavevector $\vec{k}$ and branch λ, $\left\langle N_{\lambda\vec{k}}(T)\right\rangle$ is the average phonon occupation number, $v_x\left(\lambda,\vec{k}\right)$ is the phonon group velocity normal to the grain boundary, and $t\left(\lambda,\vec{k}\right)$ is a transmission coefficient for phonons across the boundary. The integration is performed over the entire Brillouin zone[74, 107]. The presence of lateral

temperature gradients results in a net decrease in $t(l,k)$ and therefore, assuming that other factors in the integrand in equation (36) change less dramatically, a concomitant reduction (increase) in S_k (R_k). The effect of dopants on phonon density of states is explored in greater detail in Chapter 7

6.4. Structure Factor and Atomic Number Density

Diffraction measurement techniques have been extensively used to experimentally determine the planar arrangement of atoms in material. Each atom *j* in a crystal, for example, will diffract any incident radiation in a characteristic phase pattern depending on the coordinates of the atom (x_j, y_j, z_j) and atomic scattering amplitude 'f_j '. The sum of all the waves scattered by all the atoms in a given unit cell is called the Structure factor *S* [108],

$$S(hkl) = \sum_j f_j \exp\left[2\pi i\left(hx_j + ky_j + lz_j\right)\right] \tag{29}$$

where $\{hkl\}$ is the incident wave vector. From the above equation, a simple geometric rules can be applied to identify if for a given combination of the coordinates of the atom would reflect the incident wave or not. Consider the atomic coordinates (1, 1, 1). Substituting for (x_j, y_j, z_j) in the above equation, the exponential will depend only on the wave vector $\{hkl\}$. Now if $\{h+k+l\}$ are odd, the exponential will reduce to -1. However, if $\{h+k+l\}$ are even, the exponential will reduce to 1. The concept can be extended to SiC where *Zinc-Blende* crystal structure causes the above equation to depend independently on whether $\{hkl\}$ are all even or odd or mixed. Table 4 provides the geometrical rules as they apply to structure factor.

Table 4: Geometrical rules for Structure factor

Crystal Structure	Observed reflection	Structure factor, (S)
Primitive (1 atom per unit cell)	all *h, k, l*	f
Body centered cubic (2 atom per unit cell)	$h+k+l$ = even	2f
	$h+k+l$ = odd	0
Face centered cubic (2 atom per unit cell)	*h, k, l* all even	4f
	h, k, l all odd	4f
	h, k, l mixed	0

To highlight the role of boundary structure in determining R_k, we calculated the normalized structure factor, $S(\vec{k}_a)/N_s$, in a 3Å-thick layer adjacent to the GB having N_s atoms. The rotation of the crystal to form GBs causes to modify the wave vector to highlight ordering in a direction perpendicular to the GB normal. The Structure factor is normalized with respect to the scattering amplitude and is given as

$$S(\vec{k}_\alpha) = \frac{1}{N_s}\sum_{j=1}^{N_s}\sum_{i=1}^{N_s}\exp\left[i\vec{k}_\alpha\cdot(\vec{r}_i-\vec{r}_j)\right] \qquad (30)$$

where $\vec{k}_a$ is a wave vector allowed by the periodic boundary conditions. Figure 21 shows the Bragg peak heights for two face-centered cubic (fcc) reciprocal lattice vectors, $\vec{k}_1=(2\pi/a)$ (1,1,1) and $\vec{k}_2=(2\pi/a)$ (2,2,2), where *a* is the lattice parameter for the clustered and layered limits. It is evident from the figure that there is generally greater order in the layered limit of dopant segregation. In the clustered limit, the peak heights decrease significantly relative to those for the layered limit after $C>0.4$ ML, suggesting that

phonon scattering from boundary disorder may be an important factor in determining the GB resistance.

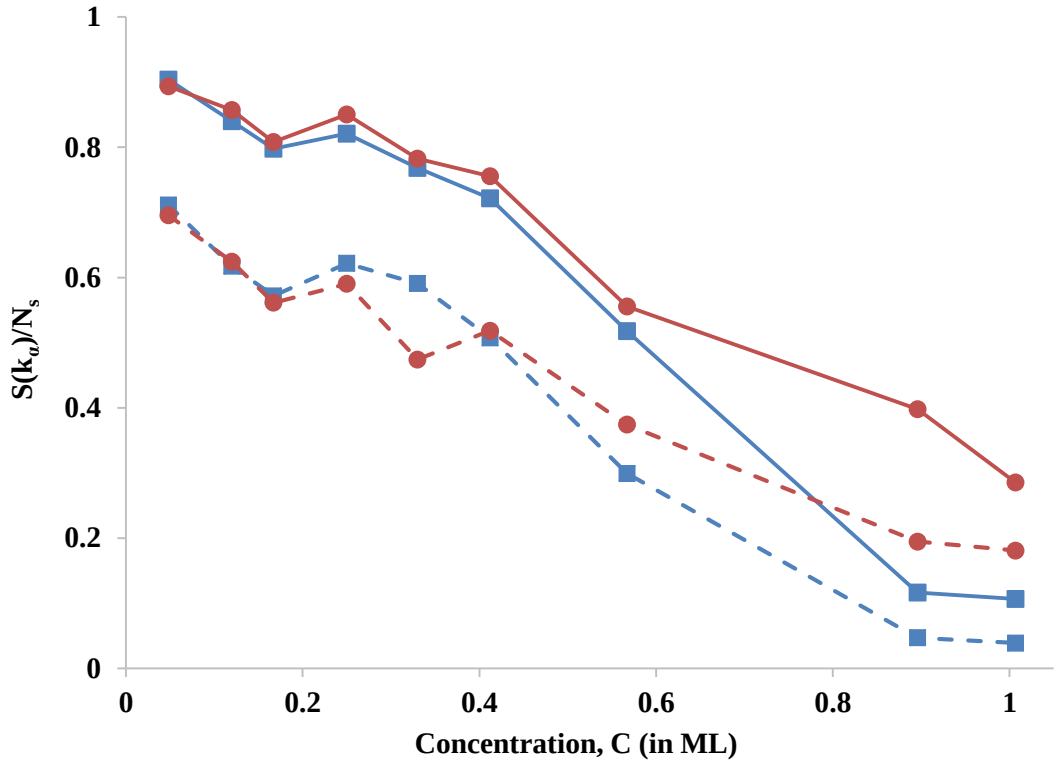

Figure 21: Bragg peak α = 1 (solid line) and α = 2 (dashed line) for the clustered (squares) and the layered (circles) limit

Further information about boundary chemistry in the vicinity of this critical concentration can be obtained from the normalized density calculation shown in Figure 22. The atomic density was calculated in a 6 Å-thick layer at the grain boundary, normalized with respect to the bulk atomic density in an identical layer in the undoped system. It is observed that for $C < 0.4$ ML the atomic density increases for both limiting cases while, for $C > 0.4$ ML, the density increases (decreases) for the layered (clustered) limit. This sharp decrease in density in the clustered limit for large C also reflects the high degree of disorder at the GBs.

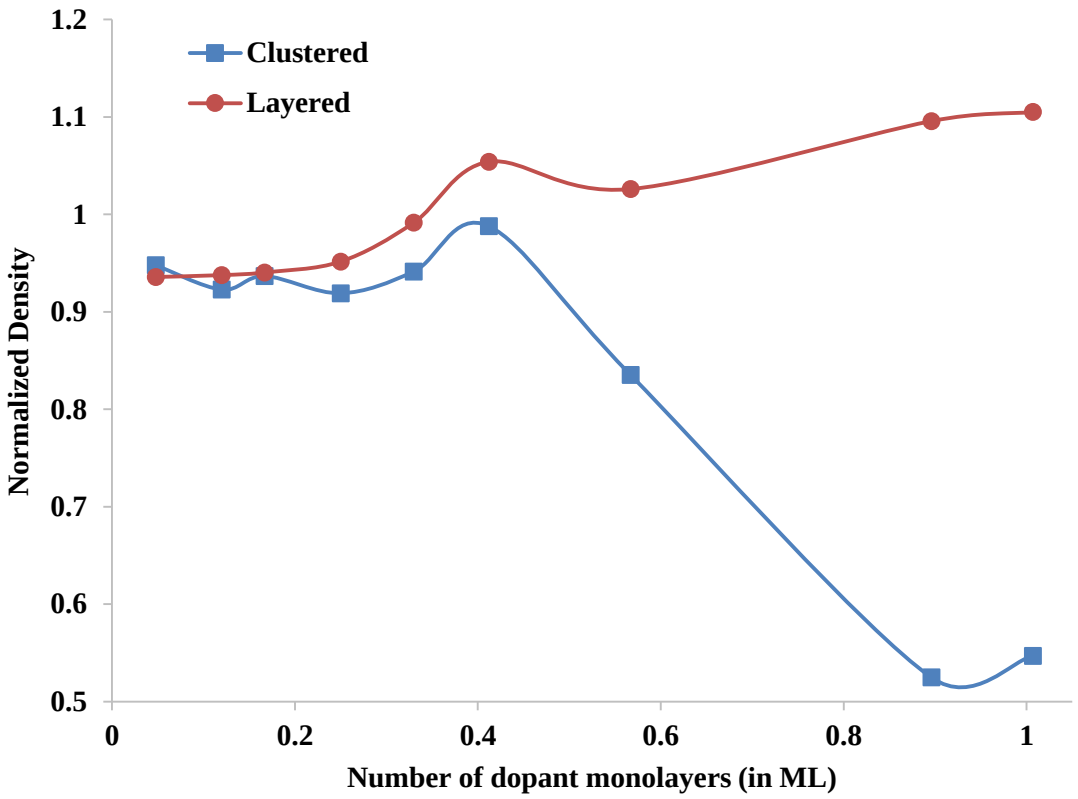

Figure 22: Normalized density in a 6Å thick layer at the GB for the clustered (squares) and the layered (circles) limit.

Having identified various factors that influence R_k, it is useful to assume that the contributions to R_k can be expressed, using Mathiessen's rule[109], as

$$R_k = R_k^{GB} + R_k^{C}(C) + R_k^{disorder}(C) \tag{31}$$

where contributions from different source of phonon scattering by grain boundaries, by impurities, and by boundary disorder are given by R_k^{GB}, R_k^{C}, and $R_k^{disorder}$ respectively, defined as a function of dopant concentration C. Equation (31) is expected to be a good approximation to the extent that phonon scattering from each source is independent. For the system considered here, the various contributions, estimated from the data in Figure 19 are found to be approximately (in units of 10^{-10} m^2K/W)

$$R_k^{GB}(C) = 5.79 \tag{32}$$

$$R_k^{C}(C) = 3.76C \tag{33}$$

$$R_k^{disorder}(C) = 45.45C^2 \tag{34}$$

where the last contribution applies only in the clustered limit. The corresponding fit to the clustered case data is shown in Figure 19 and satisfactory agreement is observed. The emergence of the disorder term for the clustered case is in accord with structural data in Figure 21

6.5. Summary

Non-equilibrium MD (NEMD) simulations were performed to compute the Kapitza resistance, R_k, for segregated grain boundaries in β-SiC; to quantify the impact of boundary dopant concentration, C, on R_k for different dopant/matrix interaction strengths. For the symmetric tilt grain boundary considered here, it was found that in the limit where the dopant/matrix interaction strength equals that of the dopant/dopant interaction, the segregation profile comprises dopant layers. In this limit, R_k was found to be relatively insensitive to C owing to the similar size of dopant and matrix atoms. By contrast, in the limit where the dopant/matrix interaction strength is less than that of the dopant/dopant interaction, the segregation profile exhibits clustering. In this limit, the dependence of R_k on C is more complex as clustering induces boundary disorder and, hence, increased phonon scattering. In particular, for $C > 0.4$, relatively large values for R_k are observed.

Another important observations about data presented was that the significant increases in R_k were accompanied by a reduction in density at the GBs; the formation of dopant clusters resulted in a more significant exclusion of matrix material from the GB

region for the clustered dopant case compared to the layered dopant case. Thus, modifications to thermal transport achieved via structural changes at GBs such as observed here for the clustered limit may result in reduction of mechanical properties. Further, no attempt was made here to control cluster size (via, e.g., modifications to the interatomic potential employed to describe dopant interactions). An interesting remaining question is whether significant increases in R_k occur predominantly due to reduction in the area fraction at GBs occupied by matrix material (and the corresponding cohesive area loss) or if there exists an additional non-trivial dependence on dopant cluster size.

Chapter 7

7. Effect of Temperature and Dopant Description

7.1. Introduction

Thermal transport in any material is attributed to the movement of electrons and/or lattice vibrations (phonons), when subject to a temperature gradient. In semiconductor materials like β-SiC, where very few free charge carriers are available, the contributions from phonons significantly dominates that from electrons[21]. Further, large wavelength phonons have been demonstrated to be the major contributor to thermal transport in the entire spectra at any temperature. Phonons with mean free path larger than the size of the grain get scattered at the grain boundary (GB), while σ remains relatively unchanged because of their much smaller mean free path compared to the phonons [19, 20].

Zhou *et al*. performed phonon density of states calculations to study the interface between metal and GaN semiconductor substrate by varying the mass of the metal and the bond stiffness between the metal and semiconductor material [31]. They observed that with the increase in mass of the metal, the density of states shifted towards the lower frequencies and therefore exhibited a better overlap with the vibrational spectra of GaN resulting in a decrease in R_k. They also observed that R_k decreased with the increase in cross-bond stiffness between the metal and the semiconductor, eventually levelling off beyond a certain limit. Duda *et al*. investigated the effect of cross-species interaction and its cut-off distance on the temperature dependence of R_k in a mass mismatch GB system. They determined that although R_k had linear dependence on temperature for all combinations of

the interaction strength and the cut-off distance, any reduction in cut-off distance or weakening of the cross-species interaction strength resulted in a decline on the temperature dependence of R_k[44]. The presence of impurities has also been investigated. Particularly, dopant mass, concentration, and the bond strength have been identified as important factors in determining R_k[45]. However, these effects were studied at very low temperatures.

Kapitza resistance, R_k, for any doped system is influenced by how strongly dopants at the GB interfere with the transmission of phonons through the GB. It is shown by the present study that the reduction in the phonon transmission was more significant in the cases where dopants segregated to the boundary. That is attributed to the stronger affinity towards neighboring dopant atoms compared to the matrix SiC atoms. The work presented in this chapter investigates how the dopants influence the phonon density distribution in the system. It is also investigated here that the influence of dopant mass and temperature of application on R_k.

7.2. Influence of Temperature

The sensitivity of thermal conductivity to temperature has long been known. Stevens *et al*. studied the temperature dependence of Kapitza conductance, σ_k using NEMD simulations and observed that σ_k increased linearly with the increase in temperature[63]. This observation can be explained from the Bose-Einstein distribution which determines the number of phonons at high temperature as:

$$\langle n \rangle = \frac{1}{\exp\left(\frac{\hbar\omega}{k_b T}\right) - 1} \approx \frac{k_b T}{\hbar\omega} - \frac{1}{2} \tag{35}$$

Here $\langle n \rangle$ is the expected number of phonons, ω is the frequency of the phonon and k_b and $\hbar$ are the Boltzman and Planck's constants respectively. From the above equation, it is noted that the number of phonons for a given mode increases with the increase in temperature. However, despite the low frequency phonons getting scattered at the GB, the increase in number of high frequency phonons results in an increased thermal transport across the GB. Young and Maris further demonstrated that with the increase in temperature, the rate of increase in σ_k decreased due to the increase in number of high frequency phonons which have a lower transmission coefficient and group velocity[110]. Dopant effects on R_k at higher temperatures were evaluated for both undoped and doped systems. Lattice constants were calculated for a wide range of temperatures from 300K and 1500 K, and bicrystals with 7.59° misorientation angle were created with the corresponding lattice constant at a given temperature. Least energy configuration were determined for each bicrystal, using Olmsted's methodology[86] as explained in Section3.3.2 above. Keeping the other simulation parameters constant, it was observed that R_k decreased with the increase in temperature. Figure 23 shows σ_k as calculated as a function of temperature for the undoped, lightly doped (C=0.048ML) and heavily doped (C=1.007ML) systems, and weak dopant matrix interaction strength ε_{dm} = 0.03 eV. It was observed that the σ_k increased linearly with the increase in temperature for all three cases. However, this enhancement was mitigated by boundary segregation, especially at high dopant levels. This observation proves particularly important for high temperature applications where majority of the materials indicate a high κ. Addition of dopants above a certain concentration can counteract the undesired high κ at high temperatures.

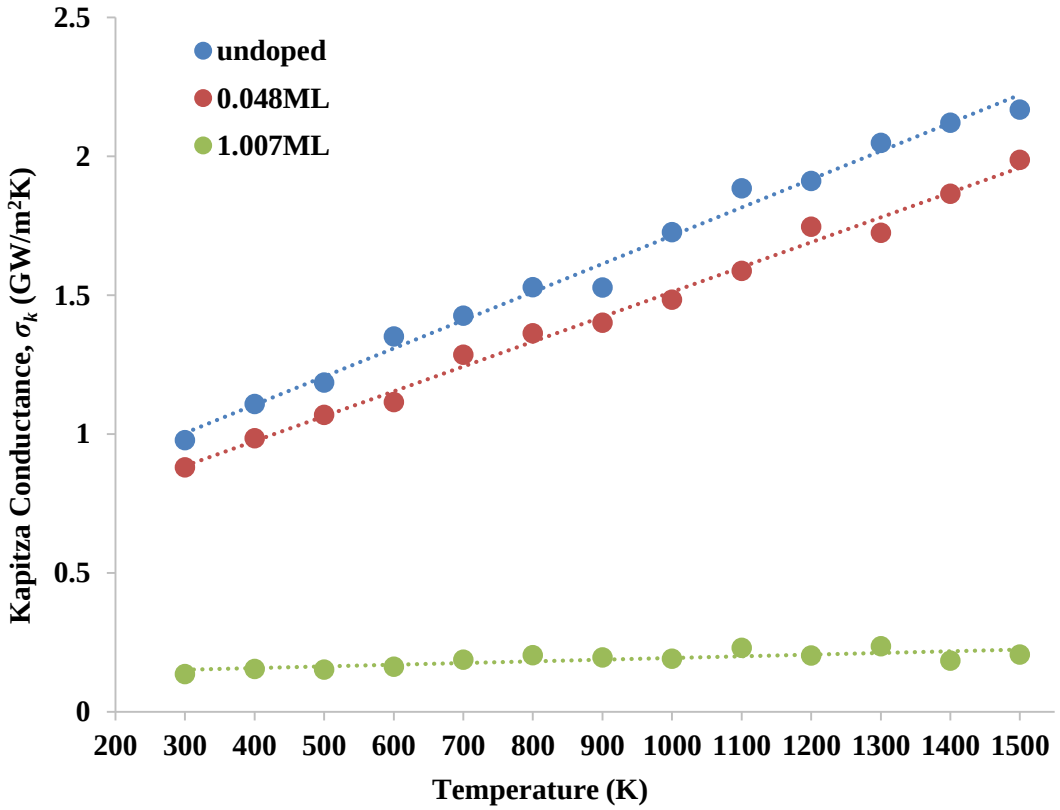

Figure 23: Effect of dopant concentration on temperature on σ_k for 7.59° symmetric tilt GB system in the cluster limit (ε_{dm} = 0.03)

7.3. Influence of Dopant Mass

Klemens theory states that the rate of phonon scattering, τ, due to the presence of dopants is inversely proportional to the square of the atomic mass difference between the dopant and the host material[111] $\tau^{-1} \propto \left(\left(m_{host} - m_{dopant}\right)/m_{host}\right)^2$. However, Duda *et al.* determined that the Klemens theory does not hold for GB systems where the scattering of phonons also depends on the overlapping phonon spectra between the two grains[45]. The frequency range of the vibrational spectra of the dopants is proportional to $\sqrt{K/m_{dopant}}$. Here K is the stiffness constant for the dopants and depends on the strength of interatomic

interactions between the dopant atoms ε_{dd}. For a given ε_{dd}, with the increase in mass of the dopants, the range of frequency of the phonon spectra would decrease. If the dopant phonon spectra overlaps the vibrational spectra for the matrix material, a region of graded vibrational states will be obtained at the interface leading to a decrease in R_k. The influence of dopant mass on R_k at 1000 K was evaluated for the clustered and the layered limits. Keeping the other system variables constant, R_k was calculated for five different dopant mass systems, 6, 12, 20, 28 and 56 a.m.u. It was observed that for each dopant mass, R_k was consistently higher for the clustered limit than the layered limit. It was also observed that for a given dopant mass, although R_k increased with the increase in the dopant mass for both the clustered and the layered limit, the increase was much more significant in the clustered limit than in the layered limit. Figure 24 shows the influence of mass of dopant atoms for the both the strong and weak interaction cases and dopant concentration of 1.007 ML. It is evident that in both the layered and the clustered limit cases, Klemens theory is not applicable due to the presence of dopants at GB. Moreover, besides the stiffness of dopant atoms, the affinity between the dopant and matrix atoms has a clear significant and compounded effect on the R_k at the GB.

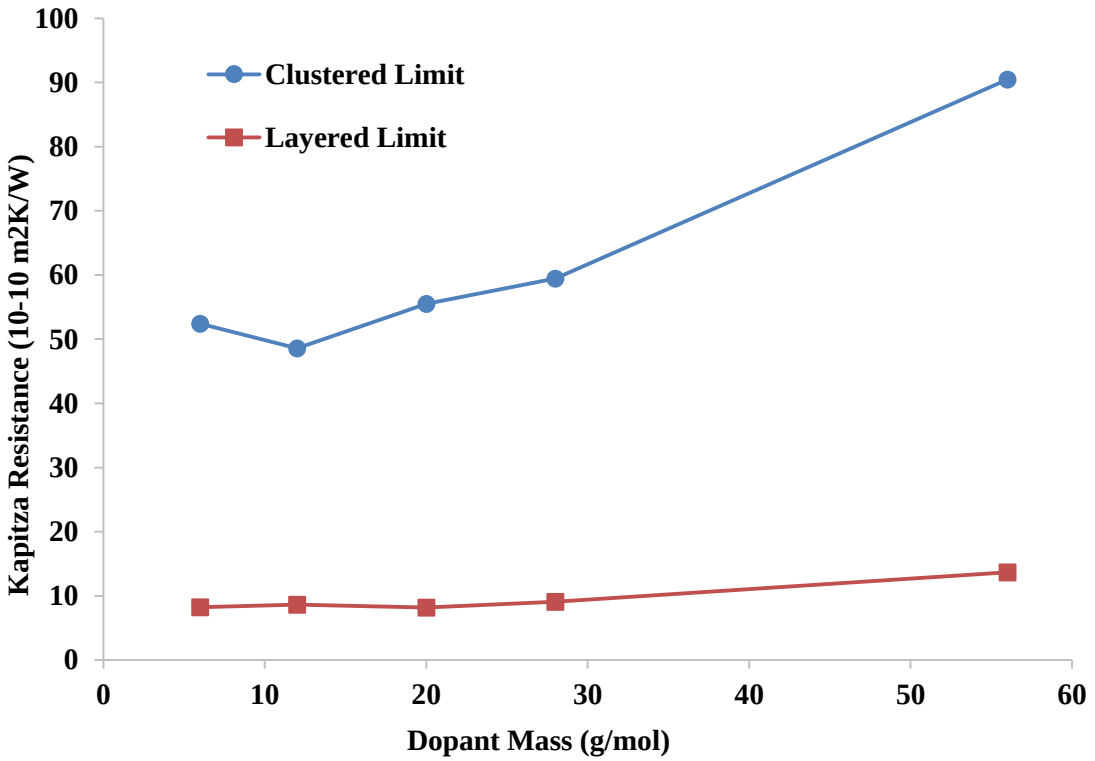

Figure 24: Influence of mass of dopant atoms on Kapitza resistance for in the layered (red squares) and clustered (blue circles) limit and dopant concentration of 1.007ML. Error bars are the size of the symbols for the data presented in this plot.

The normalized structure factor, $S(k_\alpha)/Ns$, was calculated in a 3 Å thick layer adjacent to the GB having *Ns* atoms using the same procedure as described in Section 6.4, to understand the behavior of heavier dopant atoms on R_k, where k_α is a wave vector allowed by the periodic boundary conditions. Figure 25 shows the Bragg peak heights for two face-centered cubic (fcc) reciprocal lattice vectors, $\vec{k}_1 = (2\pi/a)(1,1,1)$ and $\vec{k}_2 = (2\pi/a)(2,2,2)$, a is the lattice parameter. It is observed that the Bragg peak heights do not change significantly with the change in mass of the dopant atoms indicating that the change in dopant mass might not be a contributing to structural changes at the GB and that the effect of dopant mass only reflects in the spectra associated with the dopant phonons.

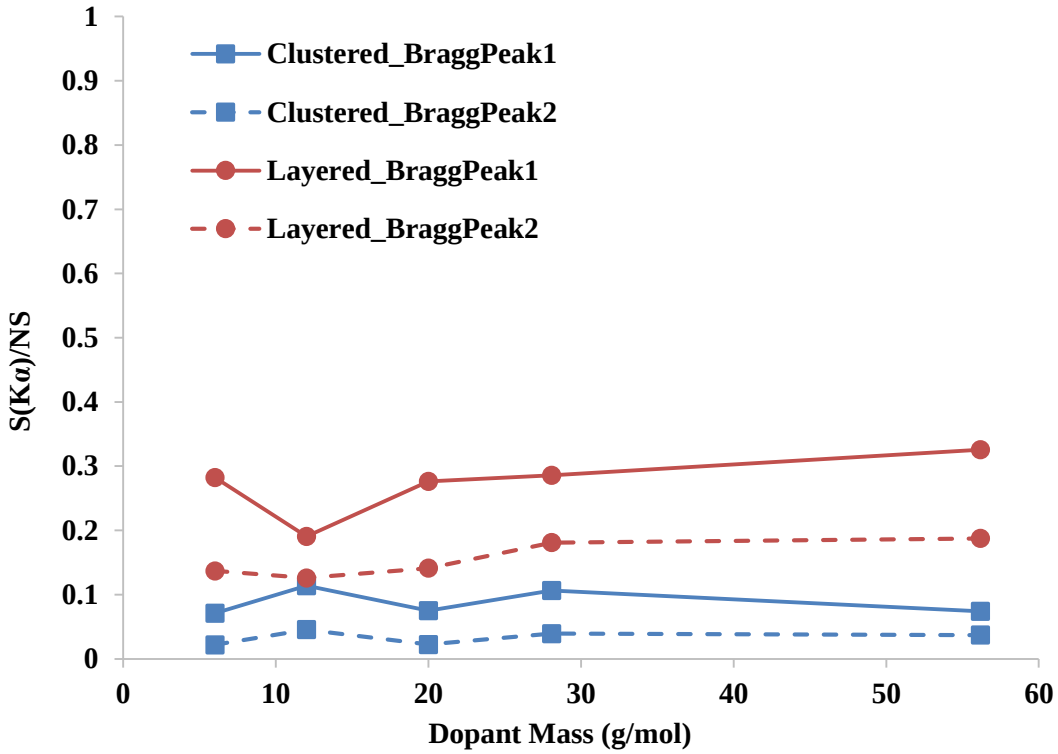

Figure 25: Bragg peak α=1 (solid line) and α=2 (dashed line) for the clustered (squares) and the layered (circles) limit

7.4. Influence of Dopant/Matrix Interaction Strength

The bond strength and atomic radius of LJ dopant atoms can be controlled by modifying the energy parameter epsilon and the length parameter sigma. A change in the interatomic interaction strength ε will change the interatomic force constant that determine the forces experienced by neighboring atoms. Duda *et al*. [45] noted that modifying the dopant/dopant interaction strength, ε_{dd}, did not have significant impact on R_k. However, their study was limited to very low temperatures and the dopant/matrix interaction strength were obtained using Lorentz-Berthelot mixing rules. In chapter 6, the impact of varying ε_{dm} was explored for a set of values nearly 10 times compared to ± 25% variation in ε_{dd} as

studied by Duda *et al.* It was observed that dopants that interact weakly with the matrix tend to cluster together due to higher affinity towards other dopant atoms, resulting in a surge in R_k. However, for the strong dopant/matrix interactions, dopants did not exhibit segregation at the GB. In this chapter, six additional dopant/matrix interaction strengths were examined to determine the critical interaction strength where dopants begin segregating to the GB. Keeping the ε_{dd} constant at 0.3 eV, the influence of dopant/matrix interaction strength, ε_{dm}, on R_k was examined. The length parameter was kept constant at σ = 2.0 Å. From Figure 26, it was noted that R_k decreased linearly with the increase in ε_{dm} till it reached ε_{dm} = 0.17 after which the rate of reduction in R_k decreased gradually.

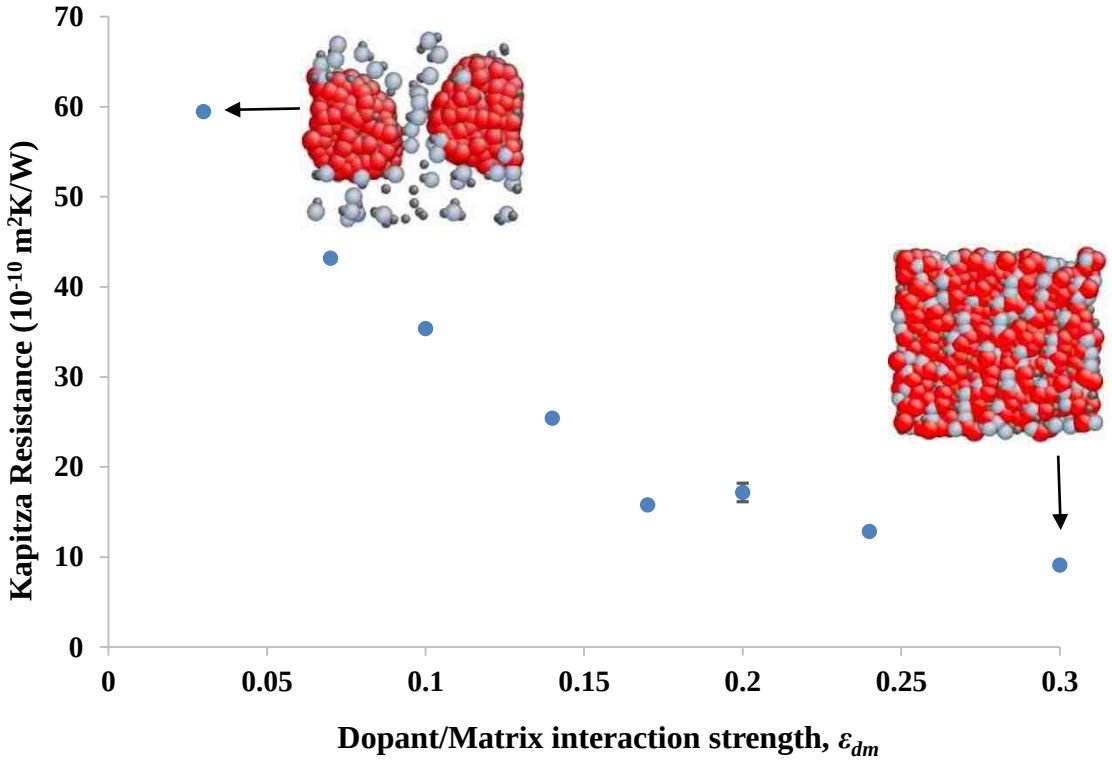

Figure 26: Kapitza resistance for different dopant/matrix interaction strengths and a dopant concentration of 1.007ML at 1000 K. The insets show the corresponding segregation profiles for the two limiting cases with Si atoms (blue), carbon atoms (black) and dopant atoms (red). Error bars were determined by averaging over well separated 50 data points.

Since the interaction between real dopants and matrix is a characteristic of the dopant material used, the approximately six-fold increase in R_k suggests that the boundary resistance may be tuned by a judicious choice of dopant.

7.5. Vibrational Density of States

Kapitza conductance, σ_k which is the inverse of Kapitza resistance R_k at temperature T is defined as the ratio of the heat flux across the interface per unit time to the temperature difference across the interface. Young and Maris expressed σ_k in terms of the group velocity of phonons of frequency ω, $\langle v_z(\omega)\rangle$ and the average transmission coefficient of the phonons, $\langle t(\omega)\rangle$ as[107, 110]:

$$\sigma_k(T) = \frac{1}{2}\int_0^\infty C(\omega,T)\langle v_z(\omega)\rangle\langle t(\omega)\rangle \tag{36}$$

$$C(\omega,T) = D(\omega)\hbar\omega\frac{\partial n(\omega,T)}{\partial T} \tag{37}$$

where $C(\omega,T)$ is the specific heat per unit volume of the phonons, $D(\omega)$ is the phonon density of states, alternately called vibrational density of states, and the $n(\omega,T)$ is the Bose-Einstein occupation number. From equations (36) & (37), it is evident that σ_k is directly proportional to the integral of the vibrational density of states. Vibrational density of states calculations were performed for the undoped, and heavily doped systems at both the clustered and the layered limits, to further explore the mechanisms responsible for the significant change in R_k for the different dopant interaction cases.

In order to draw good comparison, besides the GB, vibrational density of states calculations were performed for four additional planes (CP1, CP2, CP3, CP4, and CP5) strategically placed along the direction of heat current, as illustrated in Figure 27(a). Each

of these planes is 6 Å thick with CP1 (CP5) placed midway between the heat in (out) region and the GB, CP2 & CP4 placed adjacent to the GB on either sides, and CP3 at the GB. The vibrational density of states was calculated by taking the Fourier transform ($\mathscr{F}$) of the velocity autocorrelation function, ψ [53, 112]. Atomic velocities in each plane were obtained at each MD time step for 1,000,000 time steps and ψ was calculated for segments of 20,000 points with 90% overlap according to the Welch method of calculating power spectral density [113, 114]. For a multi-species system like doped β-SiC, it is vital to take into account the individual contribution of each species. Therefore, for each segment, the power spectral density of each species α was calculated by averaging ψ for that species and then taking the Fourier transform of it [112]. The normalized ψ_α for the species α (α = Si, C, & Dopant) is given as:

$$\psi_\alpha(t) = \frac{1}{N_\alpha}\sum_{i=1}^{N_\alpha}\frac{\langle \vec{v}_i(t)\cdot\vec{v}_i(0)\rangle}{\langle \vec{v}_i(0)\cdot\vec{v}_i(0)\rangle} \tag{38}$$

where $\vec{v}_i(t)$ is the velocity of the atom *i* of the species *z* and $\langle\cdots\rangle$ is the long time average of the data from MD simulation as described above. The power spectral density can then be calculated from the weighted Fourier transform using the mole fraction, c_α, of the species α in the plane

$$D(\omega) = \sum_\alpha c_\alpha D_\alpha(\omega) \tag{39}$$

$$D_\alpha(\omega) = \int_{-\infty}^{\infty}\psi_\alpha(t)e^{i\omega t}dt \tag{40}$$

Of the 20,000 data point in velocity autocorrelation function, Fast Fourier transform was performed over the first 16,384 points, and the remaining data points were discarded. vibrational density of states is proportional to the power spectral density[45], and was

calculated by scaling the individual contribution of each species by their mole fraction[115]. The vibrational density of states for undoped, clustered limit, and the layered limit systems respectively are illustrated in Figure 27(b), (c), and (d) respectively. For the undoped system, phonons with mean free paths greater than the distance between the heat reservoir and the GB were scattered, causing a sharp drop in vibrational density of states at the GB (CP3). Moving away from the GB, In CP2 and CP4, vibrational density of states started recovering and eventually assumed the same outline as that in the pseudo bulk β-SiC in CP1 and CP5 for the simulation system. Focusing at the GB, it can be seen that in the frequency range 180 THz – 200 THz, the peak for vibrational density of states were no longer distinct for clustered limit case whereas in the layered limit some vibrational density of states can be seen in the same frequency range shown in Figure 27(c) & (d) respectively.

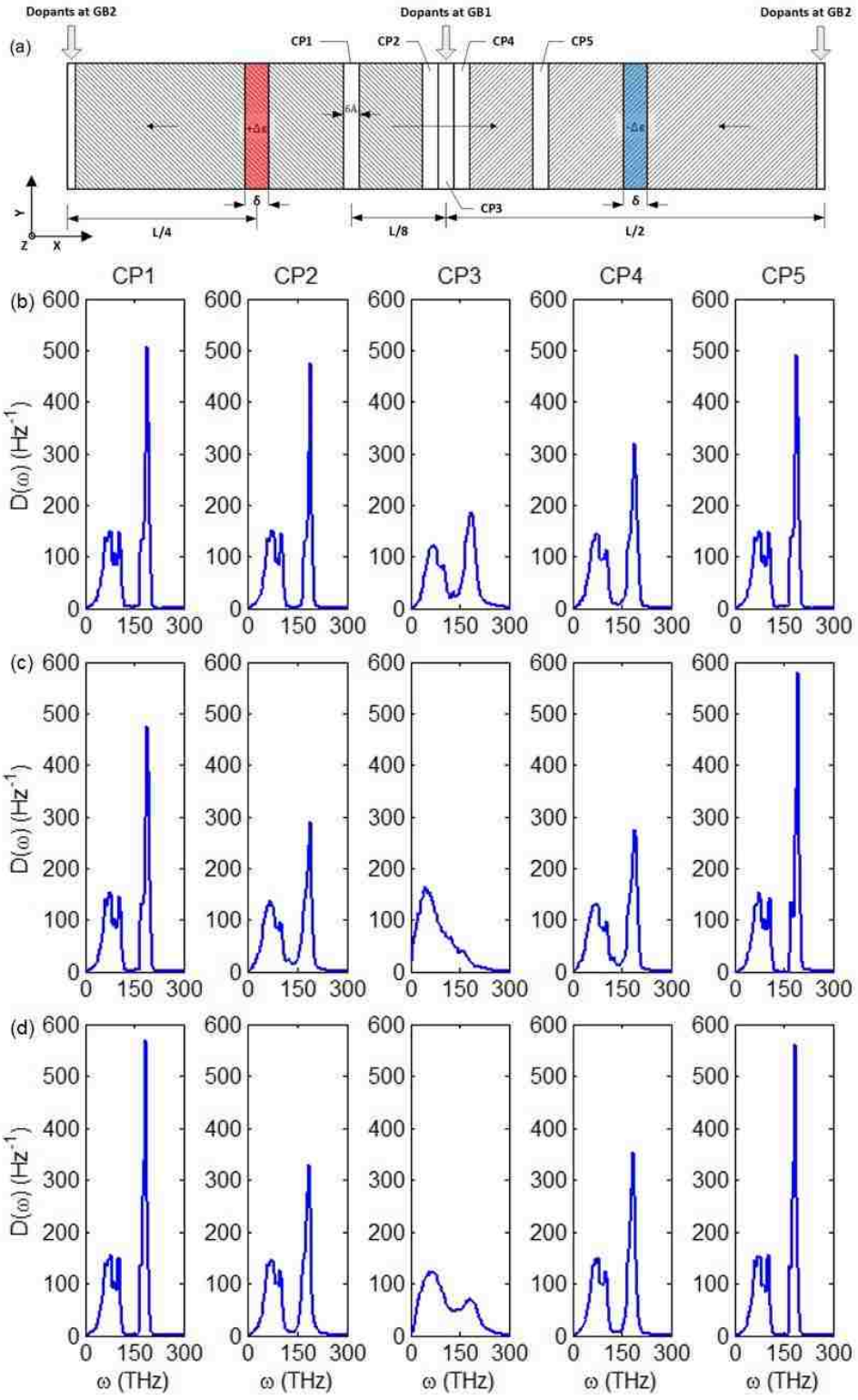

Figure 27: a) Sketch showing the location of 5 different planes for which vibrational density of states is calculated perpendicular to the direction of heat flux for b) undoped system, c) clustered limit, and d) layered limit.

A closer investigation of the individual contribution from the different species at the GB indicated that each species had a different contribution over any given frequency range. Figure 28a) show the individual contribution from each species as in ideal β-SiC crystal of same cross-sectional area as the undoped system at equilibrium. It is observed that the contribution to vibrational density of states from carbon and silicon atoms was highest for 180 THz < ω < 200 THz, as shown in Figure 28a). However, the presence of grain boundary results in loss of these peaks as can be seen from vibrational density of states contributions from the constituent species at the GB in an undoped system as shown in Figure 28b).

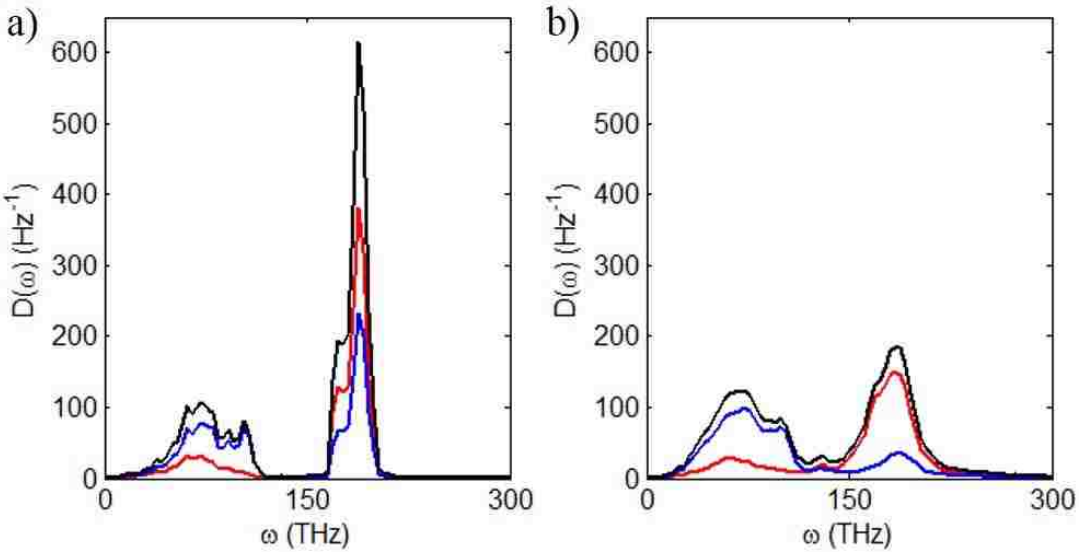

Figure 28: Individual contribution of the constituent species Si (blue), C (red) to vibrational density of states in a) as well as the total vibrational density of states (black) for a monocrystal at equilibrium. and b) at the GB in an undoped system at steady state

This observation becomes particularly important for doped systems. Figure 29a) and Figure 29b) show the vibrational density of states plots for the clustered and layered limit cases respectively, for different dopant concentrations. From left to right, the dopant concentration increases from 0.048 ML to 1.007 ML as indicated above the respective

plots. For the clustered limit, it was observed that with the increase in dopant concentration, the contribution from carbon to the total vibrational density of states decreased in the frequency range 180 THz – 200 THz, resulting in a decrease in the total vibrational density of states for the mentioned frequency range. At the same time, given the dopant atoms have the same mass as that of Silicon atoms, the vibrational density of states in the frequency range 60 THz – 90 THz increases even though the contribution from Silicon decreases in that frequency range. For the layered limit, Figure 29b) shows that the drop in vibrational density of states contribution from carbon and silicon were lower compared to those at the clustered limit for any given concentration.

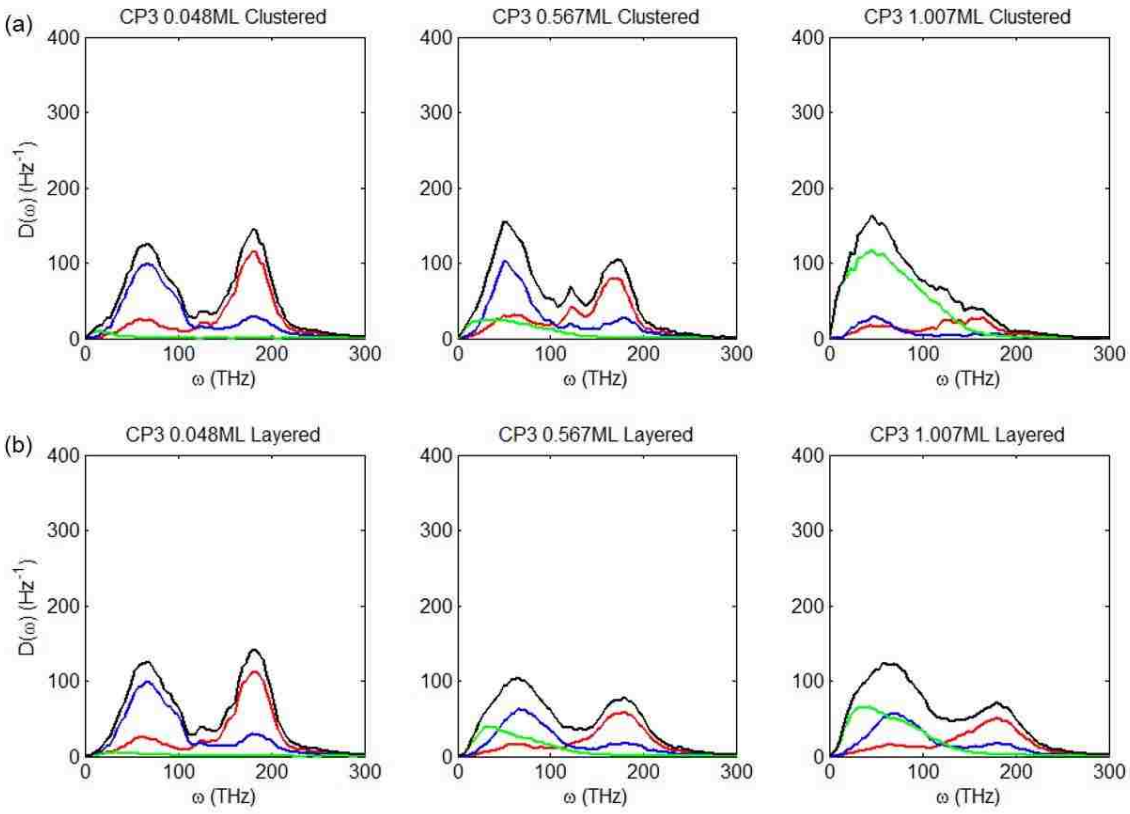

Figure 29: Individual contribution of the constituent species Si (blue), C (red) and dopant (green) to vibrational density of states in as well as the total vibrational density of states (black) for a) clustered limit (ε_{dm} = 0.03) and b) layered limit (ε_{dm} = 0.3) for the dopant concentrations (left to right) 0.048 ML, 0.567 ML and 1.007 ML.

Speed of sound calculations were performed for the monocrystal at equilibrium to determine the wave mode contributing the peak in density of states in the frequency range of 180 THz – 200THz. The bulk modulus for β-SiC was determined from the elastic constant at 0 K, as calculated by Tersoff [61] for the interatomic potential used in this work. The wave mode, λ = 2.714 Å was obtained for angular frequency of 190 THz. Given that the second neighbor C-C and Si-Si separation distance at 1000 K is 3.04 Å, and the wave mode obtained above is based on the elastic constants at 0 K, it can be argued that the wave mode corresponds to the phononic transmission between C-C and Si-Si atoms.

Projected vibrational density of states calculations were performed to obtain additional information about the important vibrational modes that affect heat transport. These calculations were performed for an ideal crystal using the methodology described by Meyer *et al*. [116]. Plane waves with wave vector *q* parallel to (100), (110) and (111) family of vectors were identified and the projection of the velocities on the plane waves were calculated from:

$$v_{\vec{q}}^{\vec{p}}(t) = \sum_{i=1}^{N} \vec{p} \cdot \vec{v}_i(t) e^{-i\vec{q}\cdot\vec{r}_i^{\,0}} \tag{41}$$

here $\vec{r}_i$ is the average position of the i^{th} atom and $\vec{p}$ is the polarization vector. Projected vibrational density of states were then calculated from the Fourier transform ($\mathcal{F}$) of the projected velocity autocorrelation function $g_{\vec{q}}^{\vec{p}}(\omega)$ as follows:

$$g_{\vec{q}}^{\vec{p}}(\omega) = \int_{-\infty}^{\infty} dt \frac{\left\langle v_{\vec{q}}^{\vec{p}}(t) \middle| v_{\vec{q}}^{\vec{p}}(0) \right\rangle}{\left\langle v_{\vec{q}}^{\vec{p}}(0) \middle| v_{\vec{q}}^{\vec{p}}(0) \right\rangle} e^{i\omega t} \tag{42}$$

Sharp peaks were obtained at frequencies corresponding to the phonons with wave vectors $\vec{q}$ and polarization $\vec{p}$. From an analysis of several high-symmetry directions, peaks were observed at ω = 200 THz from the projected vibrational density of states for $\vec{q} \| \langle 110 \rangle$ family of vectors as shown in Figure 30. As is evident from the figure, modes with a polarization $\vec{p} \langle 111 \rangle$ make a significant contribution to this peak. Given the zincblende structure of β-SiC, it can be seen that this direction is associated with the Si-C bond.

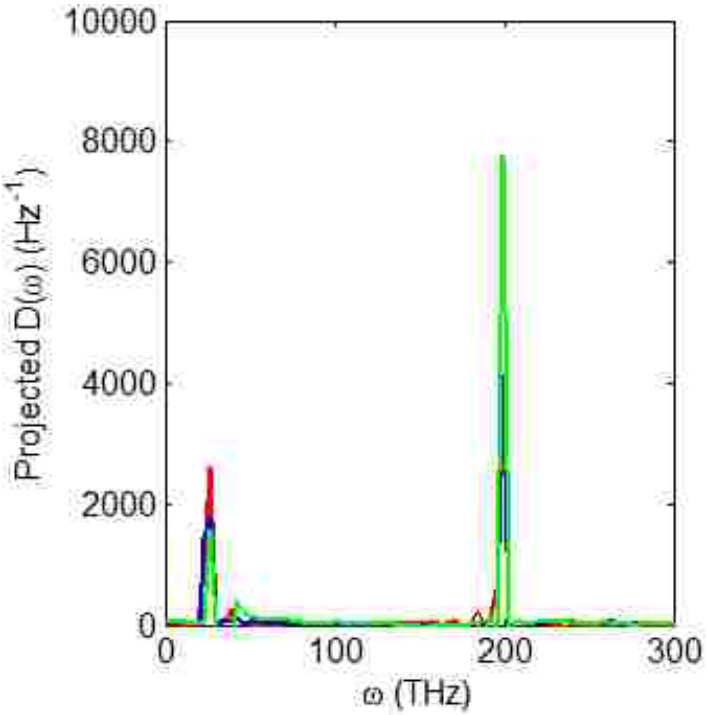

Figure 30: Projected vibrational density of states for an ideal crystal at 1000 K averaged over wave vectors $\vec{q}$ = [1 1 0], [1 0 1] and [0 1 1], and polarization vectors $\vec{p}$ = [1 0 0] (red), [1 1 0] (blue) and [1 1 1] (green).

A more detailed analysis of the relevant vibrational modes was obtained by an eigenmode analysis of the force-constant (i.e., Hessian) matrix for an undoped, perfect crystal of size 3×2×2 unit cells[57, 117, 118]. Small perturbations were introduced in all three dimensions for each atom and the Hessian matrix was built from the resulting forces

on all other atoms for each perturbation. For an N atom system, the Hessian matrix (Φ_τ) is a 3N × 3N matrix given by:

$$\Phi_{\tau,\tau'} = \frac{\partial^2 E}{\partial u_\tau \partial u_{\tau'}} = -\frac{\partial F_\tau}{\partial u_{\tau'}} = \frac{\partial F_{\tau'}}{\partial u_\tau} \tag{43}$$

where τ refers to the perturbation along the α^{th} cartesian coordinate component of the i^{th} atom. The eigenvalues obtained from diagonalizing the Hessian matrix, are the relevant phonon modes for the system in accordance with the equation:

$$\sum_{\tau'} \frac{\Phi_{\tau,\tau'}}{\sqrt{m_\tau m_{\tau'}}} e_{\tau'}^{\lambda} = \omega_\lambda^2 e_\tau^\lambda \tag{44}$$

It was determined that for the frequency range of 180 THz – 200 THz, majority of the phonon waves are travelling along the through the vibrational interaction between the second neighbor C-C and Si-Si atoms. From this analysis, the modes 180 THz $<\omega<$200 THz were found to be optical modes in which the Si and C atoms vibrate in opposite directions; by contrast, the low-frequency peak comprises acoustic modes in which the Si and C atoms vibrate in the same direction. One optical eigenmode for which $\omega = 204$ THz is illustrated in Figure 31.

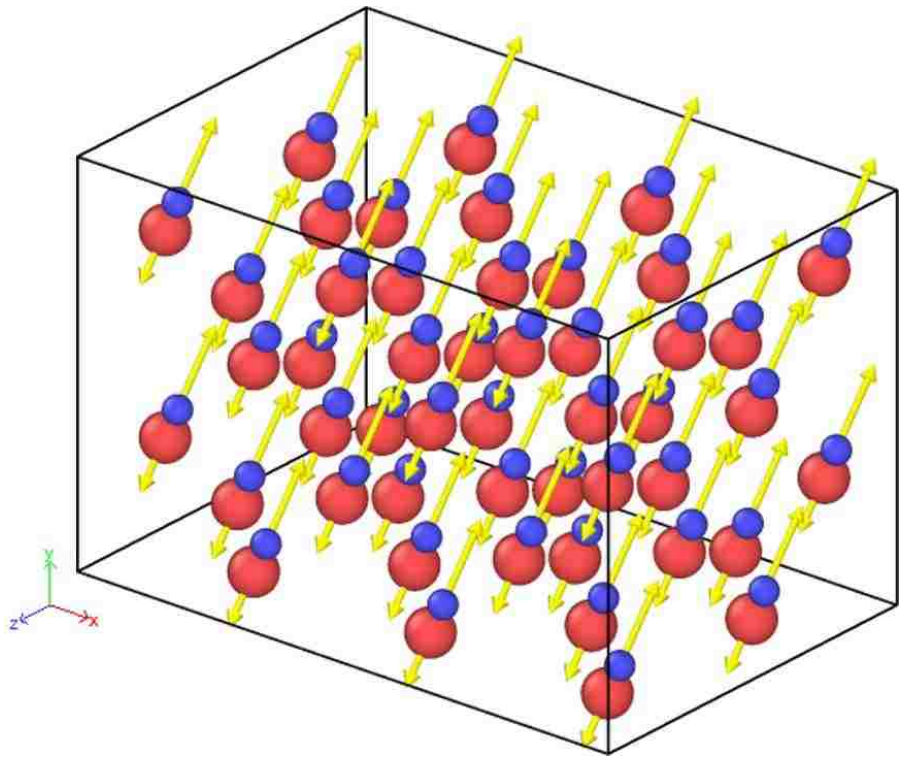

Figure 31: Atomic vibrations for Silicon (red) and Carbon (blue) from eigenmode analysis at $\omega = 204$ THz

Given that $\omega = 204$ THz corresponds to the frequency most significantly affected by dopant segregation as alluded to in the discussion above, it is clear that dopant segregation reduces the number of optical modes in the system, most especially in the clustered limit. Details about the normal mode analysis performed as well as atomic vibration modes are provided in Appendix B.

7.6. Summary

In summary, various doping scenarios were investigated to assess the role of dopants on the degree of disorder and segregation at a grain boundary. System parameters, such as temperature and dopant/matrix interaction strength, were varied and the resulting effect on R_k was examined. It was determined that the dopant/matrix interaction strength

affected the GB structure, thereby causing different degrees of phonon scattering, and therefore both the dopants and boundary disorder were associated with an increase in R_k. Moreover, it was found that while the boundary conductance increased with increasing temperature, this enhancement was mitigated by boundary segregation, especially at high dopant levels. Finally, from an analysis of the local vibrational density of states and a complementary eigenmode analysis, it was found that doping decreased the number of optical modes, and therefore the conversion from optical to acoustic modes is an important mechanism in dictating boundary resistance.

Chapter 8

8. Effect of Grain Boundary Orientation & Energy

8.1. Introduction

Crystallographic orientation has been determined to significantly affect the thermal properties of the material. Several naturally existing crystals have been identified to exhibit different thermal conductivity along different directions. For example, Pyrolytic graphite exhibits a thermal conductivity of 2000 W/mK in-plane along the a-axis and the b-axis directions, however, the cross-plane thermal conductivity along the c-axis direction is only 6.8 W/mK [119]. This is primarily due to the weak van der Waals forces between the atomic layers in the c-axis direction. More recently, Zhao *et al.* observed that the naturally occurring Tin-Selenide (SnSe) crystals have a much higher thermal conductivity along the a-axis direction of orthorhombic structure at room temperature, compared to the thermal conductivity along the b-axis and c-axis directions [120]. Similarly, chalcogen materials like $Yb_{14}MnSb_{11}$ [121], Ag_6TlTe_5 [122], and $AgSbTe_2$ [123] are some of the state of the art materials that exhibit intrinsically low thermal conductivity. However, the special properties of these materials is only limited to crystalline form of the material. A non-crystalline material consists of grains that are very irregular and arranged in an extremely complex three dimensional structure.

From the discussions earlier in this report, it is evident that each grain will have a characteristic thermal conductivity. However, each boundary between the adjacent grains will have a distinct R_k because of the size of the grains comprising the boundary, as well

as the orientation that the grains subtend to each other. Experimental evidence has been advanced that indicates σ_k can vary significantly with the change in GB orientation due to the different phonon group velocities in different directions. Hopkins *et al.* observed that σ_k differed by as much as 40% between Al:Al_2O_3 (0001) and (11$\bar{2}$0) interfaces [124], but, no orientational dependence was observed Al:Si (001) and (111) interfaces. Similarly, Contescu et al. used time domain thermos-reflectance technique to measure σ_k in TiN:MgO interfaces and reported no crystallographic orientation dependence between (001) and (111) interfaces [125]. Crocombette *et al*. [34] studied R_k in low angle as well as large angle symmetrical tilt GB systems using MD simulations. The low angle GBs were created by inserting edge dislocations whereas the large angle GB systems were created by applying mirror symmetry and shifting the system to low energy configuration. For the low angle GB systems, they observed large variations in the thermal interface resistance R_k, increasing monotonously by nearly 5 times as the GB tilt angle increased from 2° to 8°. However, for the large angle systems, the change is R_k was no longer monotonous and appeared to be independent of the GB tilt angle. In a different study, Duda *et al*. [126] determined that the GB resistance depended on the atomic packing of the constituent grains. While bicrystals with fcc crystal structure did not show strong dependence of R_k on the crystal orientation, R_k at GBs between a fcc crystal and a tertragonal crystal were strongly influenced by relative orientation of the two crystals comprising the GB.

The work presented in this chapter investigates the influence of symmetric tilt angle forming the GBs on R_k. Of particular interest is the influence of temperature on the R_k for each of these GBs. Subsequently, dopants are inserted at the GB to determine their

influence on R_k for three different tilt angle GBs. Lastly, from the discussion in Section 3.3.2, it is reasonable to assume that there is always a distinct possibility that not all GBs will be at the lowest energy, perhaps resulting in slightly elevated stresses. It is therefore of interest to build an understanding of the influence of GB energy on R_k is explored.

8.2. Grain Boundary Misorientation Angle

Five different tilt angle GBs were created using the methodology described in Section 3.3 with the Z axis along the [1 1 1] direction. The misorientation angles were chosen such that the GBs ranged from coherent and ordered boundaries at low angles to more vicinal and general boundaries at large angles. Figure 32 shows the free surface plots for mono crystals with 3.9632°, 7.5891°, and 16.1021° misorientation angles along with

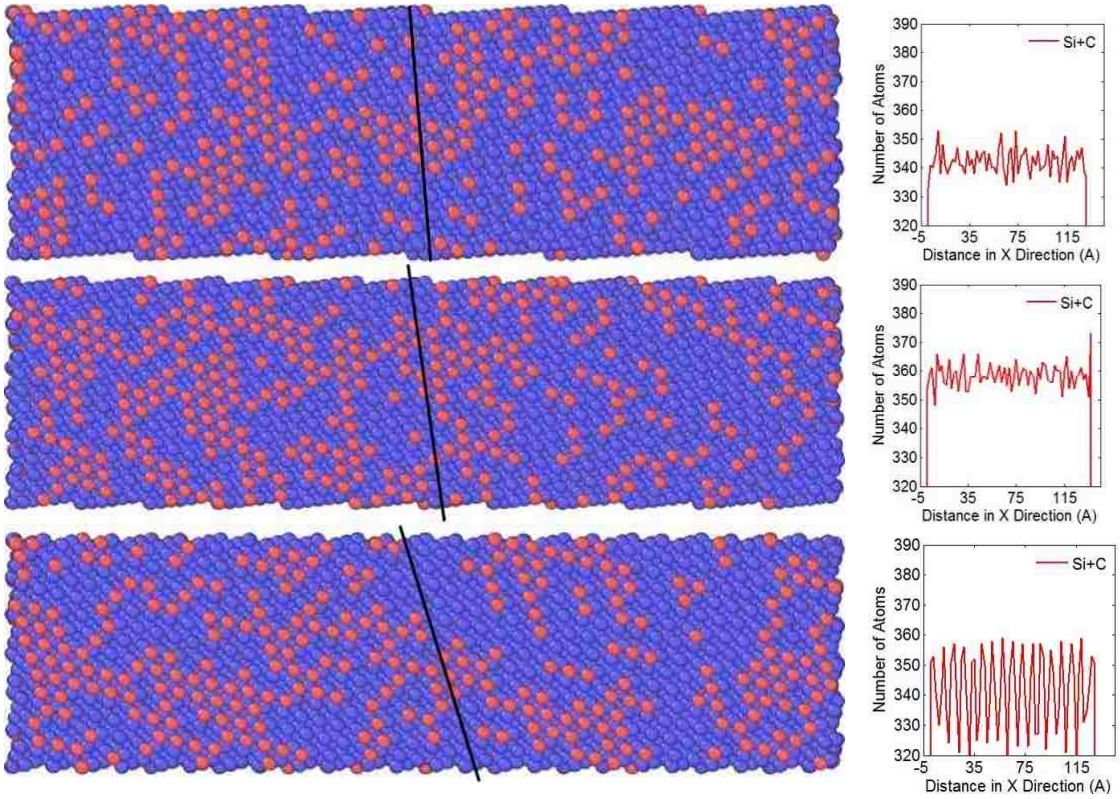

Figure 32: Free surface plots (left) and density distribution along the length (right) for 3.9632° (top), 7.5891° (middle), and 16.1021° (bottom) tilt angle about (1 1 1) plane in β-SiC mono crystal. Blue spheres are Silicon atoms and red spheres are Carbon atoms.

the atomic density distribution along the length of the mono crystal (horizontal direction in the page). The GB is formed by mirroring the mono crystal at the end. It is evident from the atomic structure adjacent to the edge that the GBs formed from these inclinations will differ with respect to the atomic proximity and occupation at the GB. From the density distribution plots on the right, it is observed that between 3.9632° and 7.5891° misorientation systems, it can be seen that the 7.5891° system is more densely packed, whereas the 16.1021° system has characteristic sharp planes of atoms which could potentially have an impact on local vibrational density of states. Table 5 provides the vectors along the X and Y axis for each symmetric tilt angle, and the dimensional details of these systems at 1000 K temperature.

Table 5: System dimensions and X and Y rotation vectors for different symmetric tilt angle GBs. Z Vector along [1 1 1]

Tilt Angle (θ)	L_x (Å)	L_y (Å)	L_z (Å)	X Vector	Y Vector
1.8038	268.988	77.6504	44.7281	$[\bar{2}\bar{7}\ \ \bar{2}\bar{4}\ \ 51]$	$[25\ \ \bar{2}\bar{6}\ \ 1]$
3.9632	264.194	38.1332	44.7281	$[\bar{1}\bar{4}\ \ \bar{1}\bar{1}\ \ 25]$	$[12\ \ \bar{1}\bar{3}\ \ 1]$
7.5891	276.528	39.9133	44.7281	$[\bar{8}\ \ \bar{5}\ \ 13]$	$[6\ \ \bar{7}\ \ 1]$
12.2163	258.882	49.8219	44.7281	$[\bar{1}\bar{1}\ \ \bar{5}\ \ 16]$	$[7\ \ \bar{9}\ \ 2]$
16.1021	263.352	38.0115	44.7281	$[\bar{9}\ \ \bar{3}\ \ 12]$	$[5\ \ \bar{7}\ \ 2]$

The fcc structure of β-SiC in (1 1 1) has a hexagonal ring shape. This shape reduces the interval of possible misorientation angles in the plane to [0°, 30°] for each mono crystal due to symmetry consideration and the GB should disappear when the tilt angle is 0°.

Figure 33 shows R_k as determined for each of the five different GB systems at different temperatures. Contrary to the notion that R_k should increase rapidly with an increase in the tilt angle as the grains become increasingly incoherent, R_k is observed to be relatively independent of the tilt angle. One reason for this observation lies in the methodology used to create these GB systems. The bicrystal was created by mirroring a mono crystal. However, if the system were to be created by replicating the mono crystal and then reversing the direction of rotation in the replicated second mono crystal, things might have been slightly different. Furthermore, with the current methodology of creating a bicrystal, the atoms appearing on the other side of the GB will not be in the ideal lattice positions even if the system rotation angle was reduced to zero. Additionally, since the atoms were

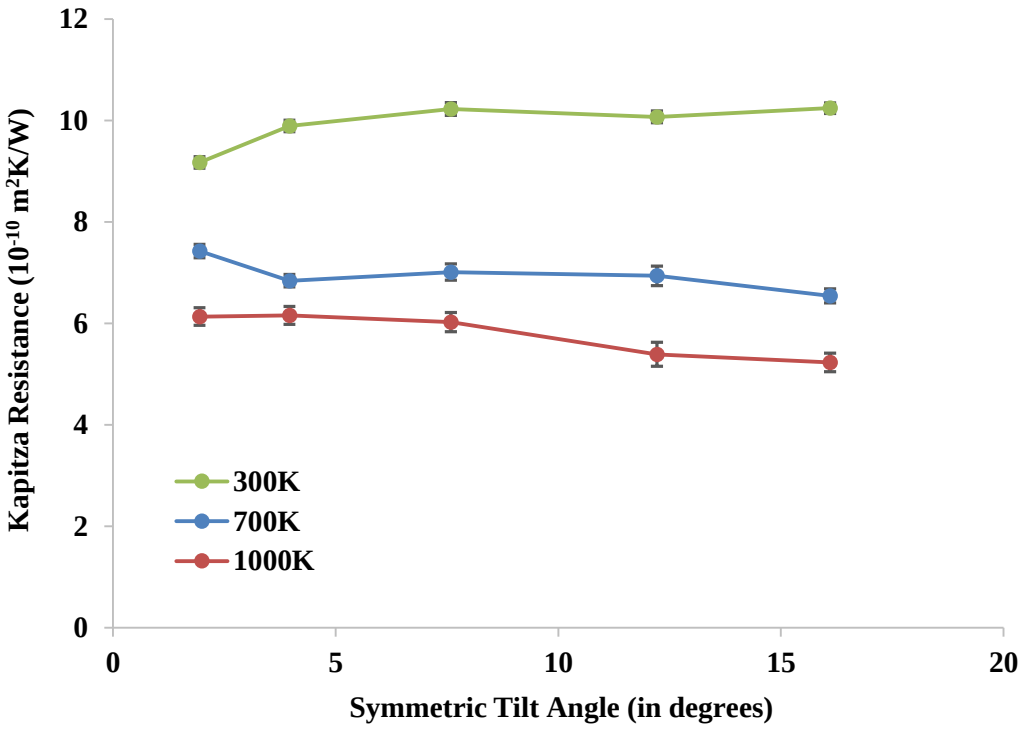

Figure 33: Influence of temperature on Kapitza resistance at different symmetric tilt GBs

shifted laterally in the transverse direction, this also causes the atomic positions to be different from what one would expect from a typical system. These actions possibly have a cumulative effect on the vibrational mismatch at the GB that overshadows the effect of GB tilt angle.

From Figure 33, it is observed that the temperature effect on R_k for different tilt angle GBs was very peculiar. At low temperature, R_k was observed to increase with an increase in the tilt angle for the low angle GB systems, and eventually levelled off for the high angle incoherent GB systems. However, the overall change in R_k was insignificant. With an increase in temperature, this effect appeared to wean off and for the tilt angles evaluated, the R_k for each system was within the statistical error of each other. However, it stands to argue that the error bars on the above data points only serve to prove the good statistics obtained on the data. These results are still preliminary and have not been verified for repeatability. It is possible that R_k calculated for different cases might turn out to be within the error bar range of each other. To resolve this issue, vibrational density of states calculations were performed for 3.9632°, 7.5891°, and 16.1021° undoped GB systems, as depicted in Figure 34.

As is evident from the figure, the vibrational density of states profiles closely followed each other for the three GBs evaluated with only small difference in the height of the peaks, indicating that the scattering of phonons can be assumed to be independent of the grain orientation for the symmetric tilt boundaries studied. However, this might hold only for symmetric tilt GB systems considered in the present study. On the contrary, Crocombette *et al*. [34] observed that in low angle GB systems obtained from edge dislocations R_k increased as the GB misorientation angle increased.

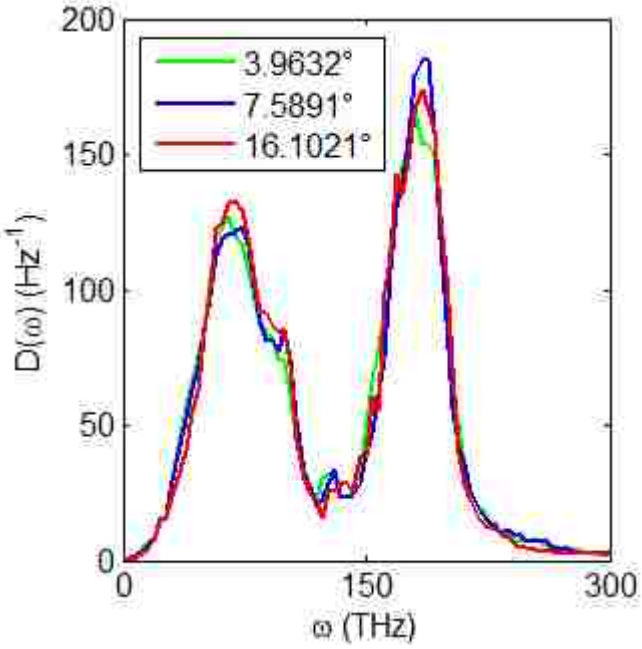

Figure 34: Vibrational Density of States at the GB for 3.9632° (green), 7.5891° (blue), and 16.1021° (red) symmetric tilt GB systems.

8.3. Effect of Misorientation Angle on Dopant Contributions

The effect of dopants at the GB was discussed in detail in Chapter 6. The observations in the chapter were limited to symmetric 7.5891° tilt GB system. It is of interest to determine if R_k remains independent of the GB tilt angle in the presence of dopants at the GB. Dopants were characterized in the identical manner as done for the 7.5891° tilt angle system and selectively inserted at the GB in 3.9632° and 16.1021° tilt angle systems. Five different dopant concentrations, C, between 0.047 ML and 1.007 ML were examined. Keeping the strength of interaction between dopants, ε_{dd}, constant at 0.3 eV, R_k was calculated for the dopant/matrix interaction strengths, ε_{dm}, of 0.03 eV, and 0.3 eV. Following the procedure described in Section 4.2, simulations were run for 4 ns at 1000 K. For the 7.5891° symmetric tilt GB, it was found that while the dopant segregation profile

comprised of layers in the limit where $\varepsilon_{dm} = \varepsilon_{dd} = 0.3$ eV, and R_k was relatively insensitive to C; in the limit where the ε_{dm} is less than ε_{dd}, the dopants segregated to form clusters. Similar observations were made for the 3.9632° and 16.1021° tilt angle GB systems. In the layered limit, it was observed that R_k changed nearly identically with the increase in C irrespective of the GB orientation, as can be seen in Figure 35. The dopants were determined to be spread out in layered structure at the GB cross section. More interesting observation was made at the clustered limit. At low dopant concentrations, the increase in R_k was determined to be independent of the GB orientation. However, once the dopant concentration increased past a certain critical concentration, R_k increased with the decrease in GB orientation.

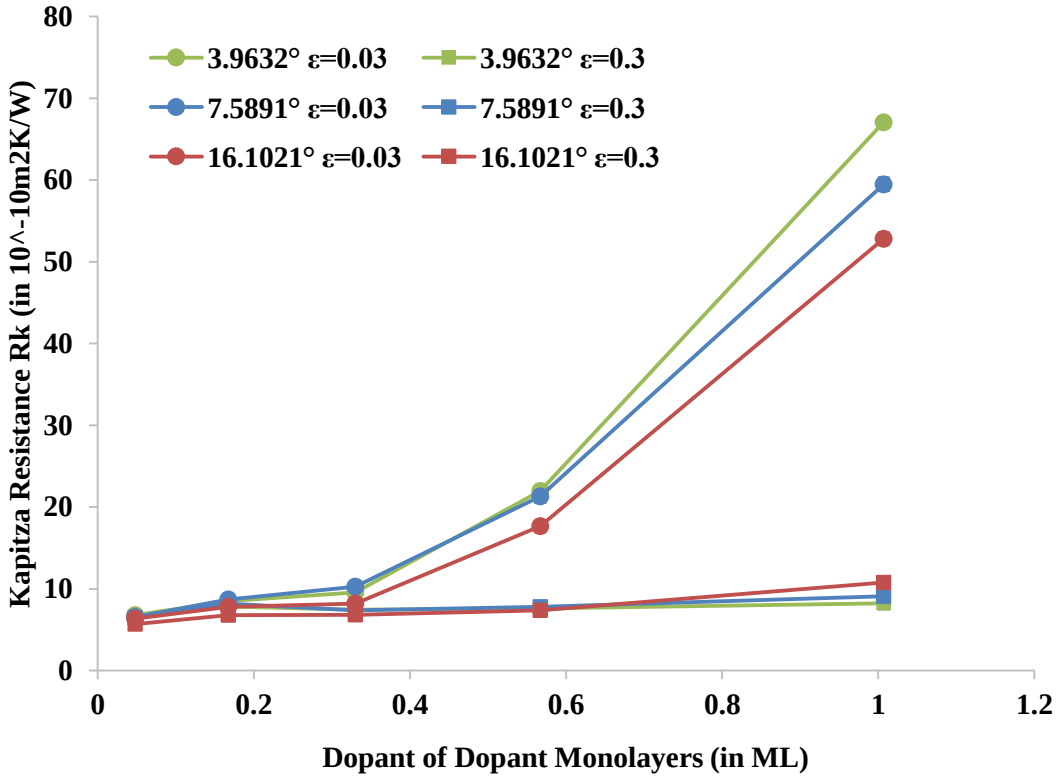

Figure 35: Influence of dopant concentration on Kapitza resistance at different symmetric tilt GBs

R_k increased by consistently by about 10% as the GB misorientation angle decreased from 16.1021° to 3.9632°. The percentage gain in R_k cannot be considered significant and the variation in R_k was examined by calculating the vibrational density of states distribution for the three systems at the GB for both the clustered and the layered limits and the highest dopant concentration. Similar to previous analyses, a 6 Å thick plane identified to straddle the GB region and vibrational density of states were calculated by taking the Fourier transform of the velocity correlation function. The procedure is described in detail in Section 7.5. Vibrational density of states obtained at the GB for the three misorientation angle systems is shown in Figure 36. In the clustered limit the vibrational density of states distribution for the 16.1021° tilt angle GB system observed a relative decline in the frequency range 180 THz – 200 THz, while the vibrational density of states distribution for the three different symmetric tilt angle GBs largely overlapped for the remaining frequencies. This observation is in somewhat contradiction to the observed trend for R_k from Figure 35 indicating that a difference of about ±10% between R_k might not be as significant and could potentially be within the error bars obtained from simulations performed for similar degenerate systems.

In the layered limit, the vibrational density of states distribution for 3.9632° and 16.1021° misorientation angle GB systems closely overlapped each other, and the 7.5891° misorientation angle GB system had vibrational density of states distribution consistently higher than those of the other two systems, despite the observed R_k for 16.1021° misorientation angle system about 10% higher than the other two systems in the layered limit. These observations only highlight that the presence of dopants at the GB potentially affects the sensitivity of R_k on the vibrational density of states at the GB.

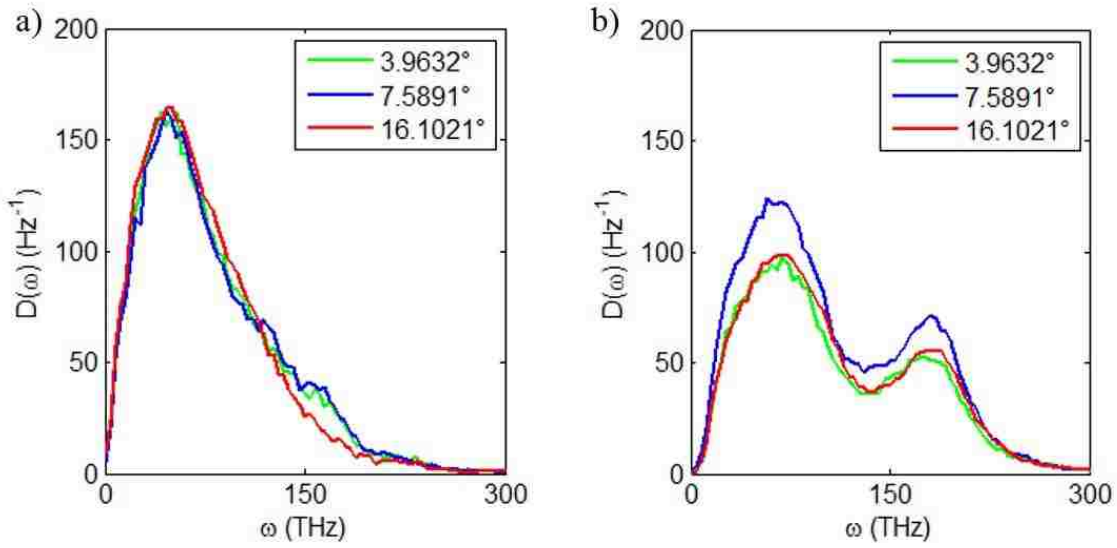

Figure 36: Vibrational density of states at the GB in a) clustered limit and b) layered limit for 3.9632° (green), 7.5891° (blue), and 16.1021° (red) symmetric tilt GB systems at highest dopant concentration

8.4. Influence of Grain Boundary Energy

Grain boundary energy was briefly discussed in Section 3.3.2. As pointed out in the previous section, each GB in a stable nano-structured material will likely have a different GB energy associated with it. Schelling *et al.* [76] investigated three different twist boundaries that inherently exhibit different energy at GB due to the differences in the degree of disorder associated with the twist angles. They observed that for the systems with higher disorder at the GB had a significantly higher R_k compared to the lower energy and more order twist GBs. GB created using symmetry and shift as well as introducing small edge dislocations were studied by Crocombette *et al*. [34] and they observed that for the low angle dislocation generated GBs, both R_k and the GB energy increased monotonously with an increase in the angle, whereas no clear relationship was observed between GB energy and R_k for the symmetric tilt GB systems.

Building off of the available literature, the effect of dopants in degenerate symmetric tilt GBs with small differences in GB energy on R_k was examined in the work presented here. From the shift procedure used to build 3.9632° tilt angle boundary, two different scroll combinations were chosen that resulted in a low GB energy. Figure 37 shows the minimum energy for each of the iteration of lateral scroll analyzed plotted in the increasing order of GB energy for three different atomic deletion criteria. Besides the bicrystal configuration with the lowest GB energy of 4.2214 eV, a second configuration was randomly selected (GB energy 4.7076 eV). From Figure 37, given the stiffness of SiC and the resulting higher slope for increase in GB energy, the two low energy (LE) and high energy (HE) configurations can be regarded as degenerate.

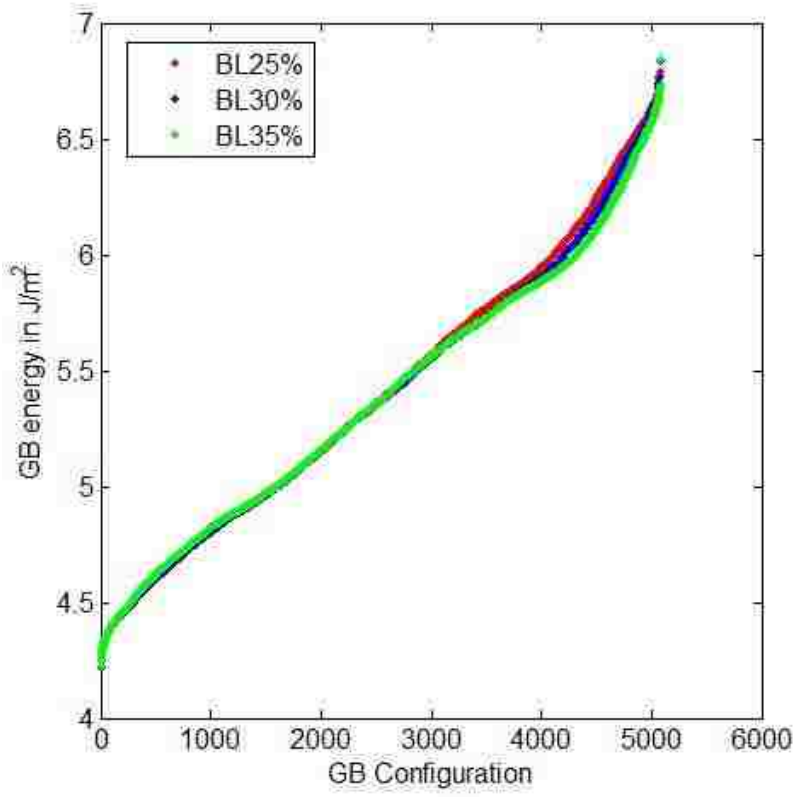

Figure 37: GB energy vs. GB configuration iteration (sorted by increasing GB energy) for atomic deletion criteria of 25%, 30%, and 35% of the equilibrium bond length in 3.9632° symmetric tilt GB

Simulations were performed for calculating R_k for undoped systems built for both the LE and HE configuration at 1000 K and was determined to be 5.8491 ± 0.2132 W/m^{2}K and 6.5196 ± 0.1764 W/m^{2}K for the LE and HE systems, respectively. Although R_k increased with an increase in GB energy, the increase was not significant. Dopant atoms were introduced at the GBs in both the LE and HE systems to examine if dopant segregation profiles are affected by the GB energy. Five different dopant concentrations, *C*, of 0.048 ML, 0.167 ML, 0.33 ML, 0.576ML and 1.007ML were evaluated using the procedure described in Section 4.2 for both the clustered and the layered limit. Figure 38 shows R_k plotted against *C* and undoped cases for both the LE and HE systems

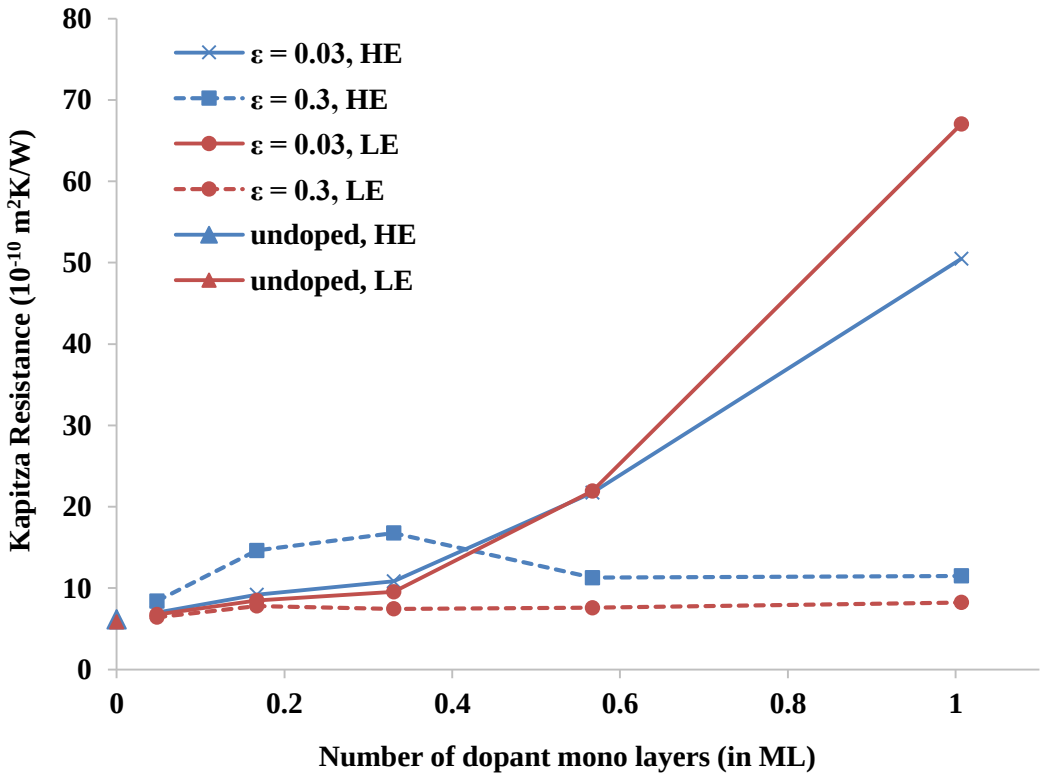

Figure 38: Kapitza resistance versus dopant concentration for high energy (squares) and low energy (circles) configurations; and the clustered (solid lines), the layered (dashed lines) limits and the undoped systems (triangle)

For both HE and LE systems, R_k was increased nearly identically with the increase in C until C = 0.567 ML, beyond which R_k for the LE system had a more significant rise compared to the HE system. For the highest concentration, R_k for the LE system was about 35% greater than that for the HE system. The layered limit exhibited very different trend for R_k compared to the clustered limit. The HE systems in the layered limit had consistently higher R_k than the LE systems for all C. More importantly, the HE systems in the layered limit exhibited rapid increase in R_k for lower dopant levels which eventually subsided with further increase in C. On the contrary, LE systems exhibited a much smaller rate on increase in R_k with the increase in C. A closer inspection of GB structure revealed that the HE systems observed a higher loss of order at the GB. Figure 39 shows the atomic structure at both the GBs in a simulation cell for the undoped system and the doped systems with dopant concentration C=0.33 ML and C=1.007 ML in HE and LE cases. It was determined that for the undoped systems, the loss of order at the GBs was not very significant which explained the negligible difference in R_k as mentioned earlier. For the clustered limit, at C=0.33 ML, it can be seen that the HE systems exhibit higher loss of order at the GBs compared to the LE systems as the matrix atoms near the GB are no longer at the ideal lattice positions. This explains the slightly higher R_k for the HE system compared to the LE system as seen in Figure 38. However, at C=1.007 ML, the HE systems did not exhibit a loss of order similar to what was observed for C=0.33ML.

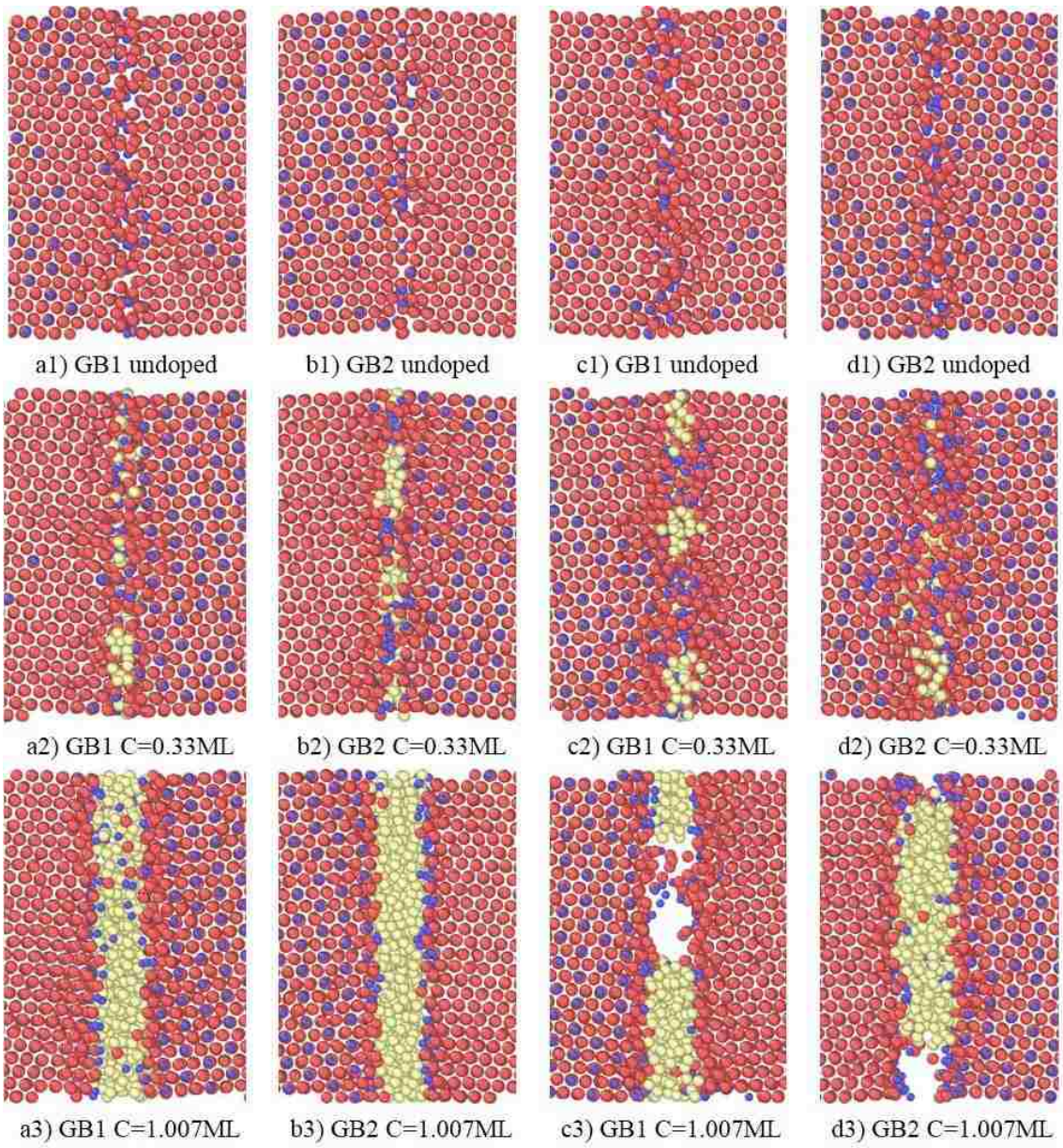

Figure 39: GB disorder at GB1 (columns a & c) and GB2 (columns b & d) as indicated in Figure 20 a) for undoped and doped systems in the clustered limit. The first two columns are for the LE systems and the last two columns are for HE systems.

For the layered limit, a much more significant loss or order in observed at the GBs as shown in Figure 40. The loss of order for *C*=0.33 ML case was higher than that for the case *C*=1.007 ML. Moreover, while for all the simulation results presented earlier, the resistance at the two GBs was with in $\pm 1\times10^{-10}$ m^2K/W, the different degrees of disorder

at the two GBs in HE systems resulted in a non-trivial difference between the corresponding R_k between the two GBs. While these observations are important, a more conclusive result requires additional simulations to be performed for the dopant concentrations studied at a few more degenerate GB energy levels.

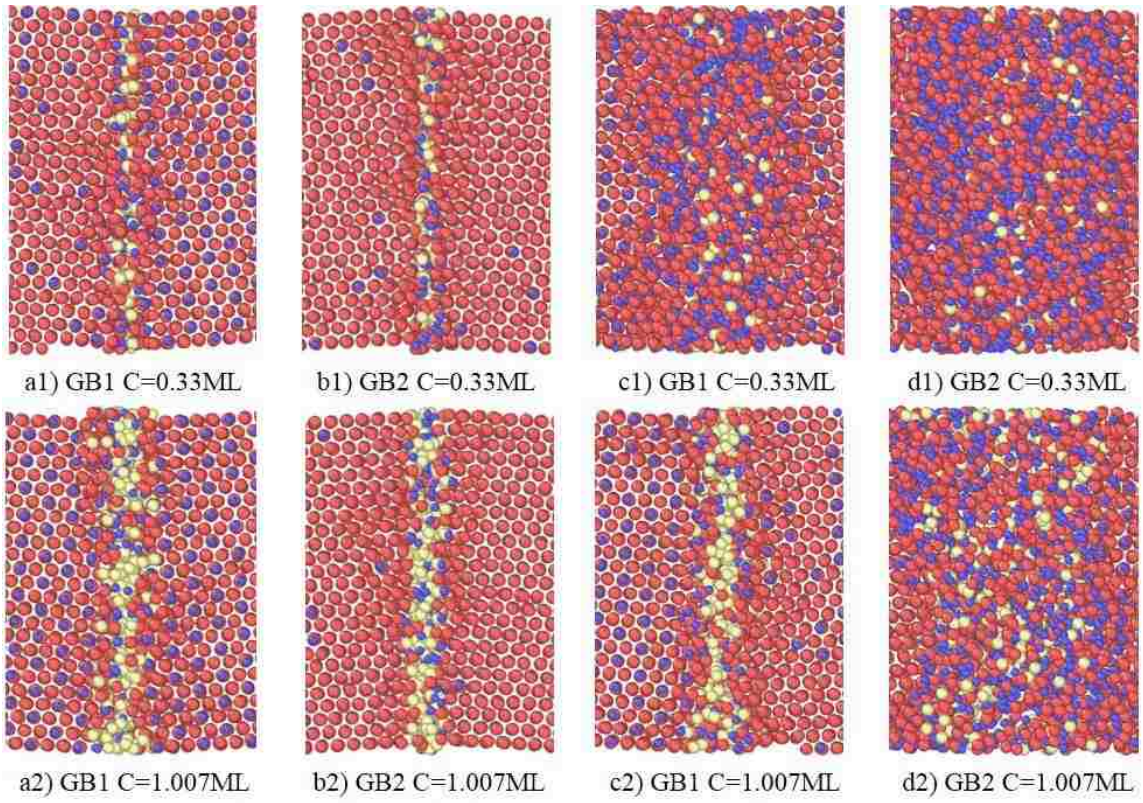

Figure 40: GB disorder at GB1 (columns a & c) and GB2 (columns b & d) as indicated in Figure 20 a) for doped systems in the layered limit. The first two columns are for the LE systems and the last two columns are for HE systems.

8.5. Summary

To summarize, several GB misorientation angles were investigated to assess the role of GB orientation on R_k. For the methodology used to build the GB system, R_k was determined to be insensitive of the GB orientation for the range of system temperatures examined. This was further confirmed from the vibrational density of states analyses. The

presence of dopants at the GBs appeared to result in different degree of phonon scattering, however, the vibrational density of states analyses performed for the doped systems did not reveal any difference in distinct loss of phonon modes between the three misorientation angle systems examined. To build a better understanding of the observed results, more simulations with other degenerate systems and the same dopant concentrations needs to be performed.

Finally, the effect of GB energy on R_k was investigated for 3.9632° misorientation angle symmetric tilt GB. Dopants in the layered limit caused a greater loss of order at the GBs in high GB energy systems. It was also observed that with the loss of order, the GB were no longer distinct and appeared to broaden, resulting in dopants occupying a larger section of the system. The lack of prominence of the loss of order in the undoped and clustered limit cases of the high energy system serve to bolster the need to better understand the influence of GB energy on thermal transport across the GB.

Chapter 9

9. Conclusions and Future Work

9.1. Conclusions

Phonon scattering at grain boundary interfaces is a proven solution to lowering thermal conductivity in semi-conductor materials for applications focusing on harvesting energy from high temperature surfaces and exhausts using thermoelectric generators. The continued miniaturization of microelectronics takes advantage of this effect and with additional opportunities of improvement in the figure of merit available via usage of appropriate dopants; understanding thermal transport at the phonon level will be required to enable further improvements in the design of nanostructured semiconductors. This will allow reducing the thermal conductivity, and thus the potential for high ZT.

In this dissertation, thermal transport across segregated grain boundaries in β-SiC was examined using non-equilibrium MD (NEMD) simulations. The aim of this study was to quantify the impact of boundary dopant concentration on Kapitza resistance for different dopant/matrix interaction strengths. These results indicate that dopants can significantly affect thermal transport in polycrystalline β-SiC by increasing R_k at GBs. The magnitude of the change observed in R_k greatly depends on the strength of the dopant interactions and the shape of the segregation profile.

Another determination from the work was that the degrees of phonon scattering is affected by the dopant/matrix interaction strength, thereby causing different GB structure and the associated R_k. Moreover, it was found that boundary segregation also mitigated the

increase in boundary conductance with increasing temperature, especially at high dopant levels. It was also found that doping decreased the number of optical modes, and therefore the conversion from optical to acoustic modes is an important mechanism in dictating boundary resistance. Finally, it was observed that while the GB orientation did not appear to have substantial impact on R_k, given the probability of different boundaries having different local energy, could influence the degree of segregation at the GB and thus influence R_k.

The results suggest that it may be possible to tailor the thermal response of other polycrystals by controlling the degree of boundary segregation. For example, one avenue for controlling segregation exploits the occurrence of complexion transitions at boundaries. By varying parameters, such as the temperature or the applied stress, it is possible to induce transitions between different complexions having, for example, different interfacial chemistry and/or structure[127]. Furthermore, by controlling the chemistry and composition of dopants as well as system temperature, one may be able to effectively tune boundary resistance by dictating segregation profiles. In particular, given that a reduction in elastic energy is a driving force for segregation, it may be advantageous to select dopants with relatively large atomic radii to promote segregation. It may also be possible to induce layering (complexion) transitions at a grain boundary to control the segregation profile and, thereby, the boundary resistance[128].

9.2. Suggestions for Future Work.

Some interesting contributions were made in this work. Most importantly, it was showcased that opportunities are indeed available to improve the performance of materials

that have not been considered for thermoelectric applications. However, this work also opened several questions that need to be answered for better understanding of the underlying principles before a suitable application. Some of these are listed below:

9.2.1. Selective Matrix Element/Dopant Affinity

In the entirety of this work, dopant were modelled such that they interacted identically with both Si and C. However, given the difference in atomic size between Si and C, dopant might have a stronger affinity to one of the two matrix elements than the other. Two smaller simulations were performed to probe the effect of selective dopant/matrix element affinity on R_k in symmetric 7.5892° tilt angle GB system at 1000 K and dopant concentration of 1.007 ML. Keeping dopant/dopant interaction strength constant for both cases, ε_{dd} = 0.3 eV, dopants/matrix interaction strengths were defined as ε_{dSi} = 0.3 eV and ε_{dC} =0.03 eV and vice-versa. The mass of dopant atoms was defined to be the same as that of elemental Si. It was observed that R_k was reduced to nearly half of what was presented in Chapter 6 in both the cases. However, of the two analyses, the one where dopants had stronger affinity towards C compared to Si exhibited a higher R_k. A possible explanation for this observation is that the identical mass of dopants and Si possibly provided a greater overlap in the phonon density of states to reduce phonon scattering at dopant/Si interface. More analyses with different variations in strengths of interaction as well as mass of the dopant should be able to explain the phenomenon more completely.

9.2.2. Phonon Dispersion Curves Analysis

In Chapter 7, it was determined that the dopants segregating at the GB resulted in a reduction of the number of optical modes in the system. It is of great interest to determine which specific optical modes are lost at the GB and how they are affected by the different

dopant/matrix interaction strength and dopant mass. Schelling *et al.* [98] determined that the lack of transmission channels corresponding to any particular phonon mode across the GB can result in an interconversion between optical and acoustic phonon modes. Phonon dispersion analyses should be able to provide the information regarding which new acoustic modes are created as optical modes get scattered at the GB.

9.2.3. Multiple Dopant Layers

Super-lattices have been studied in great length and have been determined to be very promising in semi-conductor applications. An offshoot of the same concept as applicable to this work is multiple dopant species. In the work presented in this report, only one dopant species was used in any simulation. It is of interest to see how either a binary dopant species or multiple layers of different dopant species would affect thermal transport across the GB. It is also of interest to see if an advantage can be drawn from the presence of clustering and layering dopants present at the GB at the same time, particularly given the effect of boundary energy on dopant segregation behavior.

9.2.4. Real Dopants

The thermal transport properties for LJ solids have also been thoroughly characterized in numerous studies. However, the use of LJ interatomic potential to describe the dopant atoms does not provide results specific to any material. In order to draw accurate performance of SiC for thermoelectric applications, it is necessary to identify real materials for dopants and ascertain their impact on thermal transport across the GBs. Some of the dopants that are of interest for the future work are Boron and Aluminum. While good interatomic interactions potential descriptions are available for Si-Al as well as B-C, new interatomic interaction potentials will need to be developed to describe the interactions

between Si-B as well as C-Al. The results corresponding the effect of dopant mass and dopant/matrix interaction strength should prove useful is identifying more promising dopant materials.

Appendix A

Radial Distribution Function

Radial distribution function, *g(r)* or RDF, is an example of pair correlation function which describes the atomic packing in a system. In a homogenous system of *N* atoms in a given volume *V*, *g(r)* represents the probability of finding an atom at distance *r* from a given atom. RDF is an effective way of describing the average structure of a molecular system like liquids and solid crystals.

To calculate *g(r)*, an atom is chosen at random and a sphere of radius equal to the cut-off distance from the interatomic interaction potential used to describe the material, and the chosen atom as center is constructed. The sphere is then subdivided into smaller shells of thickness *dr* at a distance *r* from the chosen atom as shown in the in Figure 41.

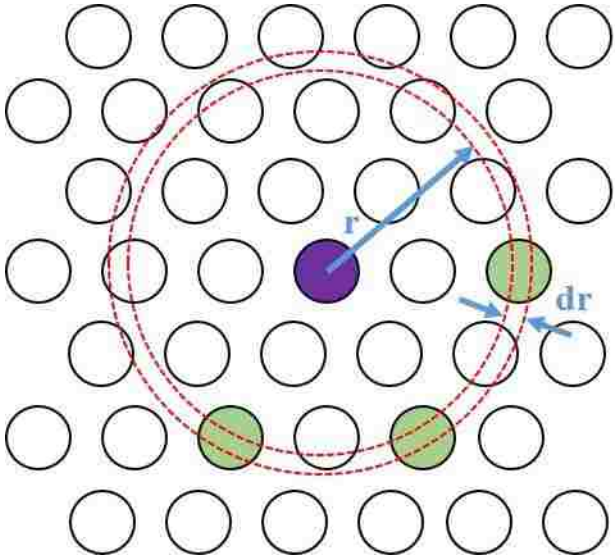

Figure 41: Space discretization for the evaluation of the radial distribution function.

For each shell, the number of atoms *n(r)* in that shell are determined. *g(r)* is then calculated by dividing the number by the volume of each shell and the average density of atoms ρ in the system as:

$$g(r) = \frac{n(r)}{\rho 4\pi r^2 dr} \tag{45}$$

The process is repeated over all the atoms in the system to obtain a statistically good *g(r)*. To further improve the statistics in the calculations, a snapshot of atomic positions was saved every 1000 time steps using LAMMPS and the average position of the atoms was obtained by averaging over 100 such snapshots. The process was repeated for Si–Si, Si-C and C-C pairs. The *g(r)* and the coordination number as a function of distance *r* from the central atom are provided in Table 6. Coordination number is a cumulative quantity that determines the total number of atoms within a radial distance r from the central atom.

Table 6: Radial Distribution function and coordination number for β-SiC at 500 K

Distance (in Å)	*g(r)* Si-Si	coord(r) Si-Si	*g(r)* Si-C	coord(r) Si-C	*g(r)* C-C	coord(r) C-C
0.01	0	0	0	0	0	0
0.03	0	0	0	0	0	0
0.05	0	0	0	0	0	0
0.07	0	0	0	0	0	0
0.09	0	0	0	0	0	0
0.11	0	0	0	0	0	0
0.13	0	0	0	0	0	0
0.15	0	0	0	0	0	0
0.17	0	0	0	0	0	0
0.19	0	0	0	0	0	0

Distance (in Å)	*g(r)* Si-Si	coord(r) Si-Si	*g(r)* Si-C	coord(r) Si-C	*g(r)* C-C	coord(r) C-C
0.21	0	0	0	0	0	0
0.23	0	0	0	0	0	0
0.25	0	0	0	0	0	0
0.27	0	0	0	0	0	0
0.29	0	0	0	0	0	0
0.31	0	0	0	0	0	0
0.33	0	0	0	0	0	0
0.35	0	0	0	0	0	0
0.37	0	0	0	0	0	0
0.39	0	0	0	0	0	0
0.41	0	0	0	0	0	0
0.43	0	0	0	0	0	0
0.45	0	0	0	0	0	0
0.47	0	0	0	0	0	0
0.49	0	0	0	0	0	0
0.51	0	0	0	0	0	0
0.53	0	0	0	0	0	0
0.55	0	0	0	0	0	0
0.57	0	0	0	0	0	0
0.59	0	0	0	0	0	0
0.61	0	0	0	0	0	0
0.63	0	0	0	0	0	0
0.65	0	0	0	0	0	0
0.67	0	0	0	0	0	0
0.69	0	0	0	0	0	0
0.71	0	0	0	0	0	0
0.73	0	0	0	0	0	0

Distance (in Å)	*g(r)* Si-Si	coord(r) Si-Si	*g(r)* Si-C	coord(r) Si-C	*g(r)* C-C	coord(r) C-C
0.75	0	0	0	0	0	0
0.77	0	0	0	0	0	0
0.79	0	0	0	0	0	0
0.81	0	0	0	0	0	0
0.83	0	0	0	0	0	0
0.85	0	0	0	0	0	0
0.87	0	0	0	0	0	0
0.89	0	0	0	0	0	0
0.91	0	0	0	0	0	0
0.93	0	0	0	0	0	0
0.95	0	0	0	0	0	0
0.97	0	0	0	0	0	0
0.99	0	0	0	0	0	0
1.01	0	0	0	0	0	0
1.03	0	0	0	0	0	0
1.05	0	0	0	0	0	0
1.07	0	0	0	0	0	0
1.09	0	0	0	0	0	0
1.11	0	0	0	0	0	0
1.13	0	0	0	0	0	0
1.15	0	0	0	0	0	0
1.17	0	0	0	0	0	0
1.19	0	0	0	0	0	0
1.21	0	0	0	0	0	0
1.23	0	0	0	0	0	0
1.25	0	0	0	0	0	0
1.27	0	0	0	0	0	0

Distance (in Å)	*g(r)* Si-Si	coord(r) Si-Si	*g(r)* Si-C	coord(r) Si-C	*g(r)* C-C	coord(r) C-C
1.29	0	0	0	0	0	0
1.31	0	0	0	0	0	0
1.33	0	0	0	0	0	0
1.35	0	0	0	0	0	0
1.37	0	0	0	0	0	0
1.39	0	0	0	0	0	0
1.41	0	0	0	0	0	0
1.43	0	0	0	0	0	0
1.45	0	0	0	0	0	0
1.47	0	0	0	0	0	0
1.49	0	0	0	0	0	0
1.51	0	0	0	0	0	0
1.53	0	0	0	0	0	0
1.55	0	0	0	0	0	0
1.57	0	0	0	0	0	0
1.59	0	0	0	0	0	0
1.61	0	0	0	0	0	0
1.63	0	0	0	0	0	0
1.65	0	0	0	0	0	0
1.67	0	0	0	0	0	0
1.69	0	0	0	0	0	0
1.71	0	0	7.60E-04	2.75E-05	0	0
1.73	0	0	7.56E-03	3.08E-04	0	0
1.75	0	0	0.075	0.003	0	0
1.77	0	0	0.445	0.020	0	0
1.79	0	0	1.742	0.089	0	0
1.81	0	0	5.001	0.292	0	0

Distance (in Å)	*g(r)* Si-Si	coord(r) Si-Si	*g(r)* Si-C	coord(r) Si-C	*g(r)* C-C	coord(r) C-C
1.83	0	0	10.301	0.719	0	0
1.85	0	0	15.702	1.384	0	0
1.87	0	0	18.270	2.175	0	0
1.89	0	0	16.531	2.905	0	0
1.91	0	0	11.800	3.438	0	0
1.93	0	0	6.855	3.754	0	0
1.95	0	0	3.274	3.908	0	0
1.97	0	0	1.300	3.970	0	0
1.99	0	0	0.433	3.992	0	0
2.01	0	0	0.127	3.998	0	0
2.03	0	0	0.031	3.9996	0	0
2.05	0	0	0.007	3.99994	0	0
2.07	0	0	8.96E-04	3.99999	0	0
2.09	0	0	2.31E-04	4	0	0
2.11	0	0	0	4	0	0
2.13	0	0	0	4	0	0
2.15	0	0	0	4	0	0
2.17	0	0	0	4	0	0
2.19	0	0	0	4	0	0
2.21	0	0	0	4	0	0
2.23	0	0	0	4	0	0
2.25	0	0	0	4	0	0
2.27	0	0	0	4	0	0
2.29	0	0	0	4	0	0
2.31	0	0	0	4	0	0
2.33	0	0	0	4	0	0
2.35	0	0	0	4	0	0

Distance (in Å)	*g(r)* Si-Si	coord(r) Si-Si	*g(r)* Si-C	coord(r) Si-C	*g(r)* C-C	coord(r) C-C
2.37	0	0	0	4	0	0
2.39	0	0	0	4	0	0
2.41	0	0	0	4	0	0
2.43	0	0	0	4	0	0
2.45	0	0	0	4	0	0
2.47	0	0	0	4	0	0
2.49	0	0	0	4	0	0
2.51	0	0	0	4	0	0
2.53	0	0	0	4	0	0
2.55	0	0	0	4	0	0
2.57	0	0	0	4	0	0
2.59	0	0	0	4	0	0
2.61	0	0	0	4	0	0
2.63	0	0	0	4	0	0
2.65	0	0	0	4	0	0
2.67	0	0	0	4	0	0
2.69	0	0	0	4	0	0
2.71	0	0	0	4	0	0
2.73	0	0	0	4	0	0
2.75	0	0	0	4	0	0
2.77	0	0	0	4	1.05E-04	1.00E-05
2.79	0	0	0	4	1.04E-04	2.00E-05
2.81	0	0	0	4	4.61E-04	6.50E-05
2.83	0	0	0	4	0.002	2.40E-04
2.85	0	0	0	4	0.009	0.001
2.87	0	0	0	4	0.033	0.005
2.89	0	0	0	4	0.120	0.017

Distance (in Å)	*g(r)* Si-Si	coord(r) Si-Si	*g(r)* Si-C	coord(r) Si-C	*g(r)* C-C	coord(r) C-C
2.91	4.77E-05	5.00E-06	0	4	0.341	0.053
2.93	7.53E-04	8.50E-05	0	4	0.862	0.144
2.95	0.057	0.006	0	4	1.944	0.353
2.97	1.150	0.132	0	4	3.794	0.768
2.99	6.826	0.887	0	4	6.505	1.487

From the Table above, it was observed that for either Si or C as central atom, the four corresponding first neighbor pairing C/Si atoms were within a distance of 2.1 Å from the central atom. For Si as the central atom, the second neighbor Si atoms don't surface until 2.89 Å away from the central atom whereas for C as the central atom, the second neighbor C atoms start cropping up at about 2.75 Å from the central atom. As such a cut-off distance of 2.65 Å was determined appropriate to ensure that all second neighbor interactions were discarded from the simulations.

The process was repeated for 900 K and the cut off distance determined to hold even after accounting for the lattice expansion at the higher temperature.

Appendix B

Lattice Dynamics: Normal mode analysis

MD simulations are ideal for predicting properties such as thermal conductivity and thermal resistance. However, model level details such as identifying individual contribution of different phonons to thermal transport is more easily obtained from lattice dynamics (LD) calculations that involve a focused study of atomic vibrations in a crystal. LD calculations are performed in reciprocal-space coordinates instead of the real space coordinates of atomic positions. Reciprocal lattice allows scaling down the phonon wavelengths that can be infinitely large to distances comparable to interatomic spacing, making it more manageable.

Harmonic approximation is one of the key approximations in LD calculations where the Taylor series expansion of the potential energy *E* between two atoms is truncated after the second-order term [129]. Although, harmonic approximation fails to provide information pertaining to inelastic phonon scattering, it is very powerful as it provides an exact solution and can be easily adapted to incorporate quantum mechanics. Under the harmonic approximation, the potential energy term can be written as:

$$E = E_0 + \sum_{\tau} \left.\frac{\partial E}{\partial u_\tau}\right|_0 u_\tau + \frac{1}{2}\sum_{\tau}\sum_{\tau'} \left.\frac{\partial^2 E}{\partial u_\tau \partial u_{\tau'}}\right|_0 u_\tau u_{\tau'} + \ldots, \tag{46}$$

where *u* is a small displacement vector from the equilibrium position $r_i(t) = r_i^0 + u_\tau(t)$ and τ = (*i*, α) refers to the perturbation along the α^{th} carterian coordinate component of the i^{th} atom. When evaluating at equilibrium, the first derivative reduces to zero as the atoms don't experience any net force in equilibrium. Therefore the equation can be rewritten as:

$$E(r) = E_0 + \frac{1}{2}\sum_{\tau,\tau'} \Phi_{\tau,\tau'} u_\tau u_{\tau'}\,, \tag{47}$$

$$\Phi_{\tau,\tau'} = \frac{\partial^2 E}{\partial u_\tau \partial u_{\tau'}} = -\frac{\partial F_\tau}{\partial u_{\tau'}} = \frac{\partial F_{\tau'}}{\partial u_\tau} \tag{48}$$

Φ is called the force constant matrix or the Hessian matrix [57, 117, 118]. For an N atom system in three dimensions, Φ will be a 3N × 3N matrix as τ varies from 1 to 3N. The Newtonian equations of motion resulting from the perturbations for each atom can then be derived from the expression for potential energy in equation (48) as:

$$m_\tau \frac{d^2 r_\tau(t)}{dt^2} = -\sum_{\tau'} \Phi_{\tau\tau'}\left[r_{\tau'}(t) - r_{\tau'}^0\right] = -\sum_{\tau'} \Phi_{\tau\tau'} u_{\tau'}(t) \tag{49}$$

The system can be assumed similar to a mass spring system and the linear notation of the equation allows to seek a solution of the form

$$u_\tau(t) = e_\tau \cos(\omega t + \phi) \tag{50}$$

The resulting set of equations define the vibrational modes of the system with amplitude e_τ and frequencies ω. The linear system of equations will have a solution for e if the determinant of the matrix $\Phi_{\tau,\tau'}/\sqrt{m_\tau m_{\tau'}} - \omega^2$ is equal to zero. The system has 3N eigenvalues and for each eigenvalue, there is an eigenvector of 3N components. The eigenvalues obtained from diagonalizing the Hessian matrix, are the relevant phonon modes for the system in accordance with the equation:

$$\sum_{\tau'} \frac{\Phi_{\tau,\tau'}}{\sqrt{m_\tau m_{\tau'}}} e_{\tau'}^\lambda = \omega_\lambda^2 e_\tau^\lambda \tag{51}$$

Relevant vibrational modes for β-SiC was obtained by an eigenmode analysis of the Hessian matrix for an undoped, perfect crystal of size 3×2×2 unit cells. Small perturbations were introduced in all three dimensions for each atom and the Hessian matrix

was built by taking the negative of the resulting forces on all other atoms with respect to the perturbation introduced in any atom. The expanded hessian matrix is shown in Table 7.

Table 7: Hessian Matrix for 3D N atom system. The subscript for τ shows the direction for the perturbation and the force vector (X, Y or Z) on atom (1, 2, 3, …N)

$$\begin{bmatrix}
\frac{\partial F_{\tau'_{1X}}}{\partial u_{\tau_{1X}}} & \frac{\partial F_{\tau'_{1Y}}}{\partial u_{\tau_{1X}}} & \frac{\partial F_{\tau'_{1Z}}}{\partial u_{\tau_{1X}}} & \frac{\partial F_{\tau'_{2X}}}{\partial u_{\tau_{1X}}} & \cdot & \cdot & \cdot & \frac{\partial F_{\tau'_{NY}}}{\partial u_{\tau_{1X}}} & \frac{\partial F_{\tau'_{NZ}}}{\partial u_{\tau_{1X}}} \\
\frac{\partial F_{\tau'_{1X}}}{\partial u_{\tau_{1Y}}} & \frac{\partial F_{\tau'_{1Y}}}{\partial u_{\tau_{1Y}}} & \frac{\partial F_{\tau'_{1Z}}}{\partial u_{\tau_{1Y}}} & & & & & & \frac{\partial F_{\tau'_{NZ}}}{\partial u_{\tau_{1Y}}} \\
\frac{\partial F_{\tau'_{1X}}}{\partial u_{\tau_{1Z}}} & \frac{\partial F_{\tau'_{1Y}}}{\partial u_{\tau_{1Z}}} & \frac{\partial F_{\tau'_{1Z}}}{\partial u_{\tau_{1Z}}} & & & & & & \cdot \\
\frac{\partial F_{\tau'_{1X}}}{\partial u_{\tau_{2X}}} & & & \cdot & & & & & \cdot \\
\cdot & & & & \cdot & & & & \cdot \\
\cdot & & & & & \cdot & & & \cdot \\
\cdot & & & & & & \cdot & & \cdot \\
\frac{\partial F_{\tau'_{1X}}}{\partial u_{\tau_{NY}}} & & & & & & & \cdot & \frac{\partial F_{\tau'_{NY}}}{\partial u_{\tau_{NY}}} \\
\frac{\partial F_{\tau'_{1X}}}{\partial u_{\tau_{NZ}}} & \frac{\partial F_{\tau'_{1Y}}}{\partial u_{\tau_{NZ}}} & \cdot & \cdot & \cdot & \cdot & \cdot & \frac{\partial F_{\tau'_{NY}}}{\partial u_{\tau_{NZ}}} & \frac{\partial F_{\tau'_{NZ}}}{\partial u_{\tau_{NZ}}}
\end{bmatrix}$$

In the Hessian Matrix, each element was divided by the $\sqrt{m_\tau m_{\tau'}}$ where the two masses are the mass of the atom on which perturbation is introduced and the mass of the atom on which forces is measured as per the equation (51). The phonon modes were obtained by taking the square root of the eigenvalues of the above matrix. The histogram plot in Figure

42 shows the phonon density of states for β-SiC obtained by binning together the phonon modes obtained from LD calculations.

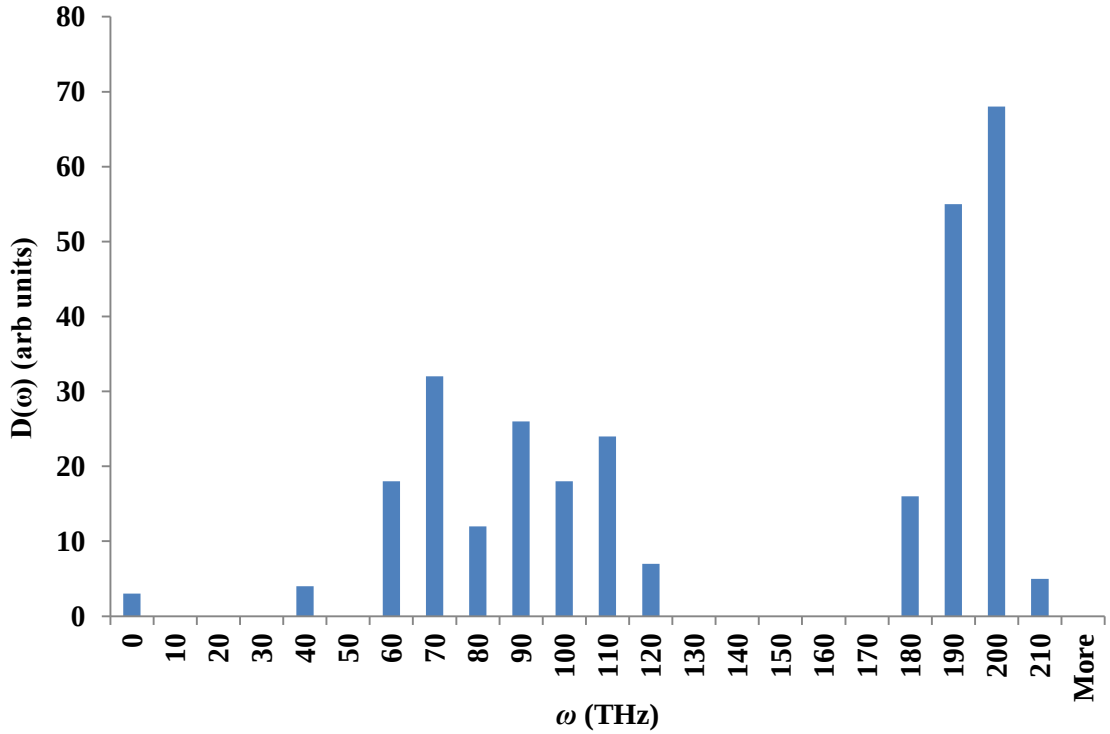

Figure 42: Vibrational density of states for β-SiC using LD calculations.

The eigenvectors were used to determine the direction of atomic vibration and wave propagation in order to differentiate between the optical and acoustic phonon modes. A characteristic of the acoustic phonon modes is that in a diatomic system, the two constituent atoms vibrate in the same direction. Whereas, the constituent atoms vibrate in the opposite direction when propagating via optical modes. A few examples observations are provided below: In the images below, Silicon is shown in red and carbon is shown in blue. The yellow arrows indicate the direction of motion, scaled to their corresponding magnitude as obtained from the eigenvector.

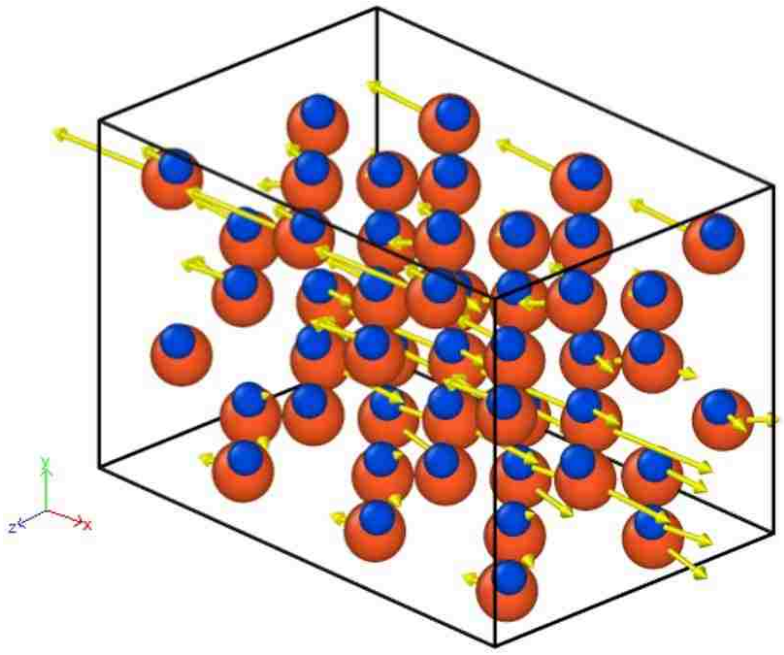

Figure 43: Atomic vibrations in acoustic mode for silicon (red) and carbon (blue) from an eigenmode analysis at $\omega = 55.2$ THz. The vibrations in Silicon atoms are higher than those in their pairing carbon atoms

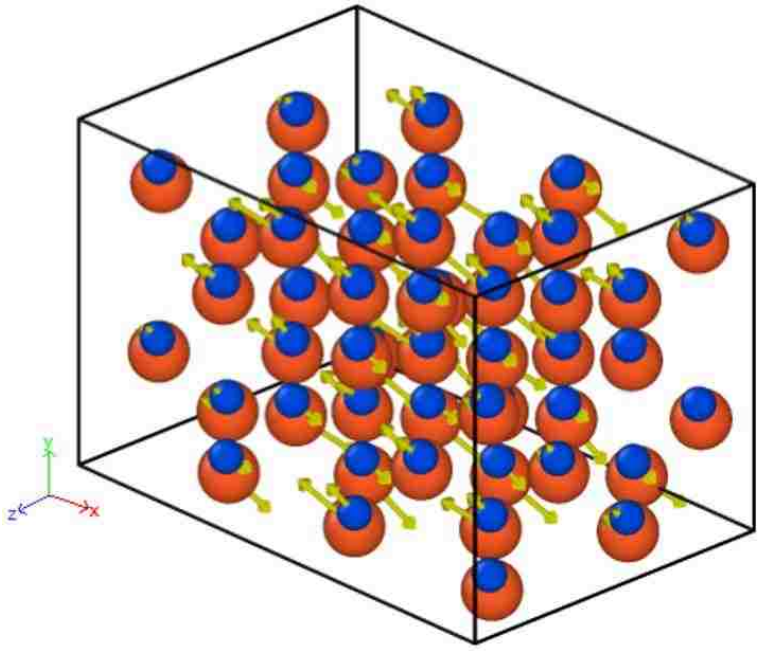

Figure 44: Atomic vibrations for acoustic mode silicon (red) and carbon (blue) from an eigenmode analysis at $\omega = 61.8$ THz. The higher vector magnitude for silicon indicates greater contribution to vibrational density of states.

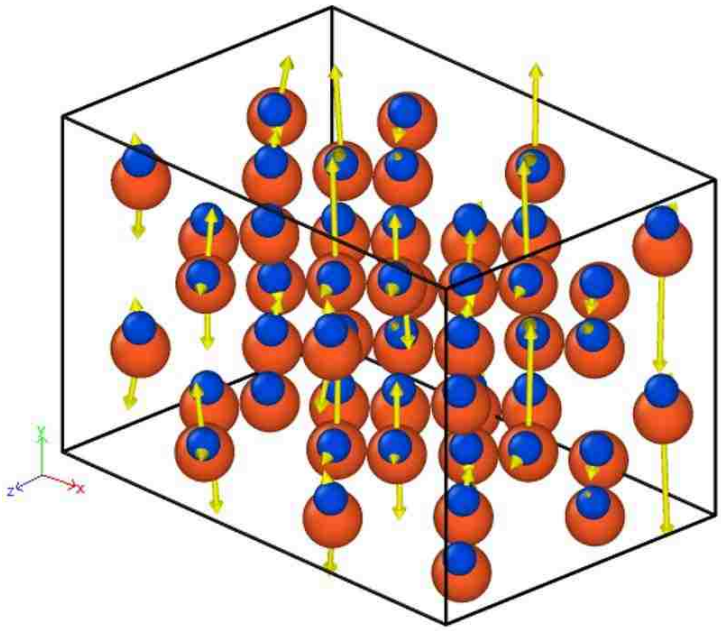

Figure 45: Atomic vibrations for silicon (red) and carbon (blue) from an eigenmode analysis at $\omega = 92.5$ THz. The entirely different direction of vibration for silicon and Carbon indicate an overlap in $\vec{q}$

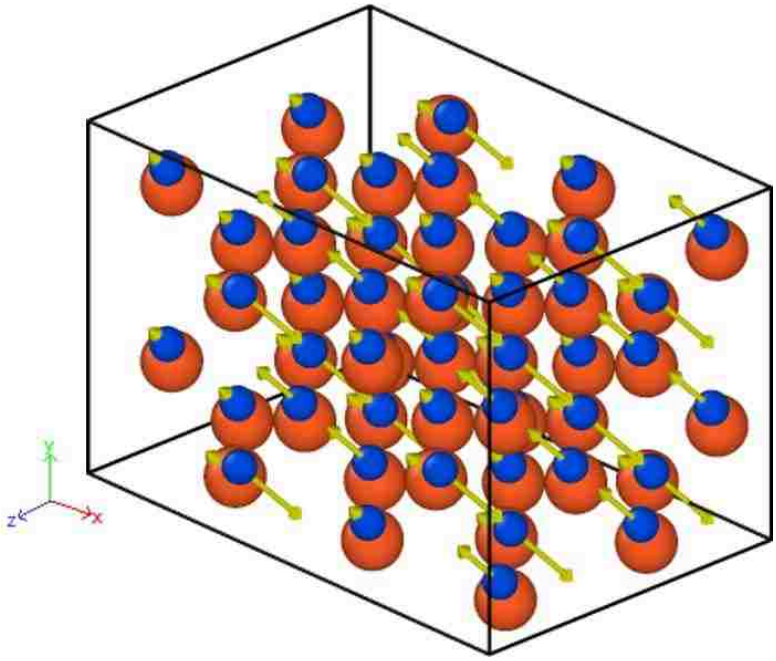

Figure 46: Atomic vibrations for optical mode for silicon (red) and carbon (blue) from an eigenmode analysis at $\omega = 188.7$ THz. The contribution from Carbon atoms to vibrational density of states is higher than that from Silicon

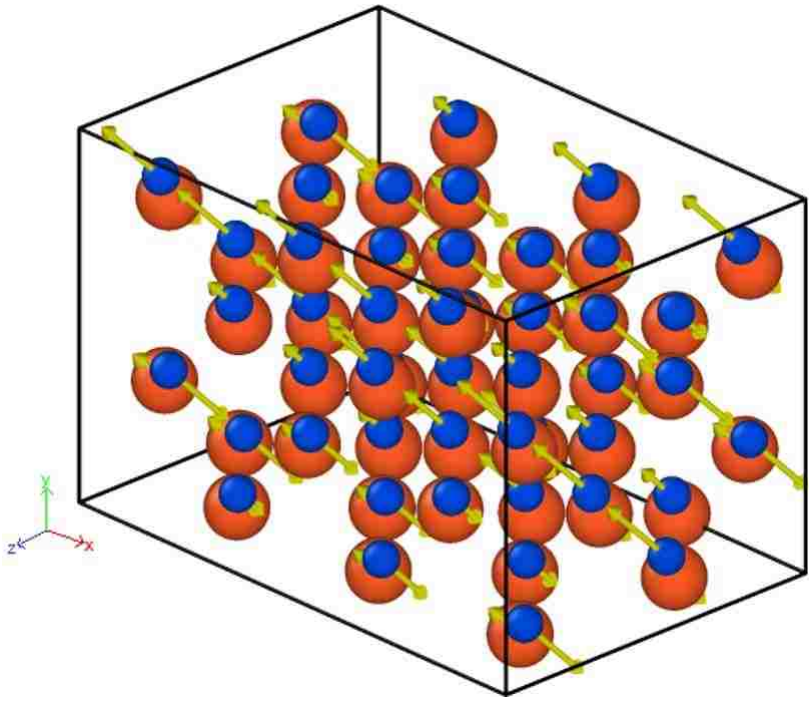

Figure 47: Atomic vibrations for optical mode for silicon (red) and carbon (blue) from an eigenmode analysis at $\omega = 191.6$ THz

References

[1] Yang, J., and Stabler, F. R., 2009, "Automotive applications of thermoelectric materials," Journal of Electronic Materials, 38(7), pp. 1245-1251.

[2] Sundarraj, P., Maity, D., Roy, S. S., and Taylor, R. A., 2014, "Recent advances in thermoelectric materials and solar thermoelectric generators–a critical review," RSC Advances, 4(87), pp. 46860-46874.

[3] Kajikawa, T., Ito, M., Katsube, I., and Shibuya, E., "Development of thermoelectric power generation system utilizing heat of combustible solid waste," Proc. The thirteenth international conference on thermoelectrics, AIP Publishing, pp. 314-318.

[4] Kagawa, S., Sakamoto, M., and Hirayama, N., "A practical test of a Bi-Te thermoelectric waste heat generator system in an incinerator using oil for heat transfer," Proc. Thermoelectrics, 1999. Eighteenth International Conference on, IEEE, pp. 321-324.

[5] Zhao, D., and Tan, G., 2014, "A review of thermoelectric cooling: materials, modeling and applications," Applied Thermal Engineering, 66(1), pp. 15-24.

[6] DiSalvo, F. J., 1999, "Thermoelectric cooling and power generation," Science, 285(5428), pp. 703-706.

[7] Ebrahimi, K., Jones, G. F., and Fleischer, A. S., 2014, "A review of data center cooling technology, operating conditions and the corresponding low-grade waste heat recovery opportunities," Renewable and Sustainable Energy Reviews, 31, pp. 622-638.

[8] Yu, C., and Chau, K., 2009, "Thermoelectric automotive waste heat energy recovery using maximum power point tracking," Energy Conversion and Management, 50(6), pp. 1506-1512.

[9] Blanke, B. C., Birden, J. H., Jordan, K. C., Murphy, E. L., Commission, U. S. A. E., and Laboratory, M., 1962, Nuclear Battery-thermocouple Type Summary Report, Mound Laboratory.

[10] Yang, J., "Potential applications of thermoelectric waste heat recovery in the automotive industry," Proc. Thermoelectrics, 2005. ICT 2005. 24th International Conference on, IEEE, pp. 170-174.

[11] Kumar, S., Heister, S. D., Xu, X., Salvador, J. R., and Meisner, G. P., 2013, "Thermoelectric Generators for Automotive Waste Heat Recovery Systems Part I: Numerical Modeling and Baseline Model Analysis," Journal of Electronic Materials, 42(4), pp. 665-674.

[12] Venkatasubramanian, R., Siivola, E., Colpitts, T., and O'Quinn, B., 2001, "Thin-film thermoelectric devices with high room-temperature figures of merit," Nature, 413(6856), pp. 597-602.

[13] Harman, T. C., Walsh, M. P., Laforge, B. E., and Turner, G. W., 2005, "Nanostructured thermoelectric materials," Journal of Electronic Materials, 34(5), pp. L19-L22.

[14] Rowe, D., 2006, Thermoelectrics Handbook: Macro to Nano, CRC Press, Boca Raton.

[15] Nolas, G. S., Sharp, J., and Goldsmind, H., 2001, Thermoelectrics: Basic Principles and New Materials Developments, Springer, New York.

[16] Dresselhaus, M. S., Chen, G., Tang, M. Y., Yang, R., Lee, H., Wang, D., Ren, Z., Fleurial, J.-P., and Gogna, P., 2007, "New directions for low-dimensional thermoelectric materials," Advanced Materials, 19(8), pp. 1043-1053.

[17] Minnich, A. J., Dresselhaus, M. S., Ren, Z. F., and Chen, G., 2009, "Bulk nanostructured thermoelectric materials: current research and future prospects," Energy & Environmental Science, 2(5), pp. 466-479.

[18] Hicks, L., and Dresselhaus, M., 1993, "Effect of quantum-well structures on the thermoelectric figure of merit," Physical Review B, 47(19), p. 12727.

[19] Poudel, B., Hao, Q., Ma, Y., Lan, Y., Minnich, A., Yu, B., Yan, X., Wang, D., Muto, A., Vashaee, D., Chen, X., Liu, J., Dresselhaus, M. S., Chen, G., and Ren, Z., 2008, "High-thermoelectric performance of nanostructured bismuth antimony telluride bulk alloys," Science, 320(5876), pp. 634-638.

[20] Chen, G., 1998, "Thermal conductivity and ballistic-phonon transport in the cross-plane direction of superlattices," Physical Review B, 57(23), pp. 14958-14973.

[21] Dames, C., and Chen, G., 2006, "Thermal conductivity of nanostructured thermoelectric materials," Thermoelectrics Handbook: Macro to Nano, D. M. Row, ed., Taylor & Francis, New York.

[22] Kapitza, P., 1941, "The study of heat transfer in helium II," J. Phys.(USSR), 4(1-6), pp. 181-210.

[23] Matatagui, E., Thompson, A., and Cardona, M., 1968, "Thermoreflectance in semiconductors," Physical Review, 176(3), p. 950.

[24] Thorne, S., Ippolito, S., Ünlü, M., and Goldberg, B., "High-resolution thermoreflectance microscopy," Proc. MRS Proceedings, Cambridge Univ Press, p. G12. 19.

[25] Minnich, A. J., Johnson, J., Schmidt, A., Esfarjani, K., Dresselhaus, M., Nelson, K. A., and Chen, G., 2011, "Thermal conductivity spectroscopy technique to measure phonon mean free paths," Physical Review Letters, 107(9), p. 095901.

[26] Koh, Y. K., and Cahill, D. G., 2007, "Frequency dependence of the thermal conductivity of semiconductor alloys," Physical Review B, 76(7), p. 075207.

[27] Cuffe, J., Eliason, J. K., Maznev, A. A., Collins, K. C., Johnson, J. A., Shchepetov, A., Prunnila, M., Ahopelto, J., Torres, C. M. S., and Chen, G., 2014, "Reconstructing phonon mean free path contributions to thermal conductivity using nanoscale membranes," arXiv preprint arXiv:1408.6747.

[28] Minnich, A., 2015, "Advances in the measurement and computation of thermal phonon transport properties," Journal of Physics: Condensed Matter, 27(5), p. 053202.

[29] Yang, F., and Dames, C., 2013, "Mean free path spectra as a tool to understand thermal conductivity in bulk and nanostructures," Physical Review B, 87(3), p. 035437.

[30] Cheaito, R., Gaskins, J. T., Caplan, M. E., Donovan, B. F., Foley, B. M., Giri, A., Duda, J. C., Szwejkowski, C. J., Constantin, C., and Brown-Shaklee, H. J., 2015, "Thermal boundary conductance accumulation and interfacial phonon transmission: Measurements and theory," Physical Review B, 91(3), p. 035432.

[31] Zhou, X., Jones, R. E., Duda, J., and Hopkins, P., 2013, "Molecular dynamics studies of material property effects on thermal boundary conductance," Physical Chemistry Chemical Physics, 15(26), pp. 11078-11087.

[32] Merabia, S., and Termentzidis, K., 2012, "Thermal conductance at the interface between crystals using equilibrium and nonequilibrium molecular dynamics," Physical Review B, 86(9), p. 094303.

[33] Landry, E., and McGaughey, A., 2009, "Thermal boundary resistance predictions from molecular dynamics simulations and theoretical calculations," Physical Review B, 80(16), p. 165304.

[34] Crocombette, J.-P., and Gelebart, L., 2009, "Multiscale modeling of the thermal conductivity of polycrystalline silicon carbide," Journal of Applied Physics, 106(8), p. 083520.

[35] Bagri, A., Kim, S.-P., Ruoff, R. S., and Shenoy, V. B., 2011, "Thermal transport across twin grain boundaries in polycrystalline graphene from nonequilibrium molecular dynamics simulations," Nano letters, 11(9), pp. 3917-3921.

[36] Duda, J. C., Kimmer, C. J., Soffa, W. A., Zhou, X. W., Jones, R. E., and Hopkins, P. E., 2012, "Influence of crystallographic orientation and anisotropy on Kapitza conductance via classical molecular dynamics simulations," Journal of Applied Physics, 112(9).

[37] Carlborg, C. F., Shiomi, J., and Maruyama, S., 2008, "Thermal boundary resistance between single-walled carbon nanotubes and surrounding matrices," Physical Review B, 78(20), p. 205406.

[38] Jones, R. E., Duda, J. C., Zhou, X. W., Kimmer, C. J., and Hopkins, P. E., 2013, "Investigation of size and electronic effects on Kapitza conductance with non-equilibrium molecular dynamics," Applied Physics Letters, 102(18).

[39] Zhou, X. W., Jones, R. E., Kimmer, C. J., Duda, J. C., and Hopkins, P. E., 2013, "Relationship of thermal boundary conductance to structure from an analytical model plus molecular dynamics simulations," Physical Review B, 87(9), p. 094303.

[40] Wang, T., Madsen, G., and Hartmaier, A., 2014, "Atomistic study of the influence of lattice defects on the thermal conductivity of silicon," Modelling and Simulation in Materials Science and Engineering, 22(3), p. 035011.

[41] Ni, Y., Xiong, S., Volz, S., and Dumitrică, T., 2014, "Thermal Transport Along the Dislocation Line in Silicon Carbide," Physical Review Letters, 113(12), p. 124301.

[42] Hopkins, P. E., 2013, "Thermal transport across solid interfaces with nanoscale imperfections: effects of roughness, disorder, dislocations, and bonding on thermal boundary conductance," International Scholarly Research Notices, 2013.

[43] Hopkins, P. E., Duda, J. C., Clark, S. P., Hains, C. P., Rotter, T. J., Phinney, L. M., and Balakrishnan, G., 2011, "Effect of dislocation density on thermal boundary conductance across GaSb/GaAs interfaces," Applied Physics Letters, 98(16), p. 161913.

[44] Duda, J. C., English, T. S., Piekos, E. S., Soffa, W. A., Zhigilei, L. V., and Hopkins, P. E., 2011, "Implications of cross-species interactions on the temperature dependence of Kapitza conductance," Physical Review B, 84(19), p. 193301.

[45] Duda, J. C., English, T. S., Piekos, E. S., Beechem, T. E., Kenny, T. W., and Hopkins, P. E., 2012, "Bidirectionally tuning Kapitza conductance through the inclusion of substitutional impurities," Journal of Applied Physics, 112(7), p. 073519.

[46] Duda, J. C., and Hopkins, P. E., 2012, "Systematically controlling Kapitza conductance via chemical etching," Applied Physics Letters, 100(11), p. 111602.

[47] Harmer, M. P., 2011, "The phase behavior of interfaces," Science, 332(6026), pp. 182-183.

[48] Dillon, S. J., Tang, M., Carter, W. C., and Harmer, M. P., 2007, "Complexion: A new concept for kinetic engineering in materials science," Acta Materialia, 55(18), pp. 6208-6218.

[49] Millett, P. C., Selvam, R. P., and Saxena, A., 2006, "Molecular dynamics simulations of grain size stabilization in nanocrystalline materials by addition of dopants," Acta materialia, 54(2), pp. 297-303.

[50] Millett, P. C., Selvam, R. P., and Saxena, A., 2007, "Stabilizing nanocrystalline materials with dopants," Acta Materialia, 55(7), pp. 2329-2336.

[51] Plimpton, S., 1995, "Fast parallel algorithms for short-range molecular dynamics," Journal of computational physics, 117(1), pp. 1-19.

[52] Goel, N., Webb III, E., Oztekin, A., Rickman, J., and Neti, S., 2015, "Kapitza resistance at segregated boundaries in β-SiC," Journal of Applied Physics, 118(11), p. 115101.

[53] Allen, M. P., and Tildesley, D. J., 1989, Computer simulation of liquids, Oxford university press.

[54] Frenkel, D., and Smit, B., 2001, Understanding molecular simulation: from algorithms to applications, Academic press.

[55] Porter, L. J., Li, J., and Yip, S., 1997, "Atomistic modeling of finite-temperature properties of β-SiC. I. Lattice vibrations, heat capacity, and thermal expansion," Journal of Nuclear Materials, 246(1), pp. 53-59.
[56] Lukes, J. R., and Zhong, H., 2007, "Thermal conductivity of individual single-wall carbon nanotubes," Journal of Heat Transfer, 129(6), pp. 705-716.
[57] Ziman, J. M., 1960, Electrons and phonons: the theory of transport phenomena in solids, Oxford University Press.
[58] Tersoff, J., 1990, "Carbon defects and defect reactions in silicon," Physical review letters, 64(15), p. 1757.
[59] Tersoff, J., 1994, "Chemical order in amorphous silicon carbide," Physical Review B, 49(23), p. 16349.
[60] Tersoff, J., 1988, "New empirical approach for the structure and energy of covalent systems," Physical Review B, 37(12), p. 6991.
[61] Tersoff, J., 1989, "Modeling solid-state chemistry: Interatomic potentials for multicomponent systems," Physical Review B, 39(8), p. 5566.
[62] Jones, R. E., Duda, J. C., Zhou, X. W., Kimmer, C. J., and Hopkins, P. E., 2013, "Investigation of size and electronic effects on Kapitza conductance with non-equilibrium molecular dynamics," Applied Physics Letters, 102(18), p. 183119.
[63] Stevens, R. J., Zhigilei, L. V., and Norris, P. M., 2007, "Effects of temperature and disorder on thermal boundary conductance at solid–solid interfaces: Nonequilibrium molecular dynamics simulations," International Journal of Heat and Mass Transfer, 50(19), pp. 3977-3989.
[64] Ladd, A. J., Moran, B., and Hoover, W. G., 1986, "Lattice thermal conductivity: A comparison of molecular dynamics and anharmonic lattice dynamics," Physical Review B, 34(8), p. 5058.
[65] Volz, S. G., and Chen, G., 2000, "Molecular-dynamics simulation of thermal conductivity of silicon crystals," Physical Review B, 61(4), pp. 2651-2656.
[66] Schelling, P. K., Phillpot, S. R., and Keblinski, P., 2002, "Comparison of atomic-level simulation methods for computing thermal conductivity," Physical Review B, 65(14), p. 144306.

[67] Li, J., Porter, L., and Yip, S., 1998, "Atomistic modeling of finite-temperature properties of crystalline β-SiC: II. Thermal conductivity and effects of point defects," Journal of Nuclear Materials, 255(2), pp. 139-152.
[68] McGaughey, A. J., and Kaviany, M., 2004, "Quantitative validation of the Boltzmann transport equation phonon thermal conductivity model under the single-mode relaxation time approximation," Physical Review B, 69(9), p. 094303.
[69] Henry, A. S., and Chen, G., 2008, "Spectral phonon transport properties of silicon based on molecular dynamics Simulations and lattice dynamics," Journal of Computational and Theoretical Nanoscience, 5(2), pp. 141-152.
[70] Henry, A., and Chen, G., 2009, "Anomalous heat conduction in polyethylene chains: Theory and molecular dynamics simulations," Physical Review B, 79(14), p. 144305.
[71] Vogelsang, R., Hoheisel, C., and Ciccotti, G., 1987, "Thermal conductivity of the Lennard-Jones liquid by molecular dynamics calculations," The Journal of chemical physics, 86(11), pp. 6371-6375.
[72] Che, J., Çağın, T., Deng, W., and Goddard III, W. A., 2000, "Thermal conductivity of diamond and related materials from molecular dynamics simulations," The Journal of Chemical Physics, 113(16), pp. 6888-6900.
[73] Zhou, X., Aubry, S., Jones, R., Greenstein, A., and Schelling, P., 2009, "Towards more accurate molecular dynamics calculation of thermal conductivity: Case study of GaN bulk crystals," Physical Review B, 79(11), p. 115201.
[74] Maiti, A., Mahan, G. D., and Pantelides, S. T., 1997, "Dynamical simulations of nonequilibrium processes - Heat flow and the Kapitza resistance across grain boundaries," Solid State Communications, 102(7), pp. 517-521.
[75] Oligschleger, C., and Schön, J., 1999, "Simulation of thermal conductivity and heat transport in solids," Physical Review B, 59(6), p. 4125.
[76] Schelling, P., Phillpot, S., and Keblinski, P., 2004, "Kapitza conductance and phonon scattering at grain boundaries by simulation," Journal of Applied Physics, 95(11), pp. 6082-6091.
[77] Hoover, W. G., 2012, Computational statistical mechanics, Elsevier.

[78] Jund, P., and Jullien, R., 1999, "Molecular-dynamics calculation of the thermal conductivity of vitreous silica," Physical Review B, 59(21), pp. 13707-13711.

[79] Schelling, P. K., and Phillpot, S. R., 2001, "Mechanism of Thermal Transport in Zirconia and Yttria-Stabilized Zirconia by Molecular-Dynamics Simulation," Journal of the American Ceramic Society, 84(12), pp. 2997-3007.

[80] Sellan, D. P., Landry, E. S., Turney, J. E., McGaughey, A. J. H., and Amon, C. H., 2010, "Size effects in molecular dynamics thermal conductivity predictions," Physical Review B, 81(21), p. 214305.

[81] Howell, P., 2011, "Thermal conductivity calculation with the molecular dynamics direct method I: More robust simulations of solid materials," Journal of Computational and Theoretical Nanoscience, 8(10), pp. 2129-2143.

[82] Flewitt, P. E. J., and Wild, R. K., 2001, "Grain boundaries: their microstructure and chemistry," Grain Boundaries: Their Microstructure and Chemistry, by PEJ Flewitt, RK Wild, pp. 338. ISBN 0-471-97951-1. Wiley-VCH, April 2001., p. 338.

[83] Lejček, P., 2010, "Grain Boundaries: Description, Structure and Thermodynamics," Grain Boundary Segregation in Metals, Springer, pp. 5-24.

[84] Wolf, D., and Jaszczak, J., 1992, "Materials interfaces: atomic-level structure and properties."

[85] Phillips, R., 2001, Crystals, defects and microstructures: modeling across scales, Cambridge University Press.

[86] Olmsted, D. L., Foiles, S. M., and Holm, E. A., 2009, "Survey of computed grain boundary properties in face-centered cubic metals: I. Grain boundary energy," Acta Materialia, 57(13), pp. 3694-3703.

[87] Holm, E. A., Olmsted, D. L., and Foiles, S. M., 2010, "Comparing grain boundary energies in face-centered cubic metals: Al, Au, Cu and Ni," Scripta Materialia, 63(9), pp. 905-908.

[88] Lejcek, P., 2010, Grain boundary segregation in metals, Springer Science & Business Media.

[89] Cheaito, R., Duda, J. C., Beechem, T. E., Hattar, K., Ihlefeld, J. F., Medlin, D. L., Rodriguez, M. A., Campion, M. J., Piekos, E. S., and Hopkins, P. E., 2012, "Experimental

Investigation of Size Effects on the Thermal Conductivity of Silicon-Germanium Alloy Thin Films," Physical review letters, 109(19), p. 195901.
[90] Ong, W.-L., Rupich, S. M., Talapin, D. V., McGaughey, A. J., and Malen, J. A., 2013, "Surface chemistry mediates thermal transport in three-dimensional nanocrystal arrays," Nature materials, 12(5), pp. 410-415.
[91] Swartz, E. T., and Pohl, R. O., 1989, "Thermal boundary resistance," Reviews of Modern Physics, 61(3), p. 605.
[92] Costescu, R. M., Wall, M. A., and Cahill, D. G., 2003, "Thermal conductance of epitaxial interfaces," Physical Review B, 67(5).
[93] McGaughey, A. J., and Kaviany, M., 2006, "Phonon transport in molecular dynamics simulations: formulation and thermal conductivity prediction," Advances in Heat Transfer, 39(2), pp. 169-225.
[94] McQuarrie, D. A., 2000, Statistical Mechanics, University Science Books.
[95] Hansen, J.-P., and McDonald, I. R., 1990, Theory of simple liquids, Elsevier.
[96] Hu, L., Desai, T., and Keblinski, P., 2011, "Determination of interfacial thermal resistance at the nanoscale," Physical Review B, 83(19), p. 195423.
[97] Hu, M., and Poulikakos, D., 2013, "Graphene mediated thermal resistance reduction at strongly coupled interfaces," International Journal of Heat and Mass Transfer, 62, pp. 205-213.
[98] Schelling, P. K., Phillpot, S. R., and Keblinski, P., 2002, "Phonon wave-packet dynamics at semiconductor interfaces by molecular-dynamics simulation," Applied Physics Letters, 80(14), pp. 2484-2486.
[99] Evans, W. J., Shen, M., and Keblinski, P., 2012, "Inter-tube thermal conductance in carbon nanotubes arrays and bundles: Effects of contact area and pressure," Applied Physics Letters, 100(26), p. 261908.
[100] Majumdar, A., 1993, "Microscale heat conduction in dielectric thin films," Journal of Heat Transfer, 115(1), pp. 7-16.
[101] Howell, P., 2011, "Thermal conductivity calculation with the molecular dynamics direct method II: Improving the computational efficiency," Journal of Computational and Theoretical Nanoscience, 8(10), pp. 2144-2154.

[102] Goldsmid, H., and Penn, A., 1968, "Boundary scattering of phonons in solid solutions," Physics Letters A, 27(8), pp. 523-524.
[103] Kittel, C., 2005, Introduction to solid state physics, Wiley.
[104] Landry, E., Hussein, M., and McGaughey, A., 2008, "Complex superlattice unit cell designs for reduced thermal conductivity," Physical Review B, 77(18), p. 184302.
[105] Papanikolaou, N., 2008, "Lattice thermal conductivity of SiC nanowires," Journal of Physics-Condensed Matter, 20(13), p. 135201.
[106] Crocombette, J.-P., Dumazer, G., Hoang, N. Q., Gao, F., and Weber, W. J., 2007, "Molecular dynamics modeling of the thermal conductivity of irradiated SiC as a function of cascade overlap," Journal of Applied Physics, 101(2), p. 023527.
[107] Stoner, R., and Maris, H., 1993, "Kapitza conductance and heat flow between solids at temperatures from 50 to 300 K," Physical Review B, 48(22), p. 16373.
[108] Randle, V., and Engler, O., 2000, Introduction to texture analysis: macrotexture, microtexture and orientation mapping, CRC press.
[109] Tien, C., Majumdar, A., and Gerner, F., 1998, Microscale Energy Transport, Taylor and Francis, Washington, DC.
[110] Young, D. A., and Maris, H. J., 1989, "Lattice-dynamical calculation of the Kapitza resistance between fcc lattices," Physical Review B, 40(6), pp. 3685-3693.
[111] Klemens, P., 1955, "The scattering of low-frequency lattice waves by static imperfections," Proceedings of the Physical Society. Section A, 68(12), p. 1113.
[112] Dickey, J., and Paskin, A., 1969, "Computer simulation of the lattice dynamics of solids," Physical Review, 188(3), p. 1407.
[113] Welch, P. D., 1967, "The use of fast Fourier transform for the estimation of power spectra: A method based on time averaging over short, modified periodograms," IEEE Transactions on audio and electroacoustics, 15(2), pp. 70-73.
[114] Press, W. H., 2007, Numerical recipes 3rd edition: The art of scientific computing, Cambridge university press.
[115] Loong, C.-K., Vashishta, P., Kalia, R., Jin, W., Degani, M., Hinks, D., Price, D., Jorgensen, J., Dabrowski, B., and Mitchell, A., 1992, "Phonon density of states and oxygen-isotope effect in Ba 1− x K x BiO 3," Physical Review B, 45(14), p. 8052.

[116] Meyer, R., and Comtesse, D., 2011, "Vibrational density of states of silicon nanoparticles," Physical Review B, 83(1), p. 014301.

[117] Turney, J., Landry, E., McGaughey, A., and Amon, C., 2009, "Predicting phonon properties and thermal conductivity from anharmonic lattice dynamics calculations and molecular dynamics simulations," Physical Review B, 79(6), p. 064301.

[118] Dove, M. T., 1993, Introduction to lattice dynamics, Cambridge university press.

[119] Taylor, R., 1966, "The thermal conductivity of pyrolytic graphite," Philosophical Magazine, 13(121), pp. 157-166.

[120] Zhao, L.-D., Lo, S.-H., Zhang, Y., Sun, H., Tan, G., Uher, C., Wolverton, C., Dravid, V. P., and Kanatzidis, M. G., 2014, "Ultralow thermal conductivity and high thermoelectric figure of merit in SnSe crystals," Nature, 508(7496), pp. 373-377.

[121] Brown, S. R., Kauzlarich, S. M., Gascoin, F., and Snyder, G. J., 2006, "Yb14MnSb11: New high efficiency thermoelectric material for power generation," Chemistry of materials, 18(7), pp. 1873-1877.

[122] Kurosaki, K., Kosuga, A., Muta, H., Uno, M., and Yamanaka, S., 2005, "Ag9TlTe5: a high-performance thermoelectric bulk material with extremely low thermal conductivity," Applied Physics Letters, 87(6).

[123] Morelli, D. T., Jovovic, V., and Heremans, J. P., 2008, "Intrinsically minimal thermal conductivity in cubic I-V-VI_2 semiconductors," Physical Review Letters, 101(3).

[124] Hopkins, P. E., Beechem, T., Duda, J. C., Hattar, K., Ihlefeld, J. F., Rodriguez, M. A., and Piekos, E. S., 2011, "Influence of anisotropy on thermal boundary conductance at solid interfaces," Physical Review B, 84(12), p. 125408.

[125] Costescu, R. M., Wall, M. A., and Cahill, D. G., 2003, "Thermal conductance of epitaxial interfaces," Physical Review B, 67(5), p. 054302.

[126] Duda, J. C., Kimmer, C. J., Soffa, W. A., Zhou, X. W., Jones, R. E., and Hopkins, P. E., 2012, "Influence of crystallographic orientation and anisotropy on Kapitza conductance via classical molecular dynamics simulations," Journal of Applied Physics, 112(9), p. 093515.

[127] Rickman, J., Chan, H., Harmer, M., and Luo, J., 2013, "Grain-boundary layering transitions in a model bicrystal," Surface Science, 618, pp. 88-93.

[128] Cantwell, P. R., Tang, M., Dillon, S. J., Luo, J., Rohrer, G. S., and Harmer, M. P., 2014, "Grain boundary complexions," Acta Materialia, 62, pp. 1-48.
[129] Dove, M., 2011, "Introduction to the theory of lattice dynamics," École thématique de la Société Française de la Neutronique, 12, pp. 123-159.

Vita

Nipun Goel was born on July 4th, 1986 to Mr. Pawan Kumar Goel and Neelam Lata in Delhi, India. Youngest of three brothers, he attended D.A.V. Public School in Delhi and graduated in 2004. Nipun received a Bachelor's in Technology in Power Engineering (with Mechanical Specialization) from Guru Gobind Singh Indraprasth University, Delhi, India in 2008. After completing his undergraduate studies, Nipun worked with Bechtel India Private Limited, Haryana, India, for two years where he gained industrial exposure. In the fall of 2010, he joined Lehigh University to pursue M.S. in Mechanical Engineering and stayed for a PhD in 2012.

While at Lehigh, Nipun was heavily involved on campus and served as the Vice-President and subsequently the President of the Graduate Student Senate from 2013 – 2015. In 2015, Nipun was recognized by Lehigh University with Student Life Leadership award for his contributions towards nurturing unity on campus. Throughout his tenure at Lehigh, Nipun was a teaching assistant for numerous courses, and also worked as the lead student with Industrial Assessment Center at Lehigh University.